National Library
of Canada

Canadian Theses Service

Ottawa, Canada
K1A 0N4

Bibliothèque nationale
du Canada

Services des thèses canadiennes

CANADIAN THESES

THÈSES CANADIENNES

NOTICE

The quality of this microfiche is heavily dependent upon the quality of the original thesis submitted for microfilming. Every effort has been made to ensure the highest quality of reproduction possible.

If pages are missing, contact the university which granted the degree.

Some pages may have indistinct print especially if the original pages were typed with a poor typewriter ribbon or if the university sent us an inferior photocopy.

Previously copyrighted materials (journal articles, published tests, etc.) are not filmed.

Reproduction in full or in part of this film is governed by the Canadian Copyright Act, R.S.C. 1970, c. C-30.

AVIS

La qualité de cette microfiche dépend grandement de la qualité de la thèse soumise au microfilmage. Nous avons tout fait pour assurer une qualité supérieure de reproduction.

S'il manque des pages, veuillez communiquer avec l'université qui a conféré le grade.

La qualité d'impression de certaines pages peut laisser à désirer, surtout si les pages originales ont été dactylographiées à l'aide d'un ruban usé ou si l'université nous a fait parvenir une photocopie de qualité inférieure.

Les documents qui font déjà l'objet d'un droit d'auteur (articles de revue, examens publiés, etc.) ne sont pas microfilmés.

La reproduction, même partielle, de ce microfilm est soumise à la Loi canadienne sur le droit d'auteur, SRC 1970, c. C-30.

THIS DISSERTATION
HAS BEEN MICROFILMED
EXACTLY AS RECEIVED

LA THÈSE A ÉTÉ
MICROFILMÉE TELLE QUE
NOUS L'AVONS REÇUE

NL-339 (r.86/06)

Canada

THE UNIVERSITY OF ALBERTA

Buoyancy Effects on Laminar Forced Convection in Curved Pipes and Flow Visualization Studies of Convective Instability Phenomena

by

© Yong W. Kim

A THESIS

SUBMITTED TO THE FACULTY OF GRADUATE STUDIES AND RESEARCH
IN PARTIAL FULFILMENT OF THE REQUIREMENTS FOR THE DEGREE
of Master of Science

Department of Mechanical Engineering

EDMONTON, ALBERTA
Fall 1986

Permission has been granted to the National Library of Canada to microfilm this thesis and to lend or sell copies of the film.

The author (copyright owner) has reserved other publication rights, and neither the thesis nor extensive extracts from it may be printed or otherwise reproduced without his/her written permission.

L'autorisation a été accordée à la Bibliothèque nationale du Canada de microfilmer cette thèse et de prêter ou de vendre des exemplaires du film.

L'auteur (titulaire du droit d'auteur) se réserve les autres droits de publication; ni la thèse ni de longs extraits de celle-ci ne doivent être imprimés ou autrement reproduits sans son autorisation écrite.

ISBN 0-315-32325-6

THE UNIVERSITY OF ALBERTA

RELEASE FORM

NAME OF AUTHOR Yong W. Kim

TITLE OF THESIS Buoyancy Effects on Laminar Forced Convection in Curved Pipes and Flow Visualization Studies of Convective Instability Phenomena

DEGREE FOR WHICH THESIS WAS PRESENTED Master of Science

YEAR THIS DEGREE GRANTED Fall 1986

Permission is hereby granted to THE UNIVERSITY OF ALBERTA LIBRARY to reproduce single copies of this thesis and to lend or sell such copies for private, scholarly of scientific research purposes only.

The author reserves other publication rights, and neither the thesis nor extensive extracts from it may be printed or otherwise reproduced without the author's written permission.

(SIGNED) YONG WON KIM

ADDRESS: Gungjeon Apt. A-907
Bangbei-Dong, Gangnam
Seoul, South Korea
135

DATED July 21, 1986

THE UNIVERSITY OF ALBERTA

FACULTY OF GRADUATE STUDIES AND RESEARCH

The undersigned certify that they have read, and recommend to the Faculty of Graduate Studies and Research for acceptance, a thesis entitled Buoyancy Effects on Laminar Forced Convection in Curved Pipes and Flow Visualization Studies of Convective Instability Phenomena submitted by Yong W. Kim in partial fulfilment of the requirements for the degree of Master of Science.

...K.C. Cheng.....
(Supervisor)

Gerald W. Sadler...

....

Date : ...July 21, 1986....

To My Wife

Eun Yi

Abstract

Experiments were conducted to study the buoyancy force effects on laminar forced convection flow in thermally and hydrodynamically developing region of a 200° pipe bend using air under the uniform wall heat flux boundary condition with peripherally uniform wall temperature. Attention is given to the effect of varying inclination angle of the curvature plane of the pipe bend on heat transfer characteristics. Measurements for wall temperature distributions and Nusselt numbers were made for Dean numbers 100, 150, 200, 300, 430, 600 and 800 for three different inclination angles from the horizontal directions: upward vertical, horizontal and downward vertical cases. The range of ReRa was 7.05×10^3 ~ 2.20×10^5. Experimental results for axial wall temperature distributions, local and average Nusselt numbers are presented and compared with recent numerical results in the literature.

Flow visualization studies employing a smoke tracer method were also conducted to provide physical understanding of the buoyancy effects in curved pipe flows. Observations of the secondary flow motion were made at the exit of the test pipe. Photographs showing the buoyancy affected secondary flow patterns are presented and compared with the streamline patterns obtained by a recent numerical calculation.

Flow visualization experiments were performed in a specially designed suction type low speed wind tunnel to study the vortex instability of natural convection flow on inclined isothermally heated plates with inclination angles from the horizontal direction at $\theta = 0, 5, 10, 15$ and 20°. Within the scope of present investigation, three characteristic flow regimes are identified, i.e. a two-dimensional laminar flow, a transition regime for developing longitudinal vortices and a turbulent regime after the breakdown of the longitudinal vortices. The photographs for side and top views of the flow and for cross-sectional views of the developing secondary flow in the post-critical regime are presented. The instability data for cirtical Grashof number and wavelength are presented with comparison made against theoretical predictions from literature.

Similar flow visualization experiments were also carried out for the case of a horizontal Blasius flow heated from below. Attention is given to the effect of an unheated length on the secondary flow patterns and the instability characteristics. The photographs for the side and top views and the cross-sectional views showing the onset and subsequent growth of the longitudinal vortex rolls are presented for three different unheated lengths: $x_o = 0$, 33.5 and 60.5 cm. The instability data for critical Grashof number are also obtained and compared with published results.

Acknowledgement

The author wishes to express his sincere gratitude to Dr. K.C. Cheng, research supervisor, for his guidance and encouragement during the course of this thesis project.

The author also wishes to give thanks to the technical staff and machinists of the Department of Mechanical Engineering headed by Tom Villet and Al Muir for their excellent assistance and cooperation during the construction of the experimental apparatus. Special thanks go to Terry Nord for his assistance with electronic instrumentation.

Financial aid from the Natural Sciences and Engineering Research Council of Canada throughout this research work is greatly appreciated.

The author is most grateful to his wife for her immeasurable emotional help and willingness to spend many painful hours in proofreading this thesis.

Table of Contents

Chapter Page

1. Introduction 1

1.1 Background Information 1

1.1.1 Buoyancy Force Effects in a Heated Curved Pipe 1

1.1.2 Flow Visualization Studies on Convective Instability Phenomena 3

1.2 Scope of the Study 6

1.3 References 8

2. Buoyancy Force Effects on Laminar Forced Convection Flow in Curved Pipes 12

2.1 Introduction 12

2.2 Experimental Apparatus 16

2.2.1 General Description of Test Setup 16

2.2.2 Curved Pipe and Heating Arrangement 17

2.2.3 Wall Temperature Measurement 18

2.2.4 Bulk Temperature Measurement 19

2.2.5 Flow Rate Measurement 20

2.3 Auxiliary Systems 21

2.3.1 AC Power Source and Constant Wattage Control System 21

2.3.2 Vacuum Vessel 21

2.3.3 Data Acquisition System 22

2.4 Experimental Procedure 22

2.4.1 Calibration of Thermocouples 23

2.4.2 Start-up of Heating and Data Acquisition Procedure 23

2.5 Data Analysis 25

2.6 Results and Discussion 29

2.6.1 Axial and Peripheral Wall Temperature Distributions 29

2.6.2 Local Nusselt Number Distributions 30

2.6.3 The study of Buoyancy Effect at Fixed Inclination Angle of Curvature Plane 31

2.6.4 The study of Buoyancy Effect with Variation of α 35

2.6.5 Results of Error Analysis and Additional Experiments Using Vacuum Vessel 39

2.7 Concluding Remarks 42

2.8 References 44

3. Flow Visualization Study on Laminar Forced Convection Flow in Curved Pipes 73

3.1 Introduction 73

3.2 Experimental Parameters 77

3.3 Experimental Apparatus and Procedure 77

3.4 Results and Discussion 79

3.4.1 Upward Vertical Flow 79

3.4.2 Horizontal Flow 83

3.4.3 Downward Vertical Flow 85

3.4.4 Transient Secondary Flow Field at De= 55 86

3.5 Concluding Remarks 87

3.6 References 88

4. Flow Visualization Studies on Vortex Instability of Natural Convection Flow over Horizontal and Slightly Inclined Constant Temperature Plates ... 100

4.1 Introduction 100

4.2 Apparatus and Experimental Procedure 104

4.2.1 Wind Tunnel and Isothermal Heating Plate Assembly 104

4.2.2 Wall Temperature Measurement 105

4.2.3 The Flow Visualization Technique and Photographic Arrangement 106

4.2.4 Measurements for the Onset of Instability 106

4.3 The Experimental Parameters 107

4.4 Results and Discussion 108

4.4.1 Horizontal Plate 108

4.4.2 Inclined Plate (0° < $\theta \leq$ 20°) 110

4.4.3 Instability Results and Wavelength Correlation 112

4.5 Concluding Remarks 115

4.6 References 116

5. Flow Visualization Study on the Vortex Instability in a Horizontal Blasius Flow Heated From Below 131

5.1 Introduction 131

5.2 Apparatus and Experimental Procedure 133

5.2.1 Wind Tunnel and Isothermal Heating Plate 133

5.2.2 Wall and Air Temperature Measurements 134

5.2.3 The Flow Visualization Technique and Photographic Arrangement 135

5.2.4 Measurements for the Onset of Instability 135

5.2.5 Range of Experimental Parameters 136

5.3 Results and Discussion 137

5.3.1 Air Temperature Profiles 137

5.3.2 Results of Flow Visualization Study 137

5.3.3 Instability Results 142

5.4 Concluding Remarks 143

5.5 References 145

6. Conclusion 157

6.1 Buoyancy Force Effects on Laminar Forced Convection Flow in Curved Pipes 157

6.2 Flow Visualization Studies on Laminar Forced Convection Flow in Curved Pipes 158

6.3 Flow Visualization Studies on Vortex Instability of Natural Convection Flow over Horizontal and Slightly Inclined Constant Temperature Plates 159

6.4 Flow Visualization Studies on Vortex Instability in a Horizontal Blasius Flow Heated From Below 160

Appendix I 162

List of Tables

Tables Page

2.1 Range of q_i^+ for the Present Experiments 35

3.1 Range of Experimental Parameters 77

4.1 Range of Experimental Parameters 107

4.2 Critical Grashof Numbers and Standard Deviations 113

5.1 Range of Experimental Parameters 136

List of Figures

Figures Page

2.1 Schematic Diagram for Test Setup 47

2.2 Locations of Thermocouples and Curved Pipe Dimensions 48

2.3 Flange at the Bend Inlet 49

2.4 Schematic Diagram for Mixing Box Design 50

2.5 Circuit Diagram for Constant Wattage Controller 51

2.6 Axial Wall Temperature Distribution for Horizontal Curved Pipe Flow 52

2.7 Peripheral Wall Temperature Distribution for Horizontal Curved Pipe Flow at De= 150, ϕ= 135° 53

2.8 Local Nusselt Number Variation for Horizontal Curved Pipe Flow 54

2.9 Axial Wall Temperature Distribution for Horizontal Curved Pipe Flow at De= 150 with ReRa as Parameter 55

2.10 Local Nusselt Number Variation for Horizontal Curved Pipe Flow at De= 150 with ReRa as Parameter 56

2.11 Nu_{180} vs. De for Horizontal Curved Pipe Flow with Gr_{av} as Parameter 57

2.12 Nu_{av} vs. De for Horizontal Curved Pipe Flow with Gr_{av} as Parameter 58

2.13 Nu_{180} vs. De for Upward Vertical Curved Pipe Flow with Gr_{av} as Parameter 59

2.14 Nu_{av} vs. De for Upward Vertical Curved Pipe Flow with Gr_{av} as Parameter 60

2.15 Nu_{180} vs. De for Downward Vertical Curved Pipe Flow with Gr_{av} as Parameter 61

2.16 Nu_{av} vs. De for Downward Vertical Curved Pipe Flow with Gr_{av} as Parameter 62

2.17 Nu_{180}/Nu_{s} vs. De for Horizontal Curved Pipe Flow with ReRa as Parameter 63

2.18 Nu_{180}/Nu_s vs. Gr/De^2 for Horizontal Curved Pipe Flow 64

2.19 Local Nusselt Number Variations and Heat Transfer Degradation Region 65

2.20 Schematic Diagrams Illustrating Buoyancy Force Effects with Varying Inclination Angle α 66

2.21 Axial Wall Temperature Distribution for α= 90°, 0° and -90° with ReRa as Parameter 67

2.22 Local Nusselt Number Variation with α and ReRa as Parameter 68

2.23 Nu_{180}/Nu_s vs. α for De=150 with ReRa as Parameter 69

2.24 Nu/Nu_s vs. α for De=150, ϕ=0° with ReRa as Parameter 70

2.25 Local Nusselt Number Variation for Horizontal Curved Pipe Flow in Insulation Vessel at 660 mmHg Vacuum 71

2.26 Nu_{180}/Nu_s vs. De for Horizontal Curved Pipe Flow in Insulation Vessel at 660 mmHg Vacuum 72

3.1 Streamline Patterns of Secondary Flow Motion with and without Buoyancy Effects [2] 74

3.2 Secondary Flow Patterns for Upward Vertical Flow at De=55 and 100 with ReRa and Γ as Parameters 90

3.3 Secondary Flow Patterns for Upward Vertical Flow at De=150 and 200 with ReRa and Γ as Parameters 91

3.4 Secondary Flow Patterns for Upward Vertical Flow at De=300, 430, 600 and 800 with ReRa and Γ as Parameters 92

3.5 Secondary Flow Patterns for Horizontal Flow at De=55 and 100 with ReRa and Γ as Parameters 93

3.6 Secondary Flow Patterns for Horizontal Flow at De=150 and 200 with ReRa and Γ as Parameters 94

3.7 Secondary Flow Patterns for Horizontal Flow at De=300, 430, 600 and 800 with ReRa and Γ as Parameters 95

3.8 Comparison Between the Streamline Patterns Obtained by Numerical Calculation [5] and Present Flow Visualization Result for Horizontal Flow Case 84

3.9 Secondary Flow Patterns for Downward Vertical Flow at De=55 and 100 with ReRa and Γ as Parameters 96

3.10 Secondary Flow Patterns for Downward Vertical Flow at De=150 and 200 with ReRa and Γ as Parameters 97

3.11 Secondary Flow Patterns for Downward Vertical Flow at De=300, 430, 600 and 800 with ReRa and Γ as Parameters 98

3.12 Transient Case for Horizontal Flow at De=55 with t and Fo as Parameters 99

4.1 Schematic Diagrams for (a) Wind Tunnel Test Facility and (b) Constant Temperature Plate and Auxiliary Equipment 120

4.2 Top and Side Views of Developing Longitudinal Vortices for $\theta=0°$, $T_w=51.8°C$ and $T_\infty=21.0°C$ 121

4.3 Cross-sectional Views of Secondary Flow Patterns for $\theta=0°$ and $\Delta T=30.8°K$ 122

4.4 Effect of ΔT on Developing Secondary Flow Patterns for $\theta=0°$ 123

4.5 Top and Side Views of Developing Longitudinal Vortices for $\theta=15°$ and $\Delta T=15.5°K$ 124

4.6 Cross-sectional Views of Secondary Flow Patterns for $\theta=15°$ and $\Delta T=15.5°K$ 125

4.7 Cross-sectional Views of Secondary Flow Patterns for $\theta=20°$ and $\Delta T=23.1°K$ 126

4.8 Effect of Inclination Angle on Developing Secondary Flow Patterns for $\theta=0°$ 127

4.9 Variation of Critical Grashof Number with Inclination Angle 128

4.10 Critical Grashof Number for Horizontal Plate ... 129

4.11 Correlation for the Wavelength of Vortex Rolls.. 130

5.1 Temperature Profiles for the Case of Stable Flow 146

5.2 Top and Side Views of Developing Longitudinal Vortices for x_o=0 cm, U_∞=0.05 m/s, T_w=57.4°C and T_∞=29.5°C 147

5.3 Cross-sectional Views of Secondary Flow Patterns for x_o=0 cm, U_∞=0.05 m/s and ΔT=27.9°K 148

5.4 Top and Side Views of Developing Longitudinal Vortices for x_o=33.5 cm, U_∞=0.04 m/s, T_w=56.0°C and T_∞=27.8°C 149

5.5 Cross-sectional Views of Secondary Flow Patterns for x_o=33.5 cm, U_∞=0.04 m/s and ΔT=28.2°K 150

5.6 Top and Side Views of Developing Longitudinal Vortices for x_o=60.5 cm, U_∞=0.04 m/s, T_w=58.5°C and T_∞=26.4°C 151

5.7 Cross-sectional Views of Secondary Flow Patterns for x_o=60.5 cm, U_∞=0.04 m/s and ΔT=32.1°K 152

5.8 Effect of ΔT on Developing Secondary Flow Patterns of Vortices for x_o=0 cm 153

5.9 Effect of U_∞ on Developing Secondary Flow Patterns of Vortices for x_o=0 cm 154

5.10 Experimental Instability Results for x_o=0 cm ... 155

5.11 Effect of x_o on Vortex Instability 156

Nomenclature

a	inside radius of curved pipe, m
C_p	specific heat of air, $J/(kg \cdot K)$
d	inside diameter of curved pipe, m
g	gravitational acceleration, 9.81 m/s^2
Gr	Grashof number, $g\beta\ [(T_{be}-T_{bi})/L]\ a^4/\nu^2$
Gr_{av}	average Grashof number, $g\beta\ [(\Delta T_i+\Delta T_{180})/2]\ a^3/\nu^2$
Gr_x	local Grashof number, $g\beta\ (\Delta T)\ x^3/\nu^2$
$Gr_x{}^*$	critical Grashof number, $g\beta\ (\Delta T)\ x_c{}^3/\nu^2$
h_{av}	average heat transfer coefficient based on $(\Delta T_i+\Delta T_{180})/2$, $W/(m^2 \cdot K)$
h_x	local heat transfer coefficient, $W/(m^2 \cdot K)$
k	thermal conductivity of air, $W/(m \cdot K)$
L	total heated length of curved pipe, m
m	mass flow rate of air flow, kg/s
P	atmospheric pressure, bar
Pr	Prandtl number, ν/κ
$q_i{}^+$	dimensionless heat flux, $(d/T_{bi})(dT_b/dx)/4$
Q_{input}	rate of heat released by heater, W
Q_{loss}	heat loss to environment, W
$Q_{rec.}$	rate of heat received by air, W
q_w	wall heat flux per unit area, W/m^2
Ra	Reyleigh number, GrPr
Rc	radius of curvature of bend, m
Re	Reynolds number, ud/ν
$ReRa$	buoyancy parameter
Re_x	local Reynolds number, $U_\infty x/\nu$

T	temperature, °K
T_b	bulk air temperature, °C
T_w	wall temperature, °C
T_∞	ambient air temperature (Ch. 4), °C free stream temperature (Ch. 5), °C
ΔT	wall to bulk temperature difference (Ch. 2,3), °K wall to ambient temperature difference (Ch. 4), °K wall to free stream temperature difference (Ch. 5), °K
u	mean velocity of curved pipe air flow, m/s
U_∞	free stream velocity, m/s
x	axial distance from bend inlet (Ch. 2,3), m distance from leading edge (Ch. 4,5), m
x_o	unheated length, m
x'	heated length $x-x_o$, m
y	coordinate in the upward vertical direction from heated surface, m
z	dimensionless axial distance, $x/d/(RePr)$
z'	dimensionless axial distance, x/a
α	inclination angle of the curvature plane of bend from the horizontal direction, °
β	coefficient of thermal expansion, 1/°K
δ_t	thermal boundary-layer thickness, m
κ	thermal diffusivity, m^2/s
λ	wavelength of vortex rolls, m
μ	absolute viscosity, kg/(ms)
ν	kinematic viscosity, m^2/s
θ	inclination angle of heated surface from the horizontal direction, °
θ_b	dimensionless bulk temperature, $(T_b-T_{bi})/(dT_b/dz')$
θ_w	dimensionless wall temperature, $(T_w-T_{bi})/(dT_b/dz')$

ρ	density, kg/m^3
σ	standard deviation
ϕ	angular position from bend inlet

Subscripts

c	critical value
e	bend exit
i	bend inlet
180	angular position $\phi=180°$ from bend inlet

1. Introduction

1.1 Background Information

1.1.1 Buoyancy Force Effects in a Heated Curved Pipe

The flow in curved pipes is characterized by a secondary flow motion in the form of a pair of symmetric counter-rotating vortices at a cross section normal to the direction of main flow. Such secondary flow motion is the consequence of the centrifugal forces created by the curvature of bend. It is generally understood that the secondary flow motion in curved pipes promotes the mixing rate within the flow field and consequently increases the heat or mass transfer rate between working fluid and pipe wall.

If the buoyancy forces are superimposed upon the existing secondary flow motion, the description of the flow field is further complicated by the interaction of the two different body forces. The net result will depend on the orientation of the original secondary flow field due to centrifugal forces against the fixed direction of gravitational acceleration.

The laminar flow in heated curved pipes is perhaps one of the most extensively studied subjects in the fields of engineering fluid mechanics and heat transfer. Due to the wide application of curved pipes in industry, experimental and theoretical studies regarding the heat or mass transfer characteristics were made by many investigators throughout the decades [1-8].

The effect of buoyancy forces was studied only recently by Yao and Berger [9] and Prusa and Yao [10]. Subsequent numerical studies such as Futagami et al. [11], Akiyama et al. [12] and Lee, Simon and Chow [13] clarified the significance of buoyancy force effects at low Reynolds numbers for the case of horizontal flow configuration. Their common finding is that the increasing buoyancy forces increase the magnitude of secondary flow motion resulting in enhancement in heat transfer rate. A few experimental studies regarding the buoyancy force effects in curved pipe flows are available in the literature [11,12,14]. However, in view of the practical importance of the problem, further experimental investigations are needed to establish reliable design criteria and to complement the existing theoretical results.

Although the calculated results for heat transfer coefficients may be directly compared with experimental data, the detailed information for field parameters such as velocity or temperature profiles are not easy to confirm since their measurements are extremely difficult in a secondary flow field. For this reason, a flow visualization study is often employed to permit a direct comparison between calculated and observed secondary flow patterns whereby the theoretical model used in a numerical calculation may be qualitatively confirmed, e.g. [12].

Recently a flow visualization study in an isothermally heated curved pipe [15] showed some interesting flow phenomena concerning the buoyancy force effects in curved pipe flows. It appears that a similar flow visualization study for the case of uniform wall heat flux boundary condition is not available in the literature. It is noted that most numerical calculations concerning the buoyancy force effects in curved pipe flows were carried out under the uniform wall heat flux boundary conditions.

In this connection, a series of flow visualization experiments were also conducted in order to provide photographs showing buoyancy affected secondary flow patterns which may be compared with existing numerical predictions. The results are extended to the cases where the numerical solutions are not yet available. It is believed that the present flow visualization study will also provide considerable physical understanding of the buoyancy force effects in curved pipe flows.

1.1.2 Flow Visualization Studies on Convective Instability Phenomena

If a natural convection flow is induced by heating from below over a horizontal or inclined plate, the flow is potentially unstable due to the density variations occurring near the heated plate. The top-heavy situation breaks down when the destabilizing effects of buoyancy forces dominate the stabilizing effects of viscous and thermal diffusion. The result is then the occurrence of longitudinal vortex rolls which are more or less periodic in the spanwise direction. After the onset of longitudinal vortex rolls, the flow field takes a three-dimensional characteristic and conventional two-dimensional theory can no longer be applied in that flow regime.

The above buoyancy induced instability phenomenon in natural convection flow along inclined surfaces was first revealed by Sparrow and Husar [16] using an electro-chemical flow visualization technique. Subsequently, instability data regarding the onset of longitudinal vortices were obtained by Lloyd and Sparrow [17] and Lloyd [18]. These initial findings apparently motivated a series of linear stability studies on the onset of longitudinal vortex rolls in natural convection flow along inclined surfaces [19-23]. The wave instability analyses were also carried out by many investigators [24-26]. It is well established that the vortex instability has priority over the wave instability in a wide range of inclination angles from the horizontal direction.

The vortex instability problem also arises if a horizontal Blasius flow is heated from below. The linear stability theory regarding the onset of longitudinal vortex rolls in a horizontal Blasius flow was first applied by Wu and Cheng [27]. Their results were subsequently compared with the experimental instability results obtained by Gilpin, Imura and Cheng [28] using an electro-chemical flow visualization technique similar to that used in [16]. Their flow visualization results also confirmed the existence of longitudinal vortex rolls in forced convection water flow over an isothermal flat plate. Heat transfer characteristics with the presence of such vortex rolls were studied by Imura, Gilpin and Cheng [29] in water flow over an isothermal flat plate. Takimoto, Hayashi and Matsuda [30] conducted a similar experiment using air as the flow medium and also presented an analytical instability result. Recently, more refined theoretical instability results were suggested by Moutsoglou, Chen and Cheng [31].

For this particular problem, the flow visualization study has been proven to be an effective tool in revealing unexplored flow phenomena and also in complementing theoretical results [16,17,28]. The primary objective of the present experimental investigation is to provide flow visualization photographs showing the onset and subsequent growth of longitudinal vortex rolls in a natural convection flow over horizontal or slightly inclined plate and in a horizontal Blasius flow. However, it appears that experimental instability data for the natural convection case are rather limited in literature in the range of inclination angles considered in the present work. Some important aspects of convective instability for the case of horizontal Blasius flow also appears to be unexplored. These are the incentives for the present work which will be further discussed in pertinent chapters to follow.

1.2 Scope of the Study

In Chapter 2, the results of heat transfer experiments concerning the buoyancy force effects on laminar forced convection flow in curved pipes are discussed. Extensive measurements for wall temperature and local Nusselt number variations in the entrance region were carried out in a 200° pipe bend under the uniform wall heat flux boundary condition with parabolic entrance velocity profile at the start of bend .

A particular emphasis was given to the effect of buoyancy forces on heat transfer characteristics with varying inclination angle of curvature plane of the test pipe from the horizontal plane. Three different inclination angles were considered: upward vertical ($\alpha=$ 90°), horizontal flow ($\alpha=$ 0°) and downward vertical flow ($\alpha=$ -90°). Additional experiments were also conducted at α=45° and -45° to further investigate the effect of varying the inclination angle on local Nusselt number variations.

Heat transfer results for the horizontal flow case are compared with the existing theoretical and experimental results. The results for other cases are also believed to be useful for future studies.

Flow visualization photographs of the buoyancy affected secondary flow patterns for upward vertical, horizontal and downward vertical flow cases are presented in Chapter 3. The flow visualization technique was a smoke tracer method similar to that used in [15]. Observations of secondary flow patterns were made at the exit of 200° pipe bend. A comparison between the streamline patterns obtained by recent numerical solutions and the present flow visualization results is presented. A typical flow visualization result for the transient case is also presented for future reference.

The problem of convective instability in free or forced convection boundary layer flow is approached by means of flow visualization study employing a smoke injection method in Chapters 4 and 5.

In Chapter 4, the results of flow visualization studies on the onset and subsequent growth of longitudinal vortex rolls in a natural convection flow over horizontal or slightly inclined surfaces are presented. Photographs for side and top views of the flow and for cross-sectional views of the developing longitudinal vortices in the post-critical regime are presented. The effects of varying the inclination angle and wall to free stream temperature difference were investigated and the results are illustrated by photographs showing the changes in secondary flow motions. Instability data for critical Grashof number and wave length were also obtained for the range of inclination angles $\theta = 0 \sim 20°$ and comparisons were made against available theoretical and experimental results.

Chapter 5 deals with similar flow visualization experiments for the case of horizontal Blasius flow over an isothermally heated flat plate.

Attention was given to the effect of an unheated length on the instability characteristics concerning the occurrence of longitudinal vortex rolls. Instability data obtained for three different unheated lengths are presented. Flow visualization photographs are also presented for different unheated lengths.

1.3 References

1. Dean, W.R., "Note on the Motion of Fluid in a Curved Pipe," Phil. Mag. 4. 1927, pp. 208 - 223.

2. Adler, M., "Stromung in Gekrummten Rohen," Z. Angew. Math. Mech. 14, 1934, pp. 257 - 275.

3. Barua, S.N., "On Secondary Flow in Stationary Curved Pipes," Q.J. Mech. Applied. Math. 16, 1962, pp. 61 - 77.

4. Mori, Y. and Nakayama, W., "Study on Forced Convective Heat Transfer in Curved Pipes - 1. Laminar Region," Int. J. Heat Mass Transfer 8, 1965, pp. 67 - 82.

5. Seban, R.A. and McLanghlin, G.F., "Heat Transfer in Tube Coils with Laminar and Turbulent Flow," Int. J. Heat Mass Transfer 6, 1963, pp. 387 - 395.

6. Truesdell, L.C. Jr. and Adler, R.J., "Numerical Treatment of Fully Developed Laminar Flow in Helically Coiled Tubes," A.I.Ch.E. J. 16, 1970, pp. 1010 - 1015.

7. Akiyama, M. and Cheng, K.C., "Boundary Vorticity Method for Laminar Forced Convection Heat Transfer in

Curved Pipes," Int. J. Heat Mass Transfer 14, 1971, pp. 1659 - 1675.

8. Dravid, A.N., Smith, K.A., Merrill, E.W. and Brian, P.L.T., "Effect of Secondary Fluid Motion on Laminar Flow Heat Transfer in Helically Coiled Tubes," A.I.Ch.E. J. 17, 1971, pp. 1114 - 1122.

9. Yao, Lun-shin and Berger, Stanley A., "Flow in Heated Curved Pipes," J. Fluid Mech., Vol. 88, Part 2, 1978, pp. 339 - 354.

10. Prusa, J. and Yao, L.S., "Numerical Solution for Fully Developed Flow in Heated Curved Tubes," J. Fluid Mech., Vol. 123, 1982, pp. 503 - 522.

11. Futagami, K., Aoyama, Y. and Abe, F., "Forced and Free Combined Convective Laminar Heat Transfer in a Helically-Coiled Tube," Trans. Jap. Soc. of Mech. Engrs., Vol 47B, 1981, pp. 1995 - 2003.

12. Akiyama, M., Suzuki, M., Cheng, K.C., Suzuki, Mi. and Nishiwaki, I., "Mixed Convection Problem in the Entrance Region of Curved Circular Tubes," Unpublished Work.

13. Lee, Jy-ber, Simon, H.A. and Chow, J.C.F., "Buoyancy in Developed Lanimar Curved Tube Flows," Int. J. Heat Mass Transfer, Vol. 28, No. 3, 1985, pp. 631 - 640.

14. Mori, Y. and Watanabe, K., "Studies on Degradation of Heat Transfer Characteristics in Heated Pipe," Trans. Jap. Soc. of Mech. Engrs., Vol. 45, No. 357, 1979, pp. 1343 - 1353.

15. Cheng, K.C. and Yuen, F.P., "Flow Visualization Experiments of Secondary Flow Patterns in an Isothermally Heated Curved Pipe," Eds. B.F. Armaly and L.S. Yao, Mixed Convection Heat Transfer, HTD-Vol. 53, ASME, 1985, pp. 17 - 24.

16. Sparrow, E.M. and Husar, R.B., "Longitudinal Vortices in Natural Convection Flow on Inclined Plates," J. Fluid Mech., Vol. 37, 1969, pp. 251 - 255.

17. Lloyd, J.R. and Sparrow, E.M., "On the Instability of Natural Convection Flow on Inclined Plates," J. Fluid Mech., Vol. 42, 1970, pp. 465 - 470.

18. Lloyd, J.R., "Vortex Wavelength in the Transition Flow Adjacent to Upward Facing Inclined Isothermal Surfaces," Procs. 5th Int. Heat Transfer Conference, Vol. 3, 1974, pp. 34 - 37.

19. Haaland, S.E. and Sparrow, E.M., "Vortex Instability of Natural Convection Flow on Inclined Surfaces," Int. J. Heat and Mass Transfer, Vol. 16. 1973, pp. 2355 - 2367.

20. Hwang, G.J. and Cheng, K.C., "Thermal Instability of Laminar Natural Convection Flow on Inclined Isothermal Plates," Canadian J. of Chemical Engineering, Vol. 51, 1973, pp. 659 - 666.

21. Kahawita, R.A. and Meroney, R.N., "The Vortex Mode of Instability in Natural Convection Flow Along Inclined Plates," Int. J. Heat Mass Transfer, Vol. 17, 1974, pp. 541 - 548.

22. Lee, J.B. and Lock, G.S.H., "Instability in Boundary-Layer Free Convection along an Inclined Plate," Trans. Canadian Soc. for Mechanical Engineering, Vol. 1, 1972, pp. 197 - 203.

23. Chen, T.S. and Tzuoo, K.L., "Vortex Instability of Free Convection Flow over Horizontal and Inclined Surfaces," ASME Journal of Heat Transfer, Vol. 107, 1982, pp. 637 - 643.

24. Haaland, S.E. and Sparrow, E.M., "Wave Instability of Natural Convection on Inclined Surfaces Accounting for Nonparallelism of the Basic Flow," ASME Journal of Heat Transfer, 1973, pp. 405 - 407.

25. Pera, L. and Gebhart, B., "On the Stability of Natural Convection Boundary Layer Flow Over Horizontal and Slightly Inclined Surfaces," Int. J. Heat Mass Transfer, Vol. 16, 1973, pp. 1147 - 1163.

26. Iyer, P.A. and Kelly, R.E., "The Stability of the Laminar Free Convection Flow Induced by a Heated Inclined Plate," Int. J. Heat Mass Transfer, Vol. 17, 1974, pp. 517 - 525.

27. Wu, R.S. and Cheng, K.C., "Thermal Instability of Blasius Flow along Horizontal Plates," Int. J. Heat Mass Transfer, Vol. 19, 1976, pp. 907 - 913.

28. Gilpin, R.R., Imura, H. and Cheng, K.C., "Experiments on the Onset of Longitudinal Vortices in Horizontal Blasius Flow Heated from Below," ASME Journal of Heat Transfer, Vol. 100, 1978, pp. 71 - 77.

29. Imura, H., Gilpin, R.R. and Cheng, K.C., "An Experimental Investigation of Heat Transfer and Buoyancy Induced Transition from Laminar Forced Convection to Turbulent Free Convection over a Horizontal Isothermally Heated Plate," ASME Journal of

Heat Transfer, Vol. 100, 1978, pp. 429 - 434.

30. Takimoto, A., Hayashi, Y. and Matsuda, O., "Thermal Stability of Blasius Flow Over a Horizontal Flat Plate, "Heat Transfer-Japaness Research, Vol. 12, 1983, pp. 19 - 33.

31. Moutsoglou, A., Chen, T.S. and Cheng, K.C., "Vortex Instability of Mixed Convection Flow Over a Horizontal Flat Plate," ASME Journal of Heat Transfer, Vol. 103, 1981, pp. 257 - 261.

2. Buoyancy Force Effects on Laminar Forced Convection Flow in Curved Pipes

2.1 Introduction

Curved pipes are used extensively in many engineering devices such as compact heat exchangers, nuclear reactors and heat engines because of compactness and high efficiency in heat transfer. The high efficiency is due to the well-known secondary flow motion caused by centrifugal forces in the form of a pair of symmetric counter-rotating vortices at a cross section normal to the main flow. Such secondary flow motion greatly increases the heat transfer rate between the working fluid and pipe wall. Similarly, mass transfer rate is also increased due to the secondary flow motion. For this reason, curved pipes or coiled tubes are also used in various biomedical applications such as the dialyzer for an artificial kidney.

The secondary flow motion in the form of a pair of symmetric vortices is the consequence of centrifugal forces acting in the direction of the radius of curvature. The centifugal forces caused by the curved flow passage tend to push the fluid in the core region toward the outer bend. By continuity, the fluid near the outer bend then returns back to the inner bend along the wall surfaces as it is driven by the pressure gradient directed toward the inner bend. Such flow motion occurs while the fluid is in continuous movement in the axial direction. The net result is then a double helix type secondary flow motion with cross sectional view showing a pair of symmetric counter-rotating vortices. Such secondary flow motion consequently increases the mixing rate within the flow field resulting in high heat or mass transfer rate.

If there is a large temperature difference between the pipe wall and the working fluid, the density variation may become significant enough to create buoyancy forces within the existing flow field. The net outcome of interaction between buoyancy forces and centrifugal forces will depend on how the curved pipe is positioned against the fixed direction of gravitational acceleration. It is noted that theoretical analysis of such mixed convection problem is extremely difficult and so far restricted to small Dean number flow regime.

The laminar flow in curved pipes was first analyzed by Dean in his series of papers [1,2]. He has shown that the flow in curved pipes can be characterized by a single nondimensional parameter now widely known as Dean number.

$$De = Re(a/R_c)^{1/2} \qquad (2.1)$$

where Re is the Reynolds number based on diameter, and a and R_c are respectively the inside radius of pipe and the radius of curvature of the bend. This parameter represents the ratio of centrifugal force to the viscous force. Following Dean's pioneering work, Alder [3] and Barua [4] introduced Prandtl's boundary layer concept for secondary flow in analyzing the flow behaviour at high Dean numbers. Their analyses apparently laid the ground work leading to the heat transfer study by Mori and Nakayama [5]. In the mean time, a few experimental studies on the subject began to appear giving empirical correlations for heat transfer coefficients [6-9]. Numerical studies for laminar forced convection in curved pipes were carried out by Truesdel [10], Akiyama and Cheng [11] and Dravid [12]. In general, their results showed good agreement with known experimental results. Because of the broad nature of the problem, the laminar flow in heated curved pipes still remains as an interesting subject to many investigators in recent years [13-18].

For the case of straight pipe flow, buoyancy forces alone are found to be capable of inducing a secondary flow motion which results in enhancement in transport rate [19]. In this connection, it is expected that the buoyancy forces may become significant in addition to centrifugal forces for laminar forced convection in curved pipes.

The effects of buoyancy forces in heated curved pipes were studied theoretically by a few investigators such as Yao and Berger [20] and Prusa and Yao [21]. Although their results were restricted to small Dean numbers and buoyancy parameter, they clearly showed the effects of buoyancy forces on velocity and temperature profiles and heat transport rates.

Recently, Futagami et al.[22], Akiyama et al.[23] and Lee, Simon and Chow [25] presented more refined numerical results showing the significance of buoyancy effects at low Dean numbers. Experiments in some of the theoretical studies such as [22] and [23] seemed to confirm the theoretical prediction. Their common finding is that the buoyancy force effects increase the magnitude of secondary motion resulting in enhancement in heat transfer rate. However, Mori et al. [26] showed quite different results in their experimental study in a Helically coiled tube using Helium as the flow medium. They observed the degradation of heat transfer rate with increasing buoyancy force effects for relatively high Dean number flows. In this view, the theory still needs to be complemented by further experimental investigations.

The present experimental investigation is concerned with the simultaneous hydrodynamic and thermal entrance region problem in curved pipes with the consideration of buoyancy force effect. Attention is given to the variations in local Nusselt numbers in the entrance region with different orientations of the curvature plane and flow direction. Experimental measurements were carried out in order to study the buoyancy effect in curved pipe air flows using a 200° bend for three different inclination angles of the curvature plane from the horizontal direction: upward vertical ($\alpha = 90°$), horizontal ($\alpha = 0°$) and downward vertical flow ($\alpha = -90°$). The resulting experimental data for axial wall temperature distributions and Nusselt numbers are presented and compared with recent numerical and experimental results.

2.2 Experimental Apparatus

2.2.1 General Description of Test Setup

The schematic diagram of the test setup is shown in Fig. 2.1. The flow medium was air from the compressor. The air was first filtered through a Fulflo air filter and passed to the main control valve. It was then passed through a helically coiled soft copper tube of 15 mm i.d. with a coil diameter 305 mm immersed in a large water reservoir at room temperature to help minimize the temperature fluctuation in the incoming air flow. The total length of the coiled tube was 9 m. The flow rate was measured using a laminar flow element. Details of the flow rate measurements will be given in a later section. Shown next in the flow circuit is the smoke generation facility used in the flow visualization study which will be reported in the following chapter. For heat transfer experiments, the smoke generation facility was by-passed.

The settling chamber was designed to reduce the turbulence levels in the incoming air flow using a series of screens. Its large contraction ratio at the exit (1:0.12) provided a fairly uniform air flow. The length of the hydrodynamic entrance tube was 3.65 m which was long enough to ensure a fully developed velocity profile for both laminar and turbulent flows. After passing through the heated test section and the mixing box, the air was ejected into the environment.

2.2.2 Curved Pipe and Heating Arrangement

The curved pipe used in this experimental investigation was fabricated by bending a 1.905 I.D. copper tube using an aluminium die after packing the inside tube with sand. Its total length was 0.772 m and the curvature ratio a/R_c of the resulting bend was 0.045. As a result of cold working, a slight deformation in the shape of circular cross section was found at both ends of the curved pipe. The measurements for the average diameter of the deformed circular cross section made at the bend inlet are given in Fig. 2.2 (b).

The curved pipe was first wrapped with a fiberglass tape in order to electrically insulate the tube wall from the heater. The heater was made from a nichrome tape(1.88 Ω/m) of 3.18×0.2 mm, width by thickness. It was carefully wound over the test section with a constant pitch of 1 cm. The resulting total resistance of the heater was 11 ohm.

A compensation heater was used to compensate for the conduction heat loss near the bend exit where the mixing box was to be connected. It was made from a nichrome tape similar to that used for the main heater and installed over approximately 4 diameter length with its pitch being gradually reduced toward the bend exit. The insulation between the main and compensation heater was rendered by wrapping the fiberglass tape over the main heater. The entire test section was tightly wrapped with fiberglass wool and finally with rubber insulation (see Fig. 2.2 (c)). The insulation thickness was gradually increased from 3cm to 7cm from the start of bend toward the bend exit.

Heat conduction to the upstream entrance tube was prevented by employing an acrylic resin flange and asbestos discs for the connection between the entrance tube and the curved pipe. The flange at the entrance tube side was designed in such a way that the curved pipe may be rotated at every 45° angle whereby the inclination angle of the curvature plane can be easily varied to provide upward vertical to downward vertical flow. The detailed design of the flange system is shown in Fig. 2.3.

2.2.3 Wall Temperature Measurement

In order to obtain a detailed wall temperature distribution in the entrance region, a total of 46 copper-constantan thermocouples (0.25mm d) were used for wall temperature measurements. In view of the possibility of peripheral wall temperature variations, either two or six thermocouples were installed at a given cross section resulting in 15 measuring sections. The approximate axial locations of the 15 measuring sections are shown in Fig. 2.2 (a) together with a list of the corresponding nondimensional axial distance from the bend inlet. Symbols indicating the positions of the two different thermocouple arrangements are described as well. Each of the thermocouples was soldered on the tube outside wall and at least 1.5cm of surface contact was ensured before it was led out of the tube wall in order to prevent conduction heat losses through the thermocouple wire.

2.2.4 Bulk Temperature Measurement

The mixing box used for the exit bulk temperature measurements in the present experimental work is shown in Fig. 2.4. The design of the mixing cup is similar to that of Futagami and et al. [22]. The incoming hot air with temperature gradients is first disturbed by a series of stainless steel blades fixed at the entrance of the mixing box. After Passing through a series of partitions having alternating flow passages, the incoming hot air is expected to be well mixed. The bulk temperature was measured by the thermocouple installed in the fifth compartment. Mixing was further promoted by filling all other compartments with thin copper chips. The mixing box was made of acrylic resin and a double-walled design was used to minimize the heat loss from the mixing compartments. The temperature gradient of mixed air was checked by traversing the thermocouple across the diameter of the center hole in the fourth partition. A maximum temperature variation of 3 % of the temperature at the center of the hole was observed. This temperature variation was incorporated as the typical measurement error for the exit bulk temperature measurements in the error analysis of the experimental data.

The center temperature at the bend inlet was measured and used as the inlet bulk temperature with the assumption that it would not significantly differ from the actual inlet bulk temperature. The resulting measurement error for typical cases is discussed in Appendix I. The bulk temperatures were all measured by 0.13mm copper-constantan thermocouples. The incoming air temperature was also recorded by a 0.3mm copper-constantan thermocouple at the exit of settling chamber. The property values for the computations of mass flow rates and Dean numbers were based on this unheated air temperature measurement.

2.2.5 Flow Rate Measurement

The flow rate of air was measured by a Meriam laminar flow element (model 50MW20-1) employing a Validyne differential pressure transducer. A straight tube of approximately 20 diameter length was connected to both ends of the laminar flow element to meet the requirements for ordinary flow meters. The diaphragm used in the pressure transducer was applicable within 0 ~ 22.5cm of water (0 ~ 0.32 psi). It was calibrated in the range of 0 ~ 12.4 cm of water using an inclined manometer. No significant linearization error was observed in curve-fitting the calibration data points. The pressure drop read by the pressure transducer was converted to air flow rates using the calibration curve provided by the maker. An Airbar manometer was simultaneously used to measure the pressure drop in the laminar flow element. The reading from the manometer agreed well with that from the pressure transducer.

2.3 Auxiliary Systems

2.3.1 AC Power Source and Constant Wattage Control System

AC power source was used for both the main and the compensation heater. In order to prevent the main heater from being affected by any cyclic variations or voltage drifts occurring in the external power supply, a feed back system was employed to maintain a constant power input. Fig. 2.5 shows the circuit diagram for the constant wattage control system used in the present experiments. The power input range to the main heater was 3 W to 90 W. No controlling device was used for the compensation heater. The power input to the compensation heater varied from 0.1 W to 2 W depending on each experimental run.

2.3.2 Vacuum Vessel

To avoid heat losses from the test section, a vacuum vessel of simple design was also used for a few additional sets of experiments. The vacuum vessel was fabricated from 6.35mm steel plates in the form of rectangular box. Its inside dimensions were 66.0×53.3×22.9 cm, length by width by depth. The top lid was made of acrylic resin in order to facilitate visual inspection. The sealing between the top lid and the vacuum box was provided by using rubber sheets with silicone sealant. The thermocouple wires and other electric wires to be connected to the external systems were all passed through a pipe fitting. The sealing was provided by filling the space between wires with epoxy in the pipe fitting. Several pieces of wood bars were used as internal bracing to prevent the vacuum box from being collapsed. The rest of the space in the box was filled with cellulose type insulation to further reduce heat losses. A maximum vacuum of 660 mmHg was obtained using a vane type vacuum pump. In order to sustain the maximum vacuum load, the vacuum pump had to be in continuous operation during the course of a complete experimental run.

2.3.3 Data Acquisition System

The data acquisition system consists of an Hewlett Packard 85 micro-computer and a Hewlett Packard 3497A data acquisition control unit which has a built-in reference junction in each of the thermocouple cards. The hard copy output of the experimental results was provided by a Digital Decwriter IV printer.

2.4 Experimental Procedure

2.4.1 Calibration of Thermocouples

The 46 thermocouples installed on the test pipe for wall temperature measurements were calibrated in-situ against a HP-2807A quartz thermometer in a constant temperature hot water tank. All other thermocouples for the bulk and unheated air temperature measurements were also calibrated. The capacity of the hot water tank was 389 liters. The heating elements and the water temperature were regulated by a PID temperature and power controller with a maximum power input of 3.7 kilowatts. The large capacity of the tank with the help of a motor-driven stirrer could provide quite a uniform temperature field with a maximum temperature variation of 0.1°C in the region where the curved pipe and thermocouples were located. Calibration data were taken at four temperature levels ranging from 20° to 80°C. The largest error resulting from linearization was less than 0.2°C. The calibration was also later confirmed by checking at the room temperature.

2.4.2 Start-up of Heating and Data Acquisition Procedure

For each experimental run, the flow rate was first set to a desired value using the main control valve. After confirming the steady flow, the heating system was turned on and adjusted to a fixed heat input. Next the data aquisition system was started and the flow rate, heat input to the main heater, time, date and etc. are fed into the main program as input data. The system was switched on at least 6 hours before any experimental run to ensure stabilization. The compensation heater was also turned on and the heat input was carefully increased while the system was in continuous operation until it reached steady-state conditions.

Prior to the actual experimental runs, a few preliminary runs were made without using the compensation heater. Indeed a sudden decrease in the axial wall temperature distribution was observed at the last one or two thermocouple stations. It was initially assumed that this sudden temperature drop is due to the increased heat loss near the bend exit and must be compensated by using a compensation heater in order to follow the overall trend of the axial wall temperature distribution. Based on this assumption, the heat input to the compensation heater was carefully controlled by observing the axial wall temperature distribution periodically in such a way that the peripherally averaged wall temperatures at last four measuring sections can be fit into one straight line.

The data acquisition system was programed to monitor and record the thermocouple temperatures at half an hour intervals. Each record was composed of an average of three readings. The time required by the system for a complete set of readings was approximately 20 seconds. The steady-state conditions were assumed to have been reached if all of the wall temperatures did not change by a specified tolerance over half an hour interval. The tolerance was set to be 0.1°C when the maximum wall temperature did not exceed 120°C. For the case of higher maximum wall temperatures, 0.2°C was found to be suitable.

2.5 Data Analysis

Experimental data were obtained at seven different Dean numbers for a given inclination angle of the curvature plane. The Dean numbers selected for this experimental work were 100, 150, 200, 300, 430, 600 and 800. The heat input to the main heater was varied from 3 W to 90 W. For a fixed Dean number, three to six different heat input levels were used and the resulting maximum wall temperatures ranged from 32°C to 180°C. The experiments were conducted for three different flow configurations, i.e. upward vertical ($\alpha = 90°$), horizontal ($\alpha = 0°$) and downward vertical ($\alpha = -90°$) cases. A few additional runs were also made for $\alpha = 45°$ and $-45°$ to further study the effect of varying the inclination angle of the curvature plane of the curved pipe with Dean number 100, 150 and 200.

The raw data obtained by the data acquisition system were the wall temperatures read by the 46 thermocouples, peripherally averaged axial wall temperatures, the inlet and exit bulk temperatures and the unheated air temperature. The flow rate was directly fed into the main program as an input data from the calibration curve for laminar flow element. The kinematic viscosity and density of the unheated air were evaluated using the following equations [27].

$$\rho = 3.4833\times10^{2}\ P/T \quad [\ \mathrm{kg/m^3}\ ] \qquad (2.2)$$

$$\nu = \mu/\rho = 1.488\times10^{-6}T^{3/2}/(118+T)/\rho \quad [\ \mathrm{m^2/s}\ ] \qquad (2.3)$$

where P [bar] and T [°K]

A value of 1.013 [bar] was used for the atmospheric pressure throughout the experiments. However, the mean Edmonton pressure was 0.934 bar. The heat received by the flowing air through the test section is calculated and compared with the actual heat input to the main heater to yield the overall heat loss to the environment. The following simple energy balance was used.

$$Q_{rec.} = m\ C_p(T_{be} - T_{bi}) \qquad (2.4)$$

$$Q_{loss} = Q_{input} - Q_{rec.} \qquad (2.5)$$

where m is the mass flow rate of unheated air flow, and T_{be} and T_{bi} are the exit bulk temperature measured by the mixing box and the inlet bulk temperature, respectively. The specific heat of air C_p was evaluated using the arithematic mean of T_{be} and T_{bi}.

The uniform wall heat flux boundary condition was assumed in the present study. Then, the local heat transfer coefficient h_x can be computed from

$$q_w = h_x\ (T_w - T_b\ ) \qquad (2.6)$$

where q_w is the uniform wall heat flux per unit area, and T_w and T_b are the local wall temperature and bulk air temperature, respectively. The wall heat flux is simply the total heat received by the air calculated by Eq.(2.4) divided by the total heated inner surface area of tube and given as

$$q_w = Q_{rec.} /(\pi dL) \tag{2.7}$$

The local wall temperature is the peripheral mean at each measuring section, and the local bulk air temperature is interpolated using the inlet and exit bulk temperature measurements by assuming a linear variation. The wall temperature at the 15th measuring section was to be directly subject to a mannual control of compensation heater as described in section 2.4.2. In order to reduce the effects of possible human error, the local wall temperature at the 15th measuring section is replaced by that extrapolated using the three preceeding local wall temperature measurements. This is done in the data processing program employing a least square curve-fitting scheme. The local peripherally averaged wall temperatures and the corresponding local bulk air temperatures are used to compute the local heat transfer coefficients from Eq. (2.6).

The local Nusselt numbers are then calculated from the definition

$$Nu = h_x d/k \tag{2.8}$$

where k is the thermal conductivity of air evaluated at local bulk temperature. The values of k are interpolated from the tabulated values given in [28] employing a cubic-spline interpolation scheme.

For convenience, an average heat transfer was also defined by the following equation

$$q_w = h_{av}\ (\Delta T_i + \Delta T_{180})/2 \qquad (2.9)$$

where ΔT_i and ΔT_{180} are the wall to bulk temperature difference at the bend inlet and at $\phi = 180°$, respectively.

Then, the average Nusselt number is defined accordingly as

$$Nu_{av} = h_{av} d/k \qquad (2.10)$$

The dimensionless parameter for the axial distances used in plotting the local Nusselt number distributions is the inverse Gratz number defined as

$$z = (x/d)/(RePr) \qquad (2.11)$$

where x is the local axial distance from the bend inlet and d is the tube inside diameter. The kinematic viscosity used in the calculation of Re is based on the unheated air temperature. A constant of 0.71 was used for Pr.

In presenting the wall temperature distributions, the following dimensionless temperature was used.

$$\theta_w = (T_w - T_{bi})/(dT_b/dz') \qquad (2.12)$$

$$\theta_b = (T_b - T_{bi})/(dT_b/dz') \qquad (2.13)$$

$$\text{where } dT_b/dz' = \frac{(T_{be} - T_{bi})}{L/a} \qquad (2.14)$$

$$\text{and } z' = x/a$$

These definitions had been used in [12] and [29].

The buoyancy parameters used in plotting the experimental results are the Grashof number and Rayleigh number. For convenience, two different definitions were used for the Grashof number, i.e.

$$Gr_{av} = g\beta[(\Delta T_{180} + \Delta T_i)/2]\ a^3/\nu^2 \qquad (2.15)$$

and
$$Gr = g\beta[(T_{be} - T_{bi})/L]\ a^4/\nu^2 \qquad (2.16)$$

where $(T_{be} - T_{bi})/L$ is the bulk temperature gradient.

The Rayleigh number is defined using the Grashof number based on the bulk temperature gradient and the Prandtl number, i.e.

$$Ra = GrPr \qquad (2.17)$$

$Pr = 0.71$ was used for air throughout the experiments.

2.6 Results and Discussion

2.6.1 Axial and Peripheral Wall Temperature Distributions

Typical axial wall temperature distributions at different Dean numbers for the horizontal flow case are shown in Fig. 2.6. Each data point represents the peripherally averaged wall temperature at a local axial position. For De=149, the wall temperature distribution is practically linear. For higher Dean numbers, some variations in the axial wall temperature distribution can be observed. However, the general trend is that the axial wall temperatures begin to increase monatonically at a certain axial distance more or less parallel to the assumed linear bulk temperature. The approximately linear wall temperature distribution seems to confirm the uniform wall heat flux boundary condition assumed in the present study.

Fig. 2.7 shows the peripheral wall temperature distribution obtained with increasing buoyancy force effects at De= 150 for horizontal flow case. Although some temperature variations can be observed, they were within the experimental error.

2.6.2 Local Nusselt Number Variation

The local Nussel number variations in the entrance region are given in Fig. 2.8 for developing laminar flow. The curves are the numerical solutions obtained by Akiyama et al. [23]. It should be mentioned that the numerical solutions were obtained with the condition of fully developed curved pipe flow at the thermal entrance. The theoretical results shown are for reference only. Numerical solution with the same inlet condition as the present experiments, i.e. parabolic velocity profile at the start of thermal entrance region, does not appear to be available.

In general the data obtained by the present experiments are below the numerical solutions in the entrance region. A possible reason will be the large thermal conductivity of the copper tube wall which tends to even out the axial wall temperature distribution in the entrance region.

However one notices that the Nusselt numbers near the fully developed region seem to be in good agreement with those predicted by numerical solution for Dean numbers higher than 200. It was initially assumed that both the velocity and temperature fields would be fully developed by the end of test section for the range of Dean numbers considered in the present experiments. Once the flow field is fully developed both hydrodynamically and thermally, the asymtotic Nusselt numbers should be independant of entry flow condition. In this respect, it may be mentioned that the present data supports the asymtotic Nusselt numbers predicted by theory for Dean number higher than 200. For the case of De=100 and 150, however, the experimental data fall much below those predicted by theory. Particularly the asymtotic Nusselt number for De=100 is even lower than that of the straight pipe flow case. This suggests some doubts about the accuracy of the present data at low Dean numbers. Some possible reasons for this trend will be mentioned in later part of the discussions.

2.6.3 The Study of Buoyancy Effect at Fixed Inclination Angle of Curvature Plane

The study of buoyancy effect in the present investigation was two-fold. Firstly, the effect of increasing buoyancy parameter ReRa was studied at a given inclination angle α of the curvature plane from the horizontal plane. Secondly, attention was focused in the effect of varying inclination angle for a fixed buoyancy parameter ReRa.

Figures 2.9 and 2.10 show the typical axial wall temperature profiles and the local Nusselt number distributions at different buoyancy parameters for the case of horizontal flow at De=150. Although the trend is not clearly shown in the figure due to too small temperature variations, the dimensionless temperature differences $(\theta_w-\theta_b)$ at any axial position are observed to increase with increasing ReRa.

The resulting local Nusselt numbers then decrease with increasing ReRa as shown by Fig. 2.10. In Fig. 2.11, the variations of local Nusselt number at $\phi=180°$ with increasing buoyancy parameter are shown for Dean numbers 150, 200, 300, 430, 600 and 800. The buoyancy parameter is the Grashof number based on the arithematic mean of the wall to bulk temperature differences at the inlet and at $\phi=180°$. As mentioned earlier, the Nusselt number at this angular position is close to the asymtotic value in the fully developed region. The trend of decreasing Nusselt number with increasing buoyancy effect is observed well up to Dean number 430. Fig. 2.12 shows a similar plot for average Nusselt numbers. The average Nusselt number is based on the heat transfer coefficient defined by Eq.(2.9). In this case, the trend of decreasing Nusselt number is also observed but only at Dean number 150 and

200.

Figures 2.13 through 2.16 show similar plots obtained for the case of upward vertical and downward vertical flow. It suffices to mention that the trend discussed earlier is consistently observed for all flow configurations considered in this experimental work.

In fact, the trend of decreasing Nusselt number with increasing buoyancy parameter is in direct contradiction with that shown by recent numerical calculations [22,23,25]. Fig. 2.17 shows the comparison between typical results of recent numerical calculations and the present experimental data for horizontal flow configuration. The theoretical results are due to Akiyama et al. [23]. The data for the ratio of local Nusselt number at ϕ=180° to the asymtotic value (Nu_s=4.36) for straight pipe flow were plotted against Dean numbers. The experimental data are grouped in four different ranges of buoyancy parameter ReRa and are distinguished by different symbols. The theory predicts that the buoyancy forces are significant only in low Dean number range and tend to increase the asymtotic Nusselt number as the buoyancy parameter is increased. It is clear that the present experimental data show similar but directly opposite trend to that of theory. Furthermore the actual values of the ratio Nu_{180}/Nu_s obtained by present experiments seriously deviate from those predicted by theory especially in the low Dean number range.

Fig. 2.18 shows a plot of Nu_{180}/Nu_s versus Gr/De^2. The parameter Gr/De^2 was successfully used by Akiyama et al. [24] in correlating the buoyancy force effects in curved square duct flow. The Grashof number is based on the axial bulk temperature gradient. It appears that the parameter Gr/De^2 is not adequate for the present case.

It is noted that an experimental work regarding the buoyancy effects in a Helically coiled tube has been undertaken by Mori et al. [26] using Helium as the flow medium under the uniform wall heat flux boundary condition with fully developed flow. They observed the phenomenon of degrading heat transfer coefficients in the thermal entrance region with the effect of buoyancy forces.

Typical of their results showing the local Nusselt number distributions with the presence of buoyancy force effects in the entrance region is shown in Fig. 2.19 (a). Nu_o/Nu_c is the ratio of local Nusselt number to fully developed Nusselt number. The value of x/d at ϕ=180° for the present study is 34.7. A plotting showing the region of heat transfer degradation is also given in Fig. 2.19 (b). The dimensionless heat flux parameter q_i^+ is defined as [26]

$$q_i^+ = (d/T_{bi})(dT_b/dx)/4 \qquad (2.18)$$

The range of q_i^+ for the present work is tabulated in Table 2.1 and also plotted as solid bars in (b) of Fig. 2.19. Although the range of experimental parameters given in [26] is in general higher than that of the present study, one may observe that the present data are in the region of heat transfer degradation found in [26].

Table 2.1 Range of q_i^+ for the Present Experiments

De	ReRa	q_i^+
100	$1.67\times10^4 \sim 2.94\times10^4$	$0.001 \sim 0.002$
150	$1.34\times10^4 \sim 4.34\times10^4$	$0.0004 \sim 0.002$
200	$1.56\times10^4 \sim 6.49\times10^4$	$0.0003 \sim 0.002$
300	$1.72\times10^4 \sim 9.10\times10^4$	$0.0002 \sim 0.002$
430	$1.94\times10^4 \sim 1.25\times10^5$	$0.0002 \sim 0.002$
600	$1.93\times10^4 \sim 1.63\times10^5$	$0.0001 \sim 0.002$
800	$2.13\times10^4 \sim 2.20\times10^5$	$0.0001 \sim 0.002$

In view of these discrepancies between theoretical and experimental results, some discussions on the validity of the present experimental results may be worthwhile and they are given in detail in section 2.6.5.

2.6.4 The Study of Buoyancy Effect with Variation of α

Regardless of the disagreement with theory found in the previous study of buoyancy effects, the present study reveals an interesting physics arising from the change of flow configuration.

The centrifugal forces caused by the curvature of bend always act from inner bend toward outer bend and a pair of symmetric counter-rotating vortices exists in a cross-section normal to the main flow regardless of changing flow configuration. However, the effect of buoyancy forces depends on the orientation of the curvature plane and the resulting secondary flow interacts with the existing secondary flow field.

For upward vertical flow, the buoyancy forces assist the centrifugal forces up to angular position 90° from the bend inlet increasing the magnitude of existing secondary flow. Passing a cross section at 90°, the two forces oppose each other. Such interaction of the two forces will result in relatively high heat transfer in the region $0° < \phi < 90°$ and low heat transfer in $90° < \phi < 180°$. If the bend is laid horizontally, the directions of two forces are perpendicular to each other throughout the test section. As shown by recent numerical calculations, the secondary flow field becomes skewed and is not symmetric. The numerical studies provide a skewed secondary flow pattern and predict enhancement in heat transfer rate with increasing buoyancy effect. For downward vertical flow, the effect of buoyancy forces is directly opposite to that of upward vertical flow case and the heat transfer mechanism is also expected to be opposite. The above-described interaction between the buoyancy force and the centrifugal force with respect to varying inclination angle α is illustrated by schematic diagrams shown in Fig. 2.20.

Figures 2.21 and 2.22 show the variations in the axial wall temperature distributions and local Nusselt number distributions for different inclination angles of the curvature plane. The Dean number and wall heat flux were fixed for all three cases and the value of ReRa was the largest in this investigation for Dean number 150. Although the temperature variations are small, the effects of the interaction between buoyancy forces and centrifugal forces can be clearly observed. Attention is focused on the behaviour of two axial wall temperature distributions obtained for upward vertical flow (α=90°) and for downward vertical flow (α=-90°) where the trends are directly opposite to each other. The nondimensional bulk temperatures computed from Eq.(2.13) and (2.14) are fixed with a value (L/a) at ϕ=200° and 0 at ϕ=0°. As a result, a lower value of θ_w at a given dimensionless axial distance means a smaller wall to bulk temperature difference which in turn implies a larger heat transfer coefficient. The opposite is true for a larger value of θ_w at a given dimensionless axial distance. The two cases for α=90° and -90° are directly comparable as they show increasing and decreasing trend respectively relative to each other. The cross over between these two trends occurs near the 9th data point (z'=35.5) which was obtained at the measuring section located very close to ϕ=90°.

The plot of corresponding local Nusselt number distributions shown in Fig. 2.22 summerizes the effect of buoyancy forces with respect to the changing inclination angle of the curvature plane discussed up to this point. Two more sets of data were added at $\alpha=45°$ and $-45°$ to demonstrate the consistency of the observed trend. It is clearly shown that the heat transfer is enhanced in the region where buoyancy forces are in phase with centrifugal forces and the opposite is true in the region where the two forces are out of phase.

Fig. 2.23 shows the variation of the ratio of Nu_{180}/Nu_s depending on both the inclination angle of the curvature plane and the buoyancy effects. It is clear that the effect of changing flow configuration becomes more prominent with increasing buoyancy parameters. As already shown by the results of heat transfer study for given flow configurations, the Nusselt number at $\phi=180°$ consistently decreases as the value of ReRa increases. Comparing the data at different values of inclination angles, it is found that the ratio Nu_{180}/Nu_s for downward vertical case is slightly higher and decreases as the curvature plane shifts from downward to upward vertical flow. This is obviously the consequence of the changing mechanism of buoyancy forces with the change in the inclination angle of the curvature plane.

Fig. 2.24 shows a similar plot for the local Nusselt number at $\phi=0°$. The effect of inclination angle of the curvature plane is seen to be rather small at the start of heating. This is apparently due to the fact that the combined effect of buoyancy and centrifugal forces is yet to be developed in this region. However it is noted that the trend of data is directly opposite to that of Fig. 2.23. These observations are in agreement with the trends of local Nusselt number distributions shown in Fig. 2.22.

2.6.5 Results of Error Analysis and Additional Experiments Using Vacuum Vessel

The error analysis regarding the accuracy of the present measurements is given in Appendix I. The linearization error in thermocouple calibration and possible errors in bulk temperature measurements, flow rate and dimensions of the test pipe were all taken into account and the resulting mean fractional error in heat transfer coefficients turned out to be 10.4 % for the worst case. It should be mentioned that the error associated with the interpolation of tabulated property values was neglected in this error analysis. Such error analysis, however, does not account for any failure in measurement systems or deficiencies inherent in the present experiments.

One of the major problems encountered throughout this investigation was large heat loss at low flow rates. Nearly 50 % of the total heat input was found to be lost at De=100, and the heat loss gradually decreased with increasing Dean number or increasing flow rates. Although the heat transfer coefficients were calculated from the heat received by the flowing air based on bulk temperature measurements, the large heat loss casts some doubts about the validity of the present results especially for low Dean number range.

In an effort to explain the problem of large heat loss, the flow rate measurement system was first checked. The laminar flow element was later calibrated against a gas flow meter which had a proven accuracy of less than 1 %. The calibration curve initially used throughout the present experiments was checked at each Dean number used in the present work. It turned out that the flow rate data obtained from the existing calibration curve were 6 to 10 % higher than the true volume flow rates. This error in flow rate will result in larger heat losses. The resulting difference in heat transfer data associated with this measurement error in volume flow rates is found to result in 6 to 10 % reduction in the existing heat transfer coefficients. However no corrections were made since the change in heat transfer coefficients was within the experimental error calculated by the error analysis mentioned earlier.

One other possible source of error regarding the large heat loss at low Dean numbers lies in the mixing-cup bulk temperature measurements. The accuracy of the present experimental results depends to a large extent on the exit bulk temperature measurement using the mixing box described in section 2.2.4. The present mixing box seemed to give reasonable bulk temperature measurements at high Dean numbers in view of reasonable agreement with known theoretical results (see Fig. 2.8). On the other hand, the increasing heat loss and too low Nusselt numbers obtained by the present experiments at De=100 and 150 may suggest some deficiency of the mixing-cup bulk temperature measurements at low flow rates. One possible deficiency may be the heat loss from the mixing box at lower flow rates. Such drawback of the mixing box may result in lower exit bulk temperature measurements which in turn lower the heat transfer coefficients. It may also be potentially responsible for the decreasing heat transfer coefficient with increasing heat load as the heat loss from the mixing box will increase. In order to check this possible problem in mixing cup bulk temperature measurements, a few experimental runs were carried out for typical cases with improved insulation employing a vacuum vessel described in section 2.3.2.

Fig. 2.25 shows the local Nusselt number variations for typical Dean numbers with negligible buoyancy effects. The pressure in the vessel was 660 mmHg vacuum. The heat loss was decreased by 10 % for all cases as a result of improved insulation. The new data clearly show significant change in the trend of local Nusselt number distributions especially in the fully developed region as compared with those shown in Fig. 2.8. A sudden rise of local Nusselt number near the fully developed region is consistently observed. Such trend apparently indicates the effect of reduced heat loss from the mixing cup due to improved insulation. However it does give an impression of somewhat abnormal asymtotic behaviour of local Nusselt number. A few more sets of data were taken with large heat input and the results are compared with the previous study on buoyancy effects in Fig. 2.26. The new data are shown as solid points and the symbols indicating different values of ReRa are in conformance with those of open data points. One notices a considerable increase in the ratio Nu_{180}/Nu_s for low Dean number range as compared with the previous data. This may suggest that the heat loss from the mixing box was significantly reduced. One also finds the ratio Nu_{180}/Nu_s again decreases with increasing value of ReRa. From this result, it may be mentioned that the trend of decreasing Nusselt number with increasing ReRa value is still observed even with improved insulation.

2.7 Concluding Remarks

Experiments were performed to study the effect of buoyancy forces in the laminar forced convection air flow in curved pipes.

The curved pipe used in the present investigation was a 200° copper bend being subject to the uniform wall heat flux boundary condition with parabolic inlet velocity profile. Attention was given to the effects of buoyancy forces on heat transfer with varying inclination angle of the curvature plane of bend from the horizontal direction. Measurements for wall temperature distributions and Nusselt numbers were made at De=100, 150, 200, 300, 430, 600 and 800 for three different inclination angles: upward vertical ($\alpha=90°$), horizontal ($\alpha=0°$) and downward vertical ($\alpha=-90°$).

In the range of present study, it was found that the increasing buoyancy forces decrease the local and average Nusselt number for all of the three different inclination angles. Such finding is in direct contradiction with the results of known numerical calculations [22,23,25] for fully developed flow. It appears that the present work on buoyancy effect in curved pipes, is inconclusive and further work is required to clarify the discrepancies.

The study of the effect of buoyancy forces with varying inclination angle of the curvature plane showed that the local Nusselt numbers are relatively higher in the region where the buoyancy force and the centrifugal force assist each other, and the opposite is true in the region where the two forces oppose each other.

For future studies, the following suggestions can be made;

1. Use the largest possible tube diameter to obtain a wider range of buoyancy parameter.
2. The ratio, L/d must be increased to ensure the fully developed axial temperature distribution.

3. It is suspected that the mixing box used in the present study may not be adequate for heat transfer experiments at low Dean numbers. Therefore, the design of the mixing box needs to be further improved.
4. Improved insulation is suggested in view of the large heat losses observed at low Dean numbers. At present, a vacuum vessel of refined design is considered to be the most suitable means of insulation.

2.8 References

1. Dean, W.R., "Note on the Motion of Fluid in a Curved Pipe," Phil. Mag. 4, 1927, pp.208-223.
2. Dean, W.R., "The Stream-line Motion of Fluid in a Curved Pipe." Phil. Mag. 5, 1928, pp.673-695
3. Adler, M., "Stromung in Gekrummten Rohen," Z.Angew. Math. Mech. 14, 1934, pp.257-275.
4. Barua, S.N., "On Secondary Flow in Stationary Curved Pipes," Q.J. Mech. Applied. Math. 16, 1962, pp.61-77.
5. Mori, Y. and Nakayama, W., "Study on Forced Convective Heat Transfer in Curved Pipes - 1.Laminar Region," Int. J. Heat Mass Transfer 8, 1965, pp.67-82.
6. Berg, R.R. and Bonilla, C.F., "Heating of Fluids in Coils," Trans. N.Y. Acad. Sci. 13, 1950, pp.12.
7. Seban, R.A. and McLanghlin, G.F., "Heat Transfer in Tube Coils with Laminar and Turbulent Flow," Int. J. Heat Mass Transfer 6, 1963, pp.387-395.
8. Kubair, V. and Kuloor, N.R., "Heat Transfer to Newtonian Fluids in Coiled Pipes in Laminar Flow," Int. J. Heat Mass Transfer 9, 1966, pp.63-75.
9. Shchukin, V.K., "Correlation of Experimental Data on Heat Transfer in Curved Pipes," Thermal Engng 16, 1969, pp.72-76.

10. Truesdell, L.C. Jr. and Adler, R.J., "Numerical Treatment of Fully Developed Laminar Flow in Helically Coiled Tubes," A.I.Ch.E. J. 16, 1970, PP.1010-1015.

11. Akiyama, M. and Cheng,K.C., "Boundary Vorticity Method for Laminar Forced Convection Heat Transfer in Curved Pipes," Int. J. Heat Mass Transfer 14, 1971, pp.1659-1675.

12. Dravid, A.N., Smith, K.A., Merrill, E.W. and Brian, P.L.T., "Effect of Secondary Fluid Motion on Laminar Flow Heat Transfer in Helically Coiled Tubes," A.I.Ch.E. J. 17, 1971, pp.1114-1122.

13. Kalb, C.E. and Seader, J.D., "Heat and Mass transfer Phenomena for Viscous Flow in Curved Circular Tubes," Int. J. Heat Mass Transfer 15, 1972, pp.801-817.

14. Austin, L.R. and Seader, J.D., "Fully Developed Viscous Flow in Coiled Circular Pipes," A.I.Ch.E. J. 19, 1973, pp.85-94.

15. Tarbell, J.M. and Samuels, M.R., "Momentum and Heat Transfer in Helical Coils," Chem. Engng. 5, 1973, pp.117-127.

16. Patankar, S.V., Pratap, V.S. and Spalding, D.B., "Laminar Flow and Heat Transfer in Helically Coiled Pipes," J. Fluid Mech. 62, 1974, pp.539-551.

17. Singh, S.P.N. and Bell, K.T., "Laminar Flow Heat Transfer in a Helically coiled Tube," Paper FC5.3 in Proceedings of the 5th International Heat Transfer Conference, Tokyo, 1974.

18. Janssed, L.A.M. and Hoogendoorn, C.J., "Laminar Convective Heat Transfer in Helically Coiled Tubes," Int. J. Heat Mass Transfer, Vol. 21, 1978, pp.1197-1206.

19. Morton, B.R., " Laminar Convection in Uniformly Heated Horizontal Pipes at Low Rayleigh Numbers," Quart. J. Mech. Appl. Math. 12, 1959, pp.61-77.

20. Yao, Lun-shin and Berger, Stanley A., "Flow in Heated Curved Pipes," J. Fluid Mech., Vol. 88, Part 2, 1978, pp.339-354.

21. Prusa, J. and Yao, L.S., "Numerical Solution for Fully Developed Flow in Heated Curved Tubes," J. Fluid Mech., Vol. 123, 1982, pp.503-522.

22. Futagami, K., Aoyama, Y. and Abe, F., "Forced and Free Combined Convective Laminar Heat Transfer in a

Helically-Coiled Tube," Trans. Jap. Soc. of Mech. Engrs., Vol 47B, 1981, pp.1995-2003.

23. Akiyama, M., Suzuki, M., Cheng, K.C., Suzuki, Mi. and Nishiwaki, I., "Mixed Convection Problem in the Entrance Region of Curved Circular Tubes," Unpublished Work.

24. Akiyama, M., Kikuchi, K., Cheng, K.C., Suzuki, M. and Nishiwaki, I., "Mixed Laminar Convection of the Thermal Entry Region in Curved Rectangular Channels," ASME-JSME Thermal Engineering Joint Conference, Vol. 3, 1983, pp. 27 - 33.

25. Lee, Jy-ber, Simon, H.A. and Chow, J.C.F., "Buoyancy in Developed Laminar Curved Tube Flows," Int. J. Heat Mass Transfer, Vol. 28, No.3, 1985, pp.631-640.

26. Mori, Y. and Watanabe, K., "Studies on Degradation of Heat Transfer Characteristics in Heated Pipe," Trans. Jap. Soc. of Mech. Engrs., Vol. 45, No. 357, 1979, pp.1343-1353.

27. Fujii, T., Kato, Y. and Mihara, K., "Expressions of Transport and Thermodynamic Properties of Air, Steam and Water," Institute of Industrial Science, Kyushu University, 1977.

28. Kays, William M. and Crawford, Michael E., "Convective Heat and Mass Transfer," Second Edition, McGraw-Hill Inc, 1980.

29. Abul-Hamayel, Mohammad A., "Heat Transfer in Helically Coiled Tubes with Laminar Flow," Ph.D. Thesis, Oklahoma State University, 1979.

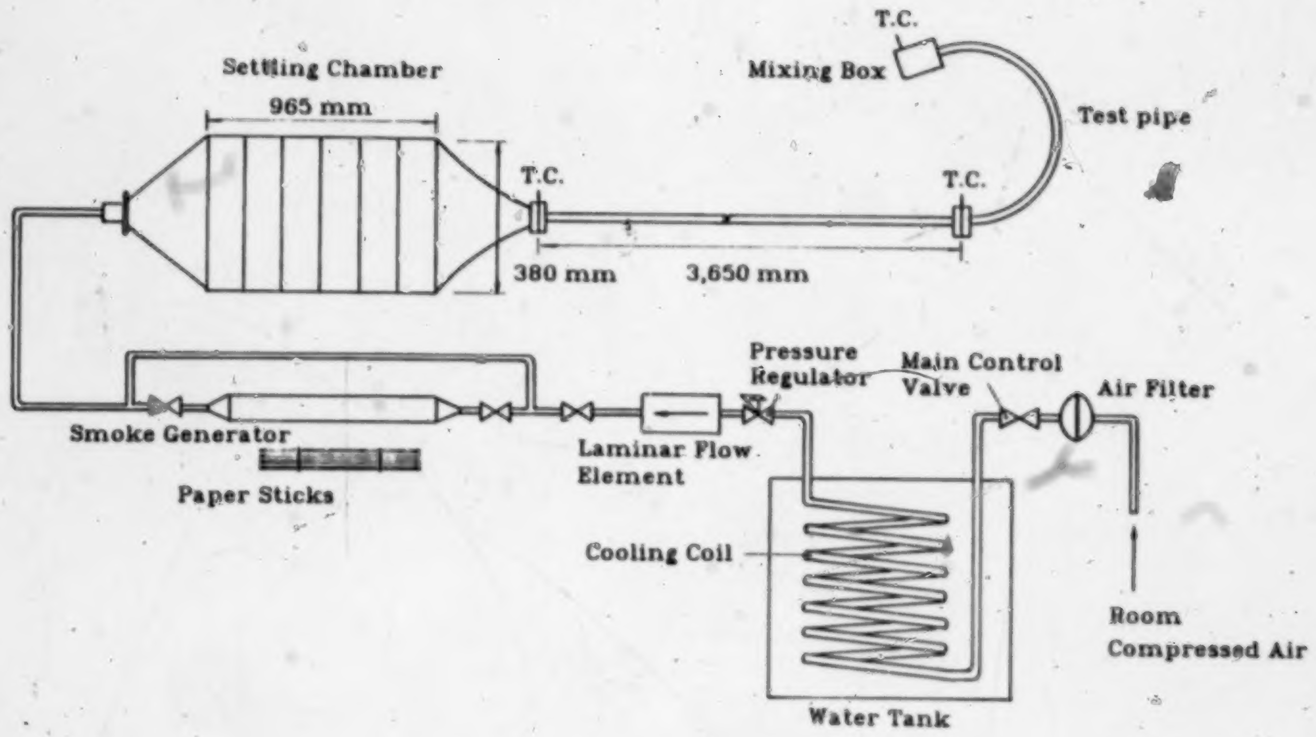
Settling Chamber
965 mm
T.C.
Mixing Box
T.C.
Test pipe
T.C.
380 mm
3,650 mm
Pressure
Regulator
Main Control
Valve
Air Filter
Smoke Generator
Paper Sticks
Laminar Flow
Element
Cooling Coil
Room
Compressed Air
Water Tank

Fig. 2.1 Schematic Diagram for Test Setup

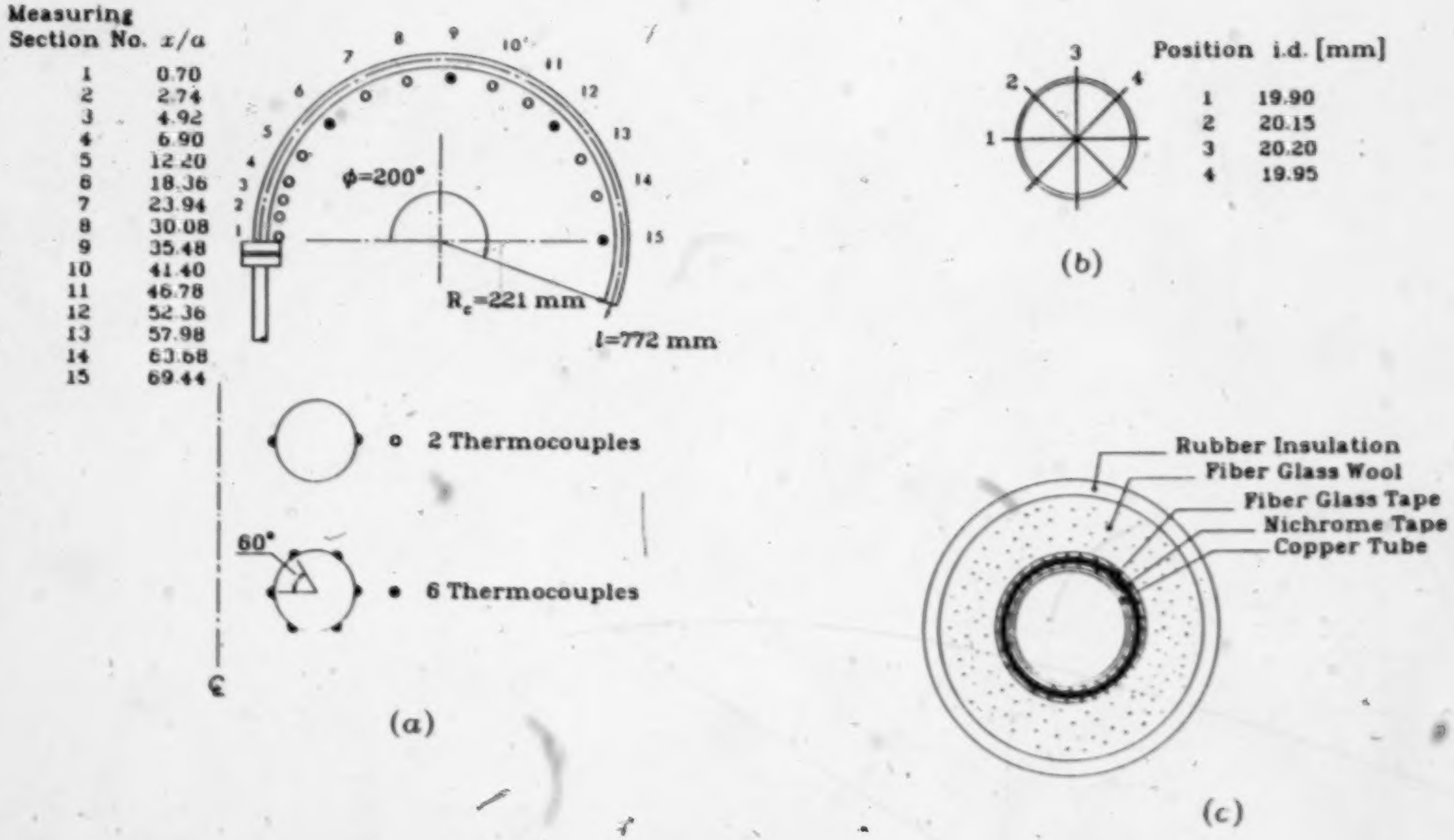

ϕ=200°
R_c=221 mm
l=772 mm
1
2
3
4
5
6
7
8
9
10'
11
12
13
14
15
○ 2 Thermocouples
● 6 Thermocouples
60°
℄
(a)
1
2
3
4
(b)
Rubber Insulation
Fiber Glass Wool
Fiber Glass Tape
Nichrome Tape
Copper Tube
(c)

Measuring Section No.	x/a
1	0.70
2	2.74
3	4.92
4	6.90
5	12.20
6	18.36
7	23.94
8	30.08
9	35.48
10	41.40
11	46.78
12	52.36
13	57.98
14	63.68
15	69.44

Position	i.d. [mm]
1	19.90
2	20.15
3	20.20
4	19.95

Fig. 2.2 Locations of Thermocouples and Curved Pipe Dimensions

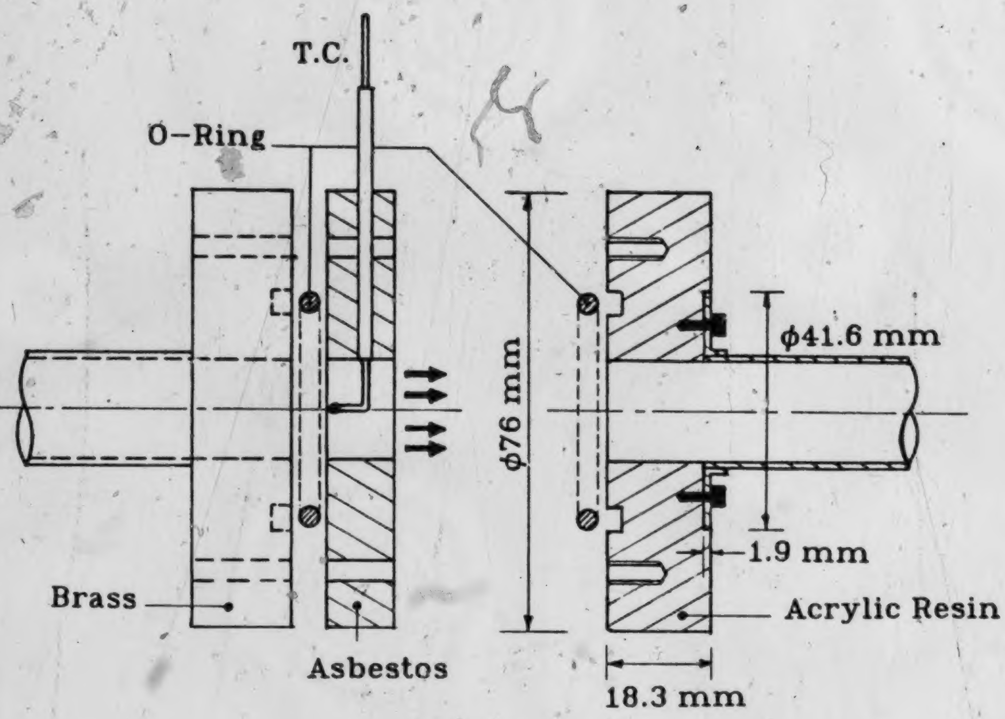
T.C.
O-Ring
Brass
Asbestos
ϕ76 mm
ϕ41.6 mm
1.9 mm
Acrylic Resin
18.3 mm

Fig. 2.3 Flange at the Bend Inlet

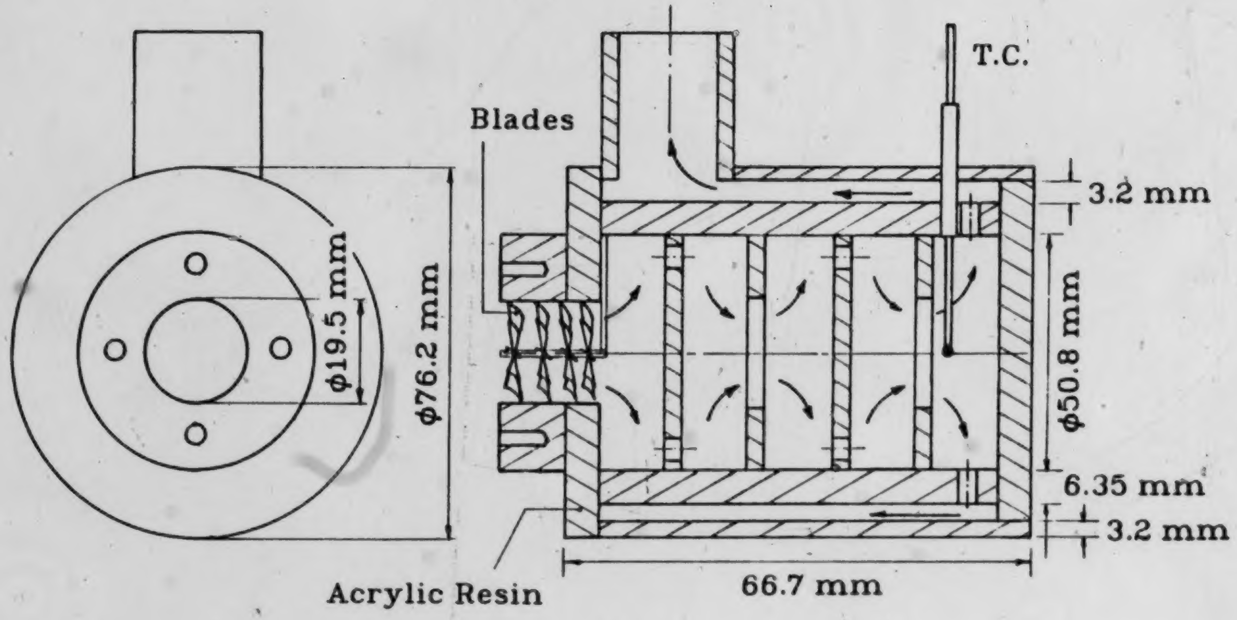
Blades
T.C.
3.2 mm
φ19.5 mm
φ76.2 mm
φ50.8 mm
6.35 mm
3.2 mm
Acrylic Resin
66.7 mm

Fig. 2.4 Schematic Diagram for Mixing Box Design

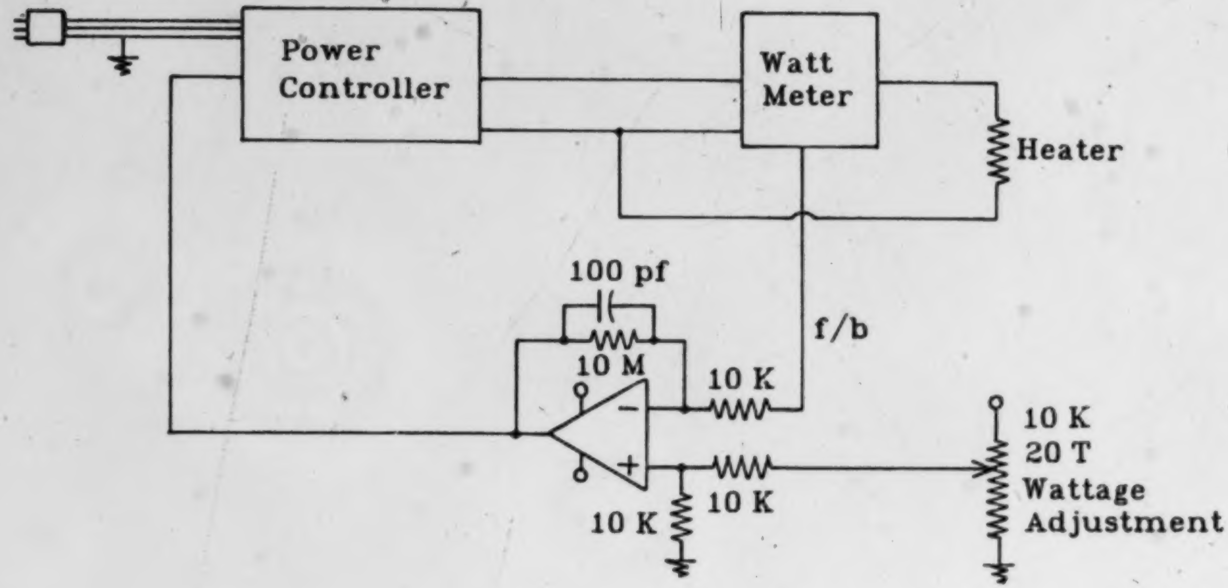
Power Controller
Watt Meter
Heater
100 pf
10 M
10 K
f/b
10 K
10 K
10 K
10 K
20 T
Wattage Adjustment

Fig. 2.5 Circuit Diagram for Constant Wattage Controller

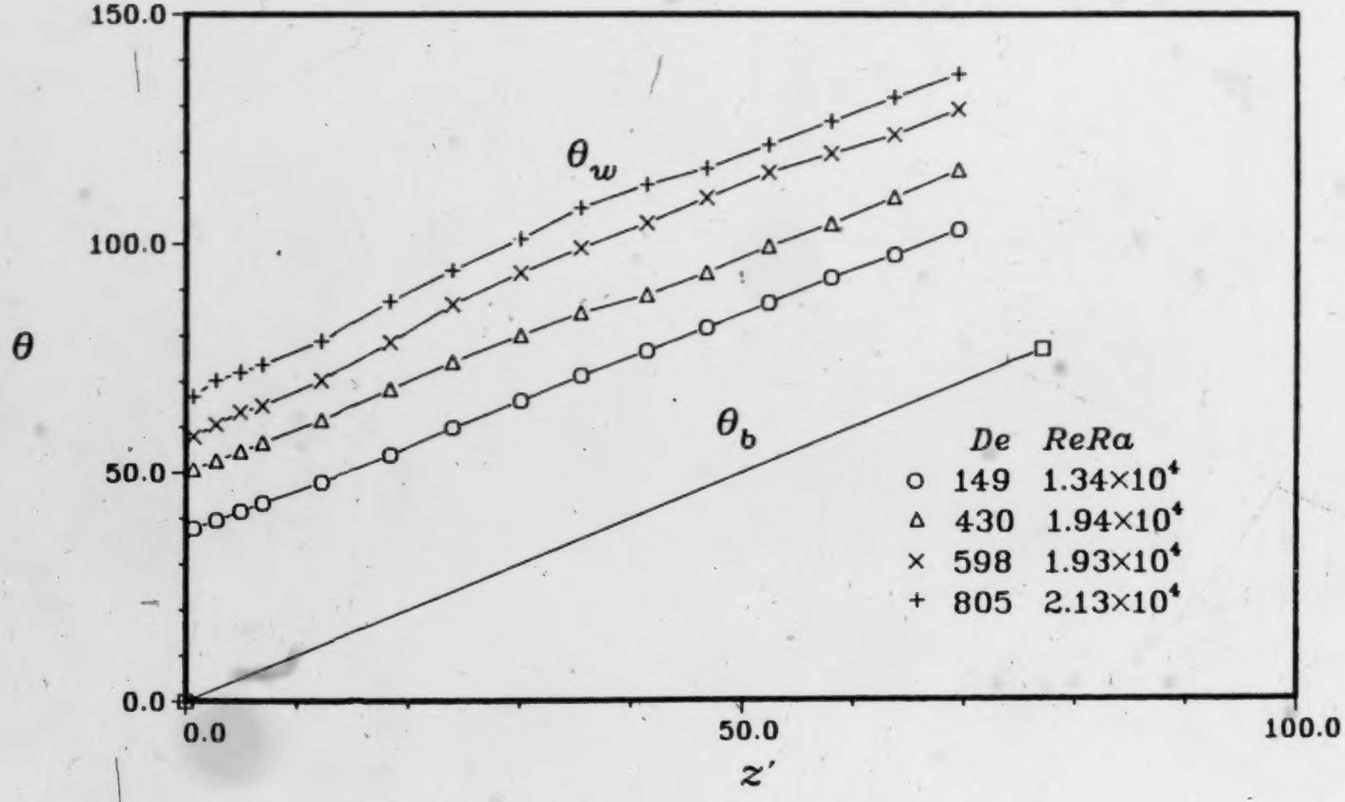

Fig. 2.6 Axial Wall Temperature Distribution for Horizontal Curved Pipe Flow

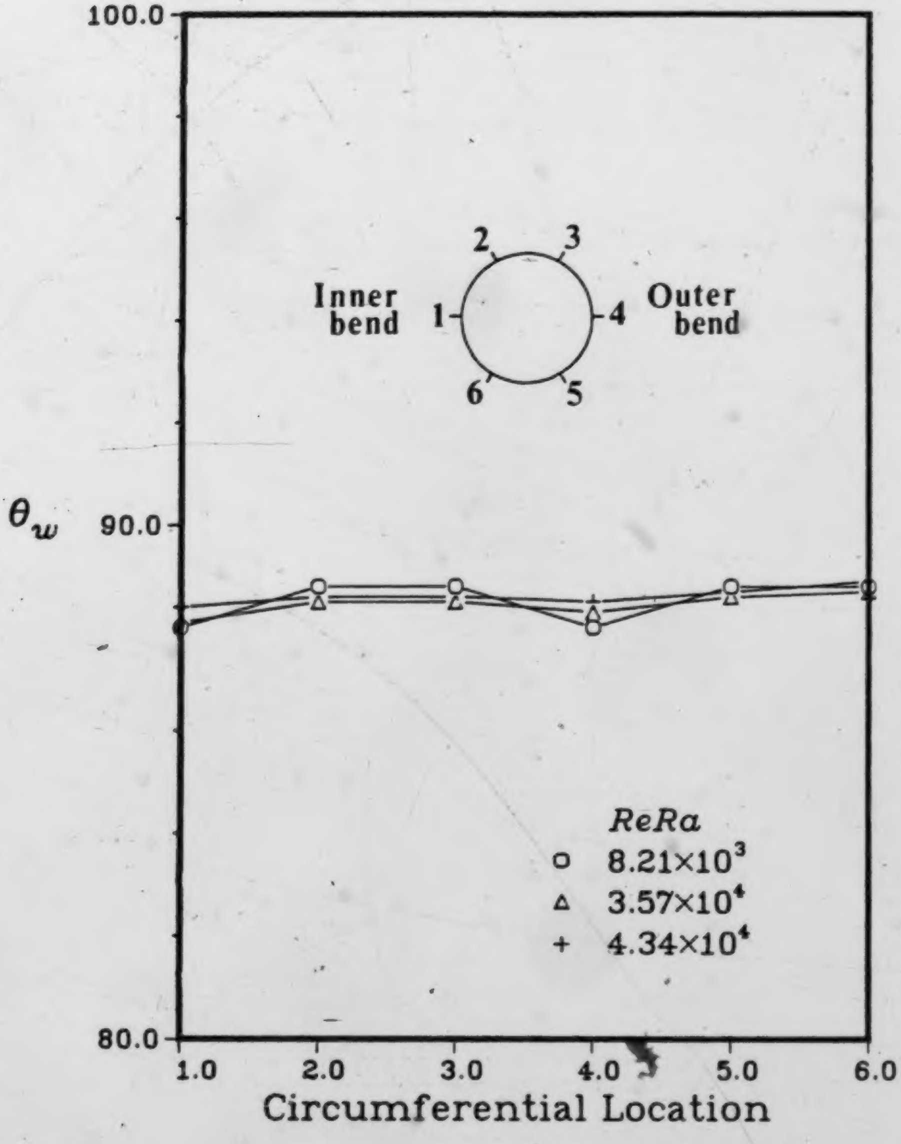

Fig. 2.7 Peripheral Wall Temperature Distribution for Horizontal Curved Pipe Flow at De= 150, ϕ= 135°

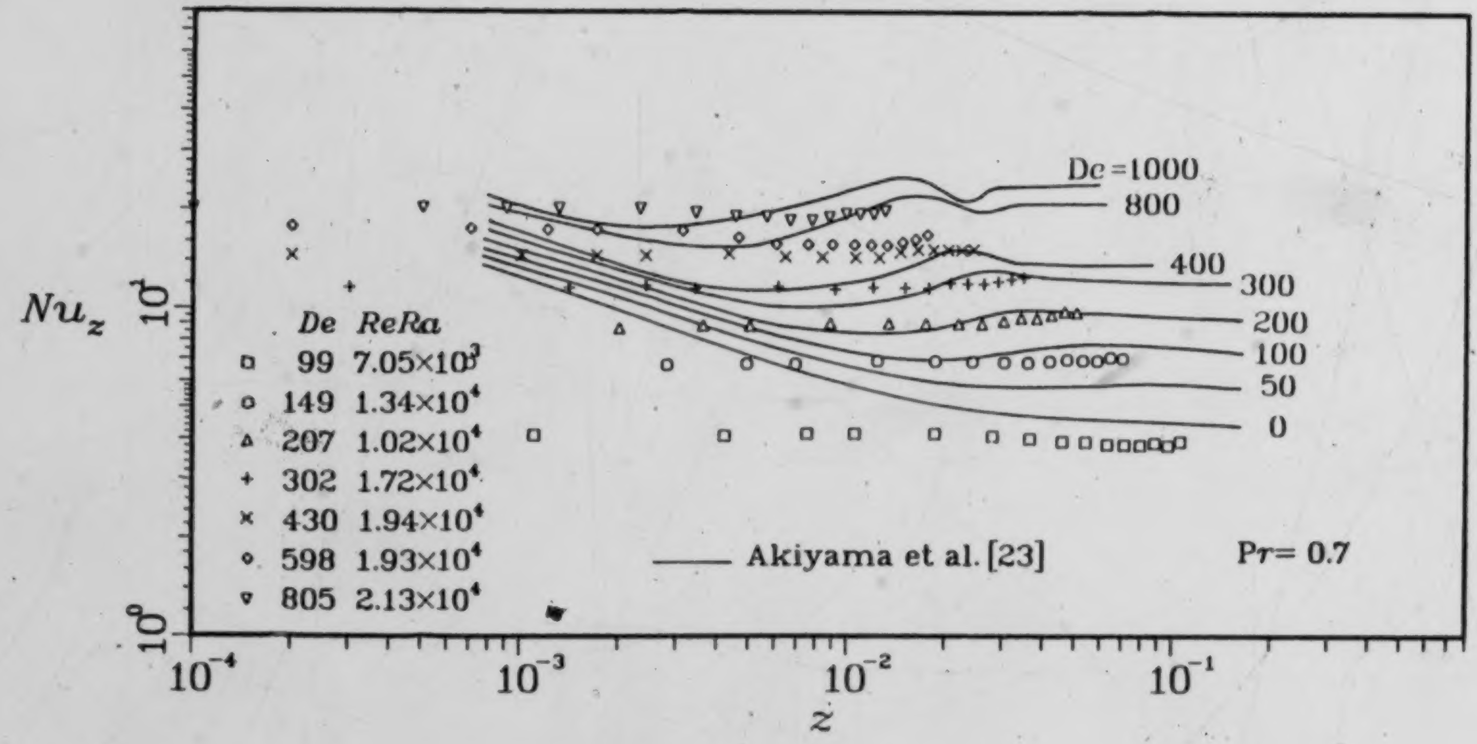

Fig. 2.8 Local Nusselt Number Variation for Horizontal Curved Pipe Flow

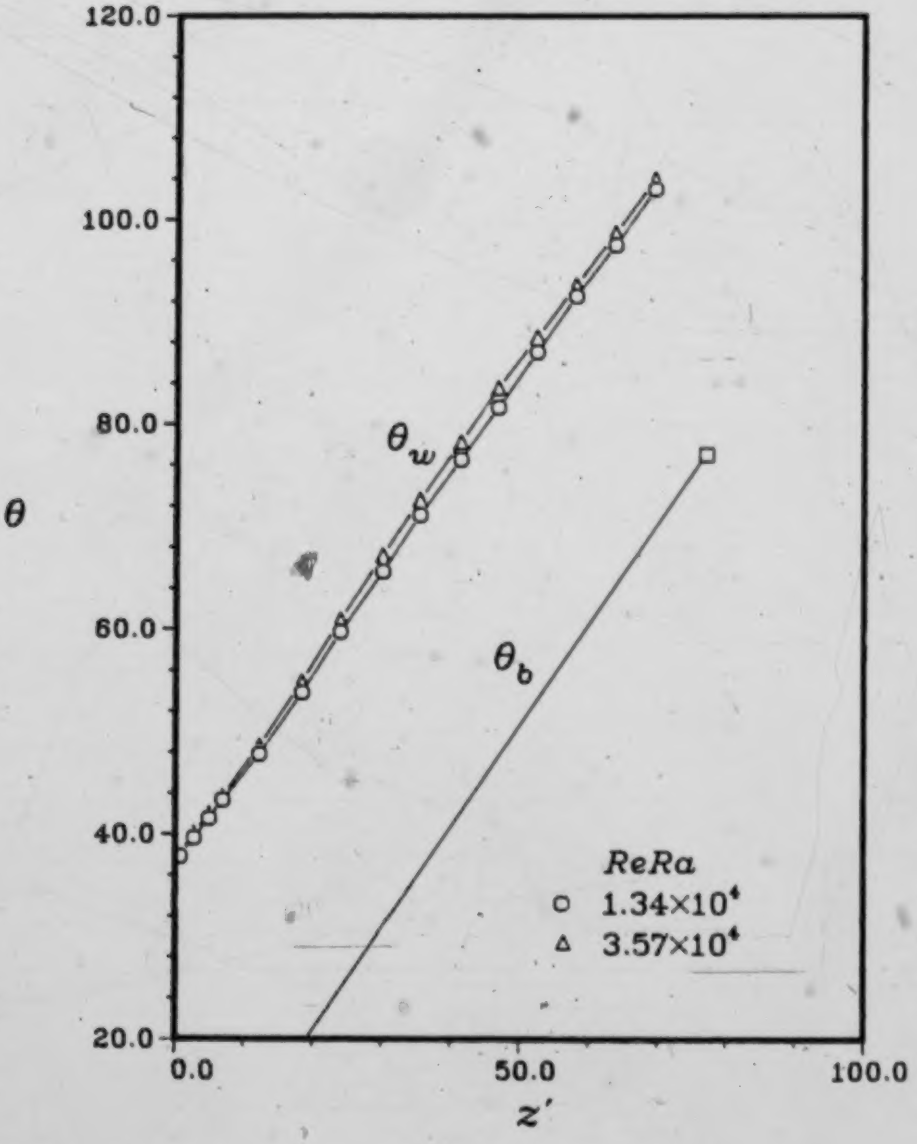

Fig. 2.9 Axial Wall Temperature Distribution for Horizontal Curved Pipe Flow at De= 150 with ReRa as Parameter

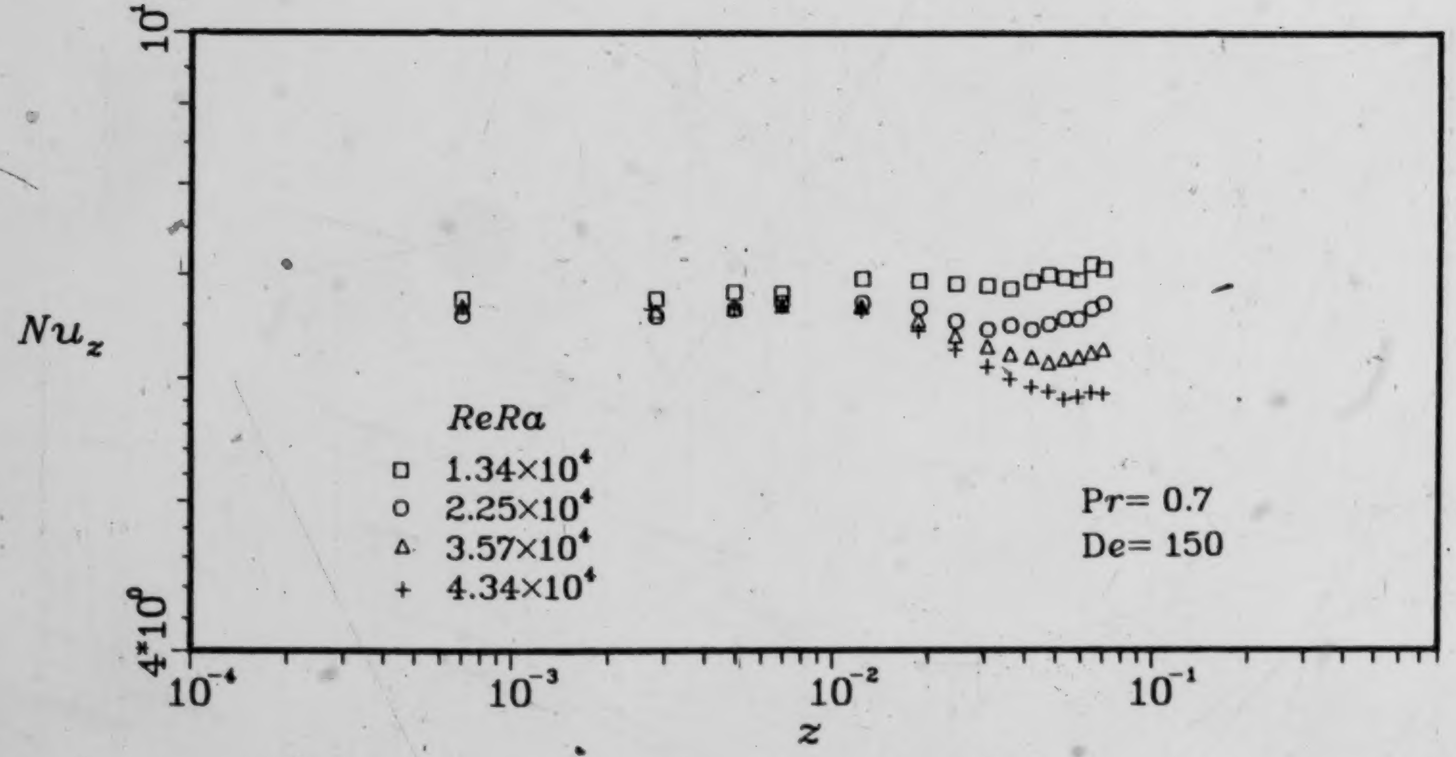

Fig. 2.10 Local Nusselt Number Variation for Horizontal Curved Pipe Flow at De= 150 with ReRa as Parameter

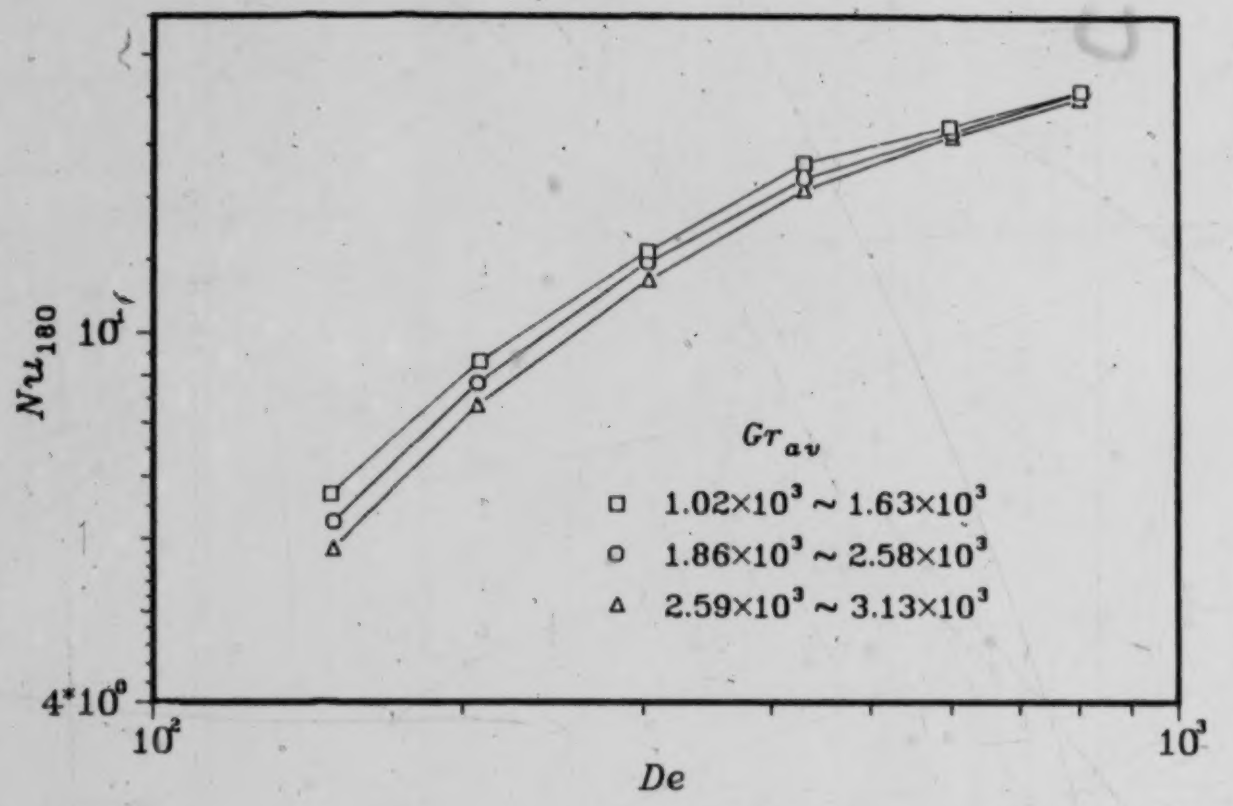

Fig. 2.11 Nu_{180} vs. De for Horizontal Curved Pipe Flow with Gr_{av} as Parameter

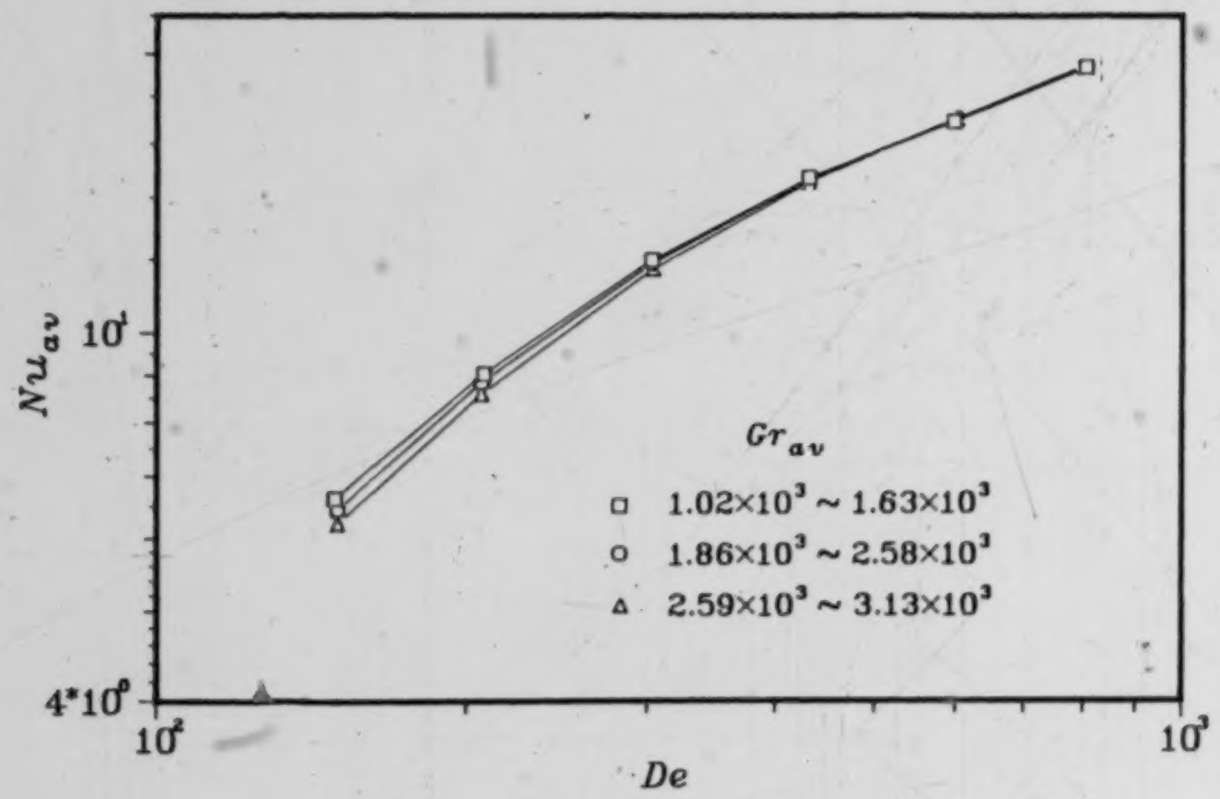

Fig. 2.12 Nu_{av} vs. De for Horizontal Curved Pipe Flow with Gr_{av} as Parameter

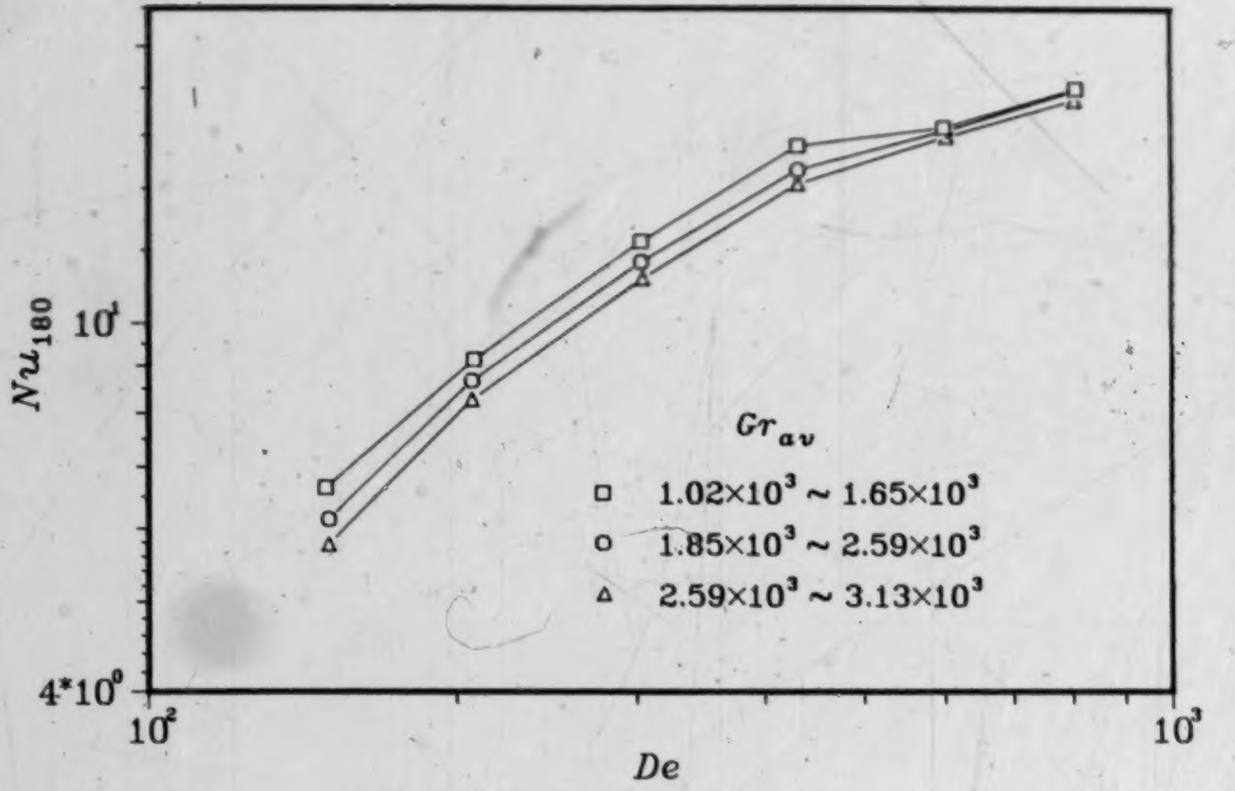

Fig. 2.13 Nu_{180} vs. De ' for Upward Vertical Curved Pipe Flow with Gr_{av} as Parameter

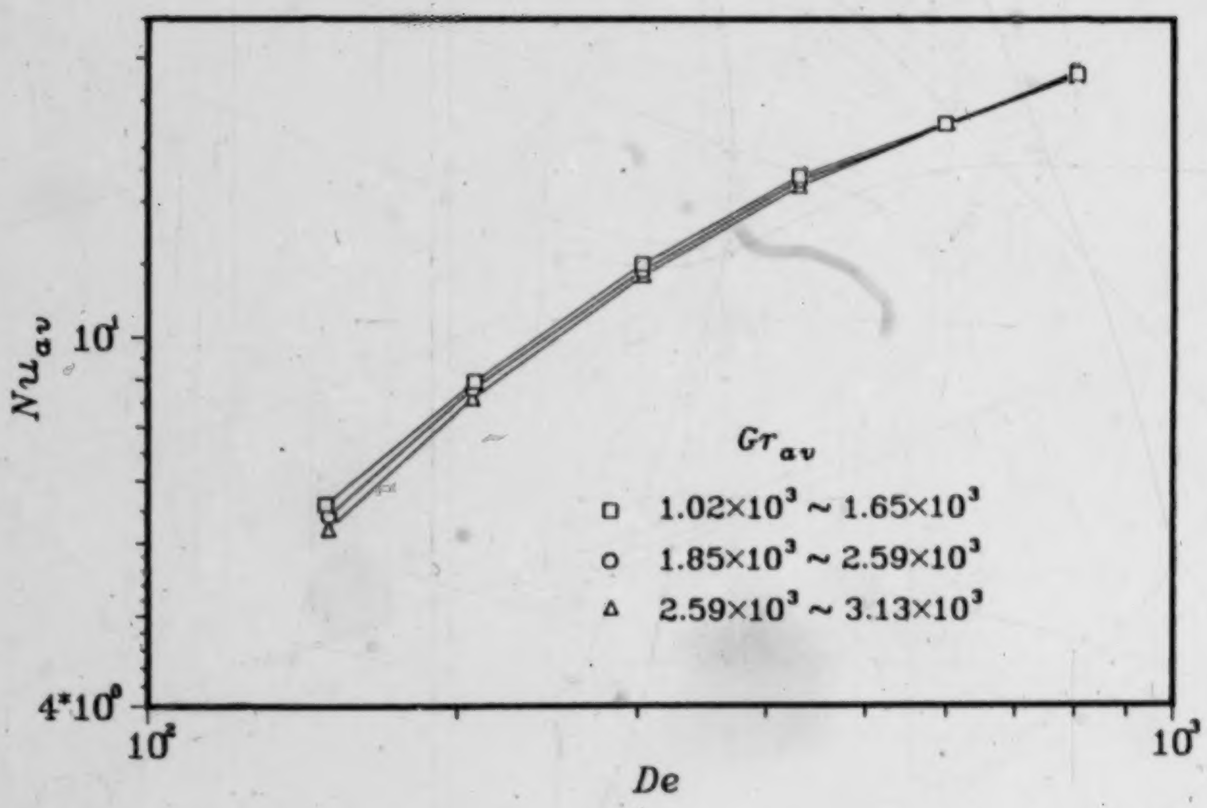

Fig. 2.14 Nu_{av} vs. De for Upward Vertical Curved Pipe Flow with Gr_{av} as Parameter

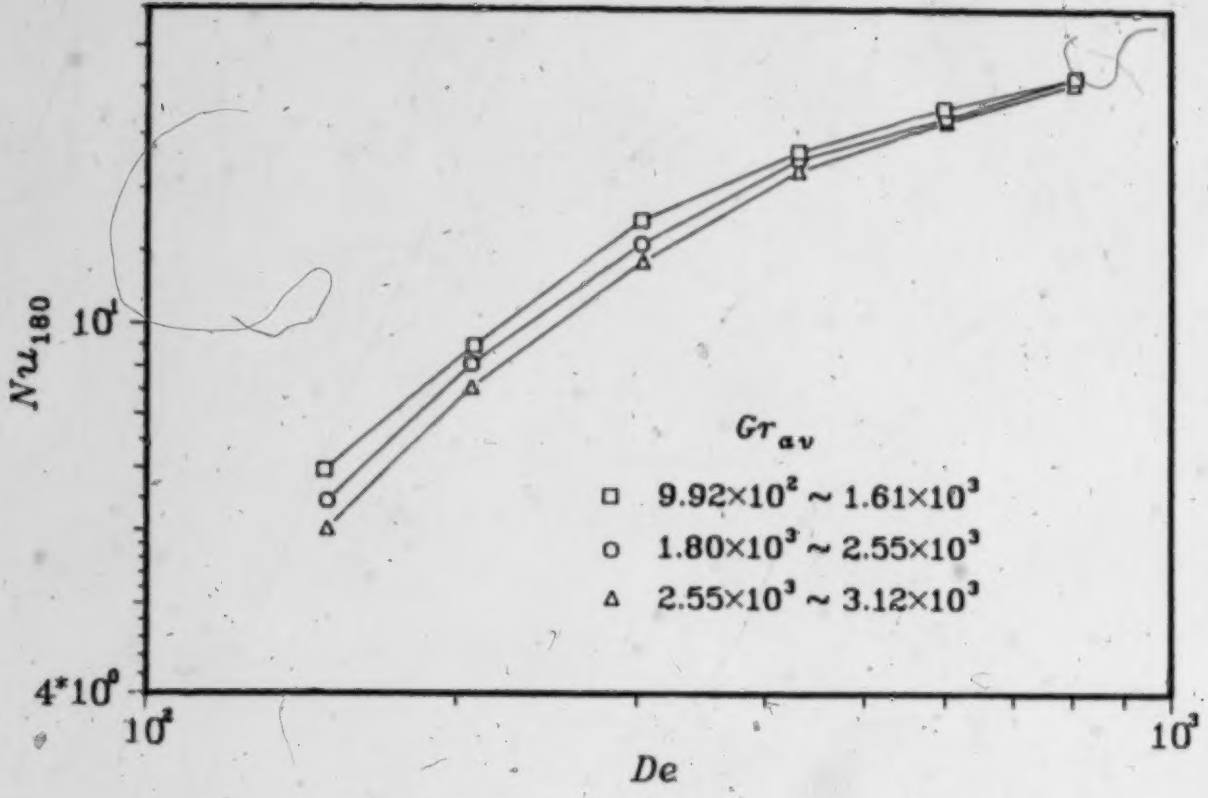

Fig. 2.15 Nu_{180} vs. De for Downward Vertical Curved Pipe Flow with Gr_{av} as Parameter

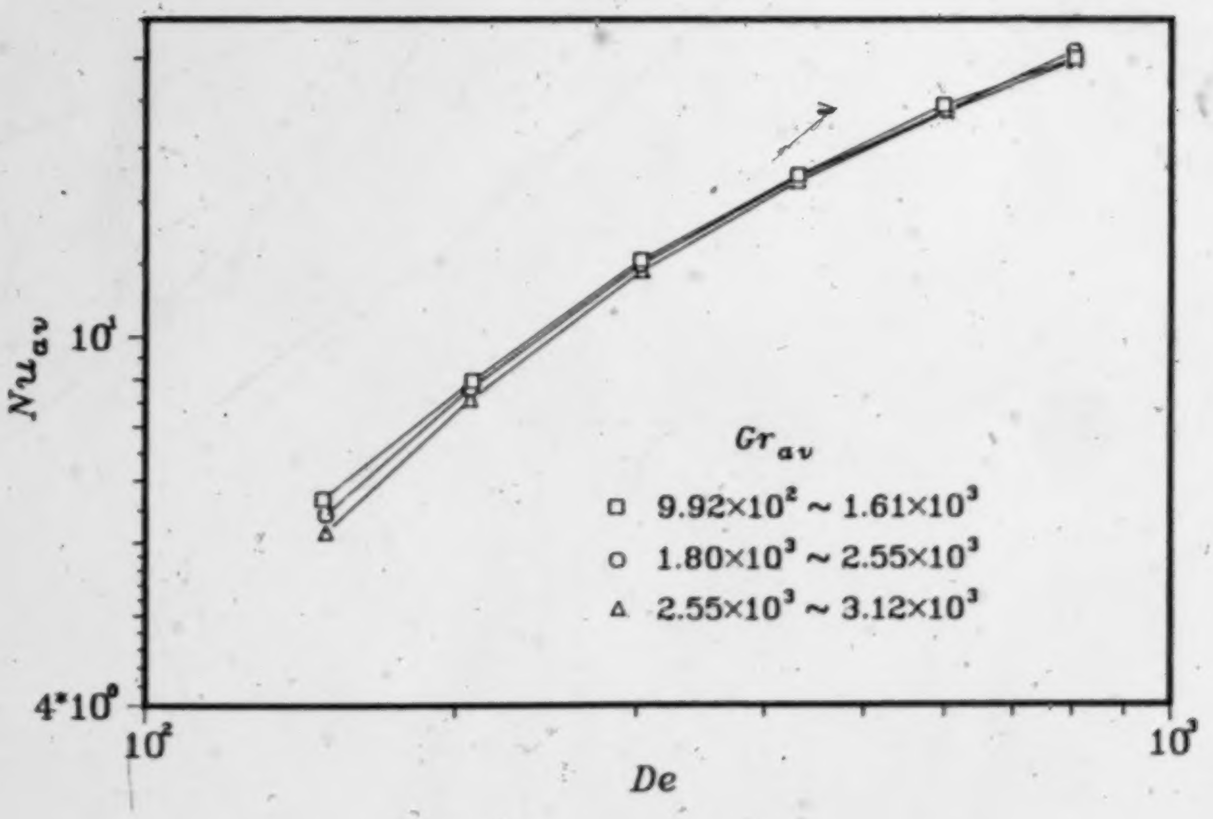

Fig. 2.16 Nu_{av} vs. De for Downward Vertical Curved Pipe Flow with Gr_{av} as Parameter

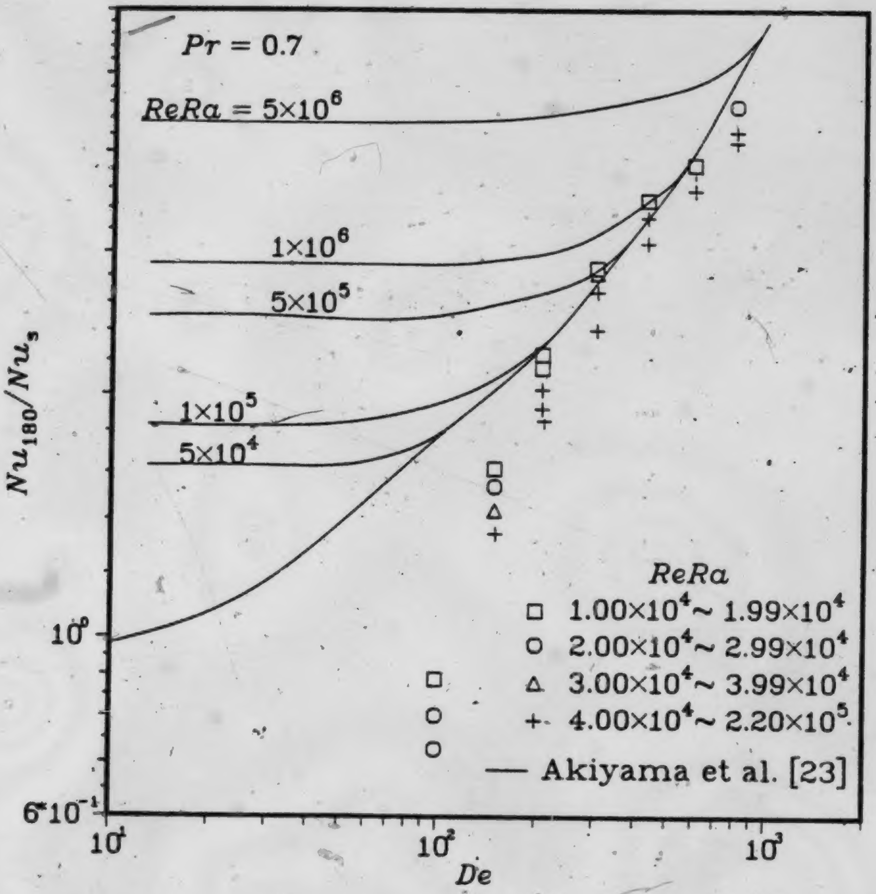

Fig. 2.17 Nu_{180}/Nu_s vs. De for Horizontal Curved Pipe Flow with ReRa as Parameter

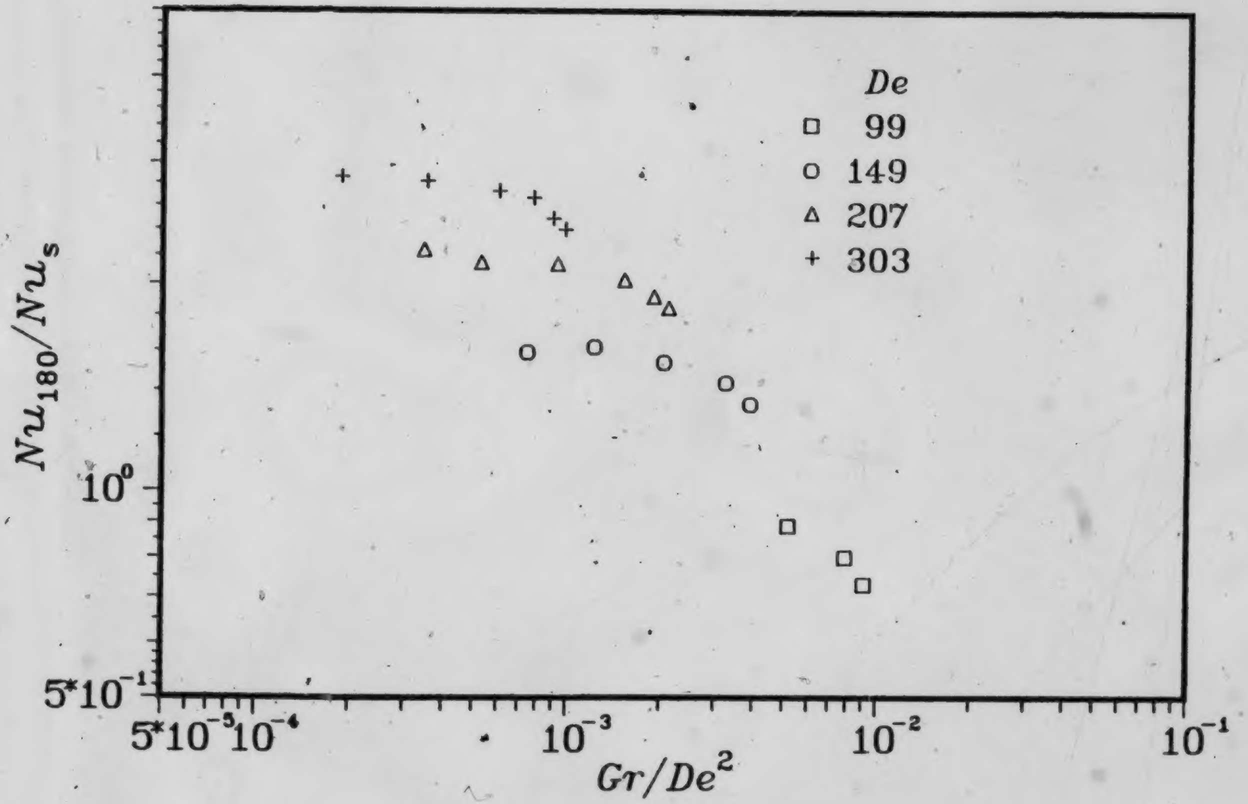

Fig. 2.18 Nu_{180}/Nu_s vs. Gr/De^2 for Horizontal Curved Pipe Flow

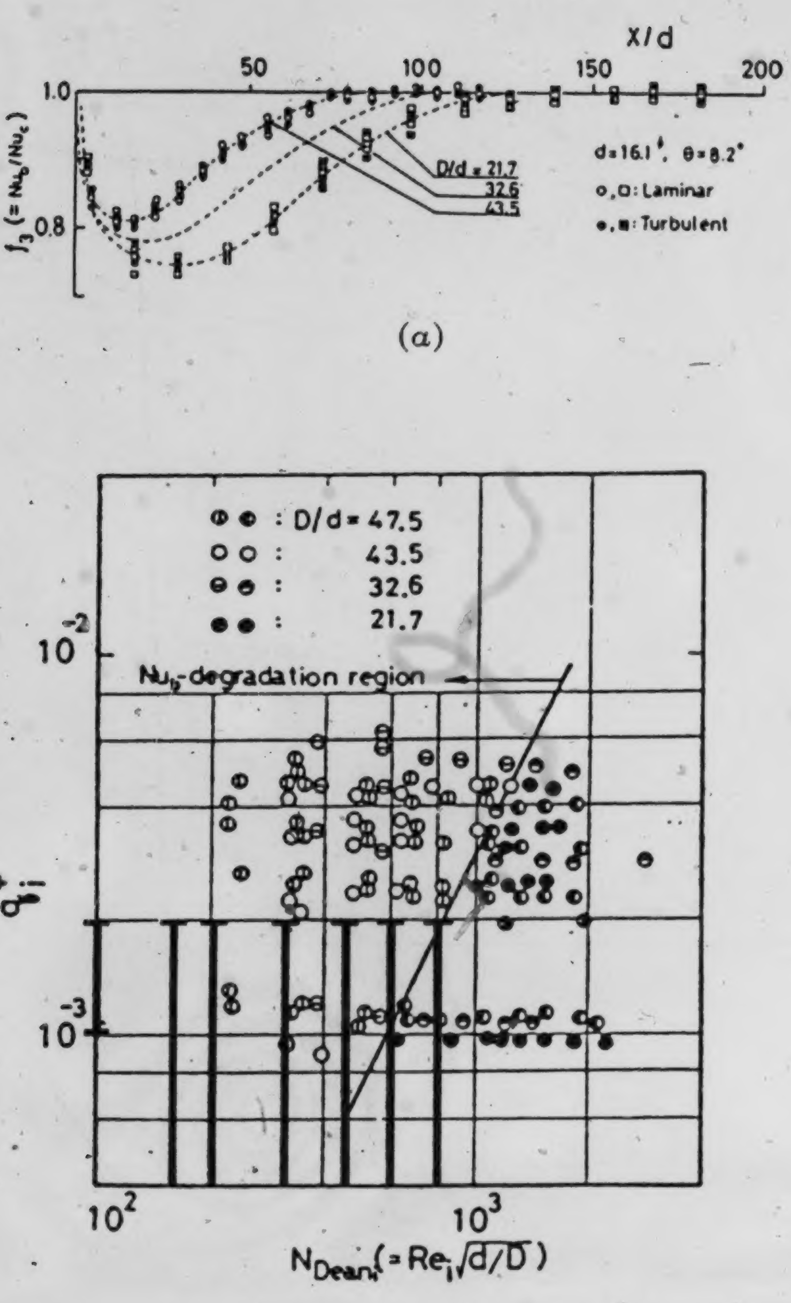

(a)

(b)

Fig. 2.19 (a) Local Nusselt Number Variations and
(b) Heat Transfer Degradation Region

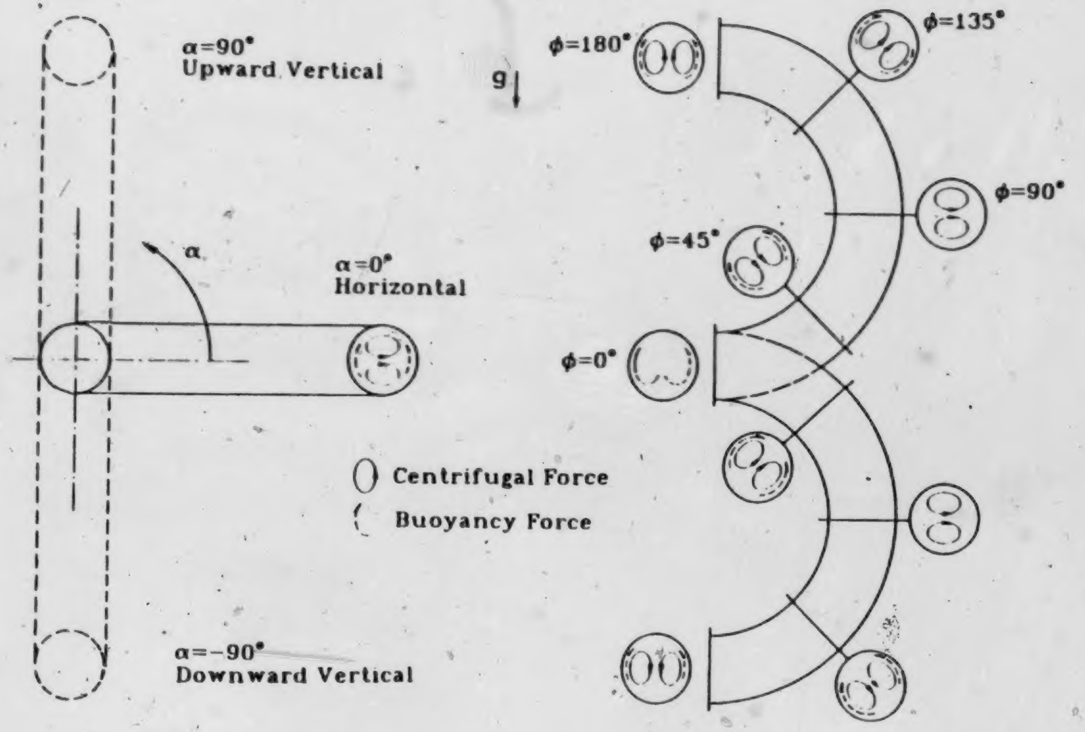
α=90°
Upward Vertical
α
α=0°
Horizontal
α=-90°
Downward Vertical
Centrifugal Force
Buoyancy Force
g
ϕ=180°
ϕ=135°
ϕ=90°
ϕ=45°
ϕ=0°

Fig. 2.20 Schematic Diagrams Illustrating Buoyancy Force Effects with Varying Inclination Angle α

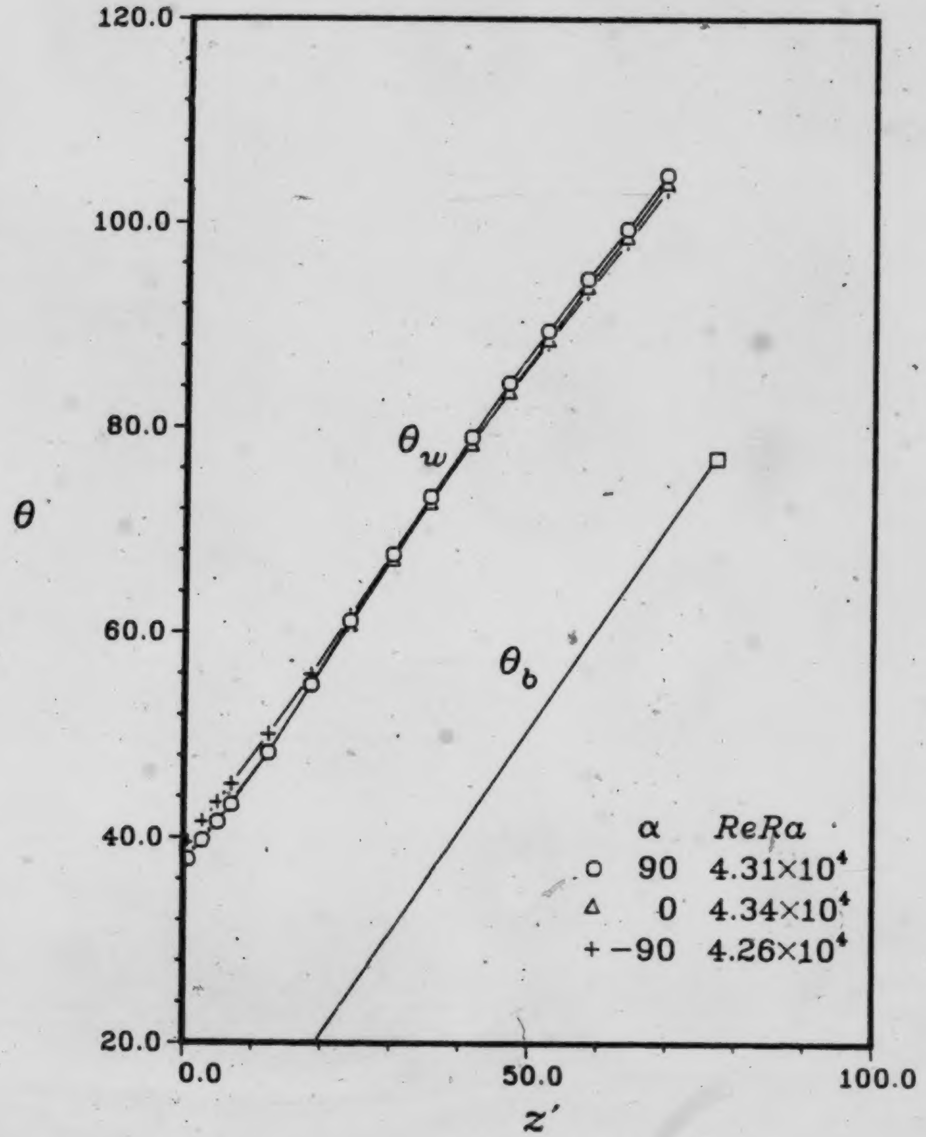

Fig. 2.21 Axial Wall Temperature Distribution for α= 90°, 0° and -90° with ReRa as Parameter

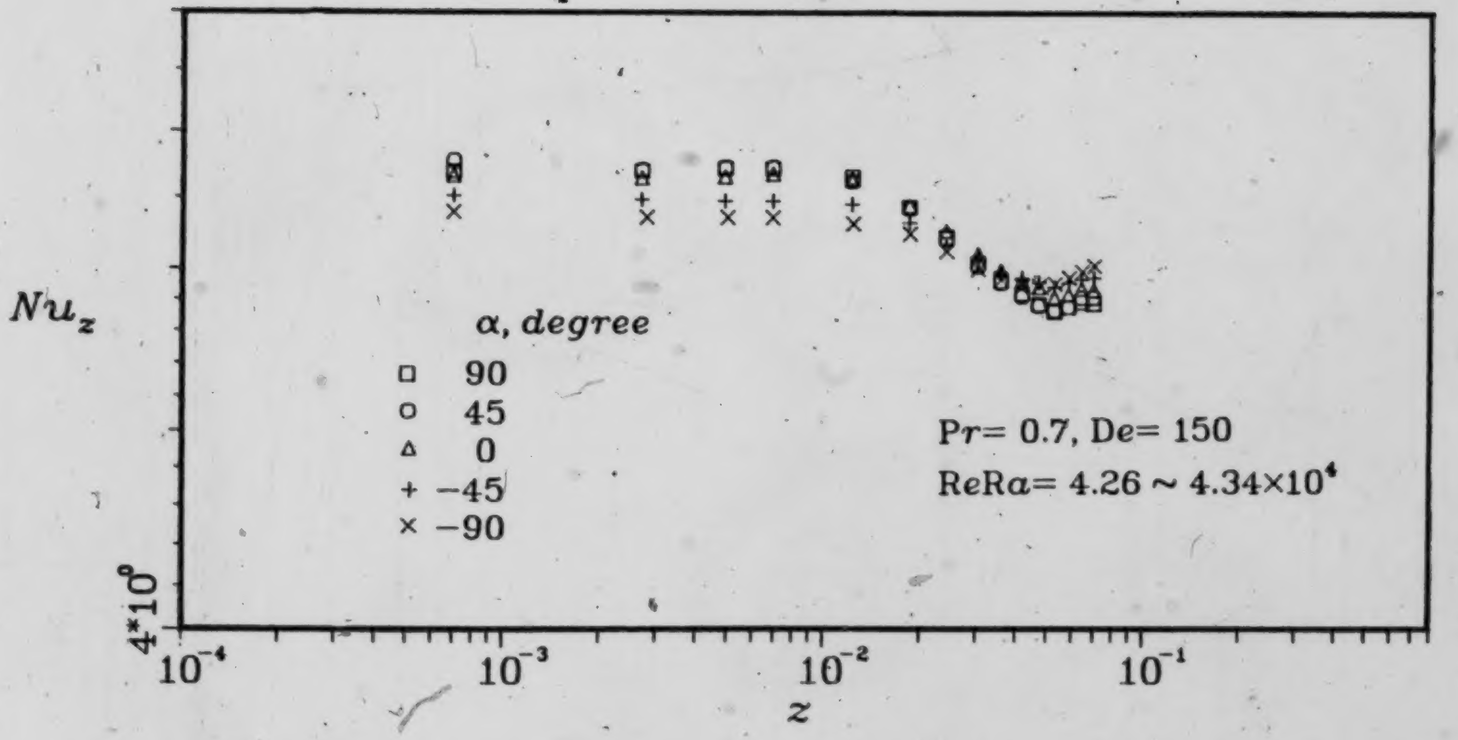

Fig. 2.22 Local Nusselt Number Variation with α and ReRa as Parameter

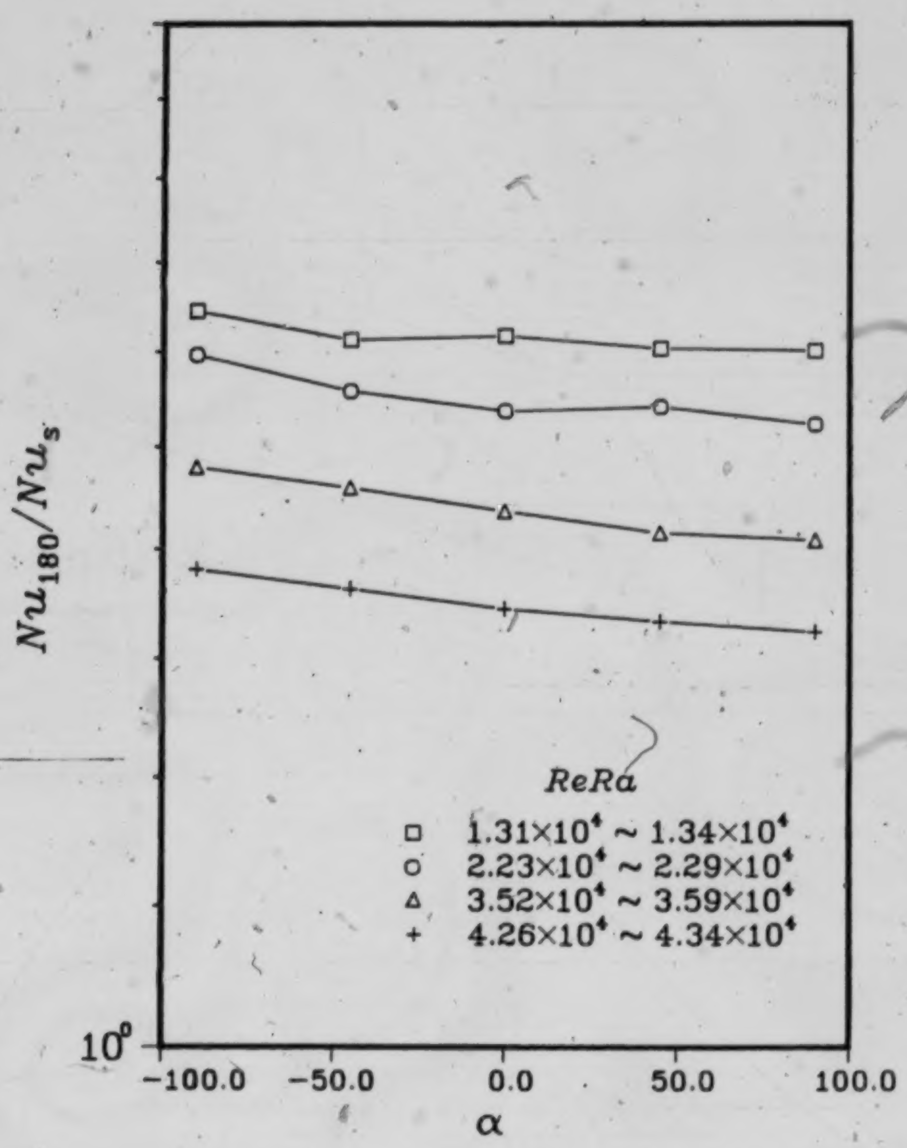

Fig. 2.23 Nu_{180}/Nu_s vs. α for De=150 with ReRa as Parameter

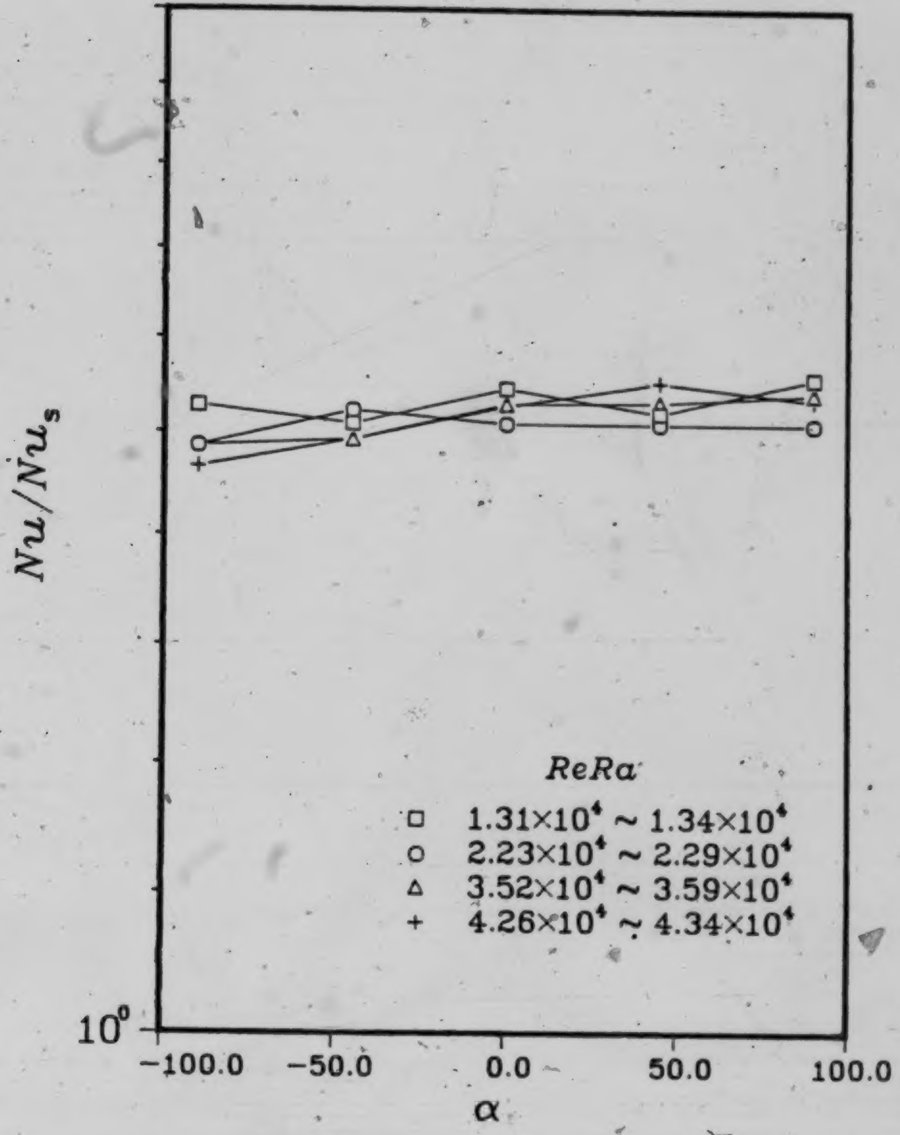

Fig. 2.24 Nu/Nu_s vs. α for De=150, ϕ=0° with ReRa as Parameter

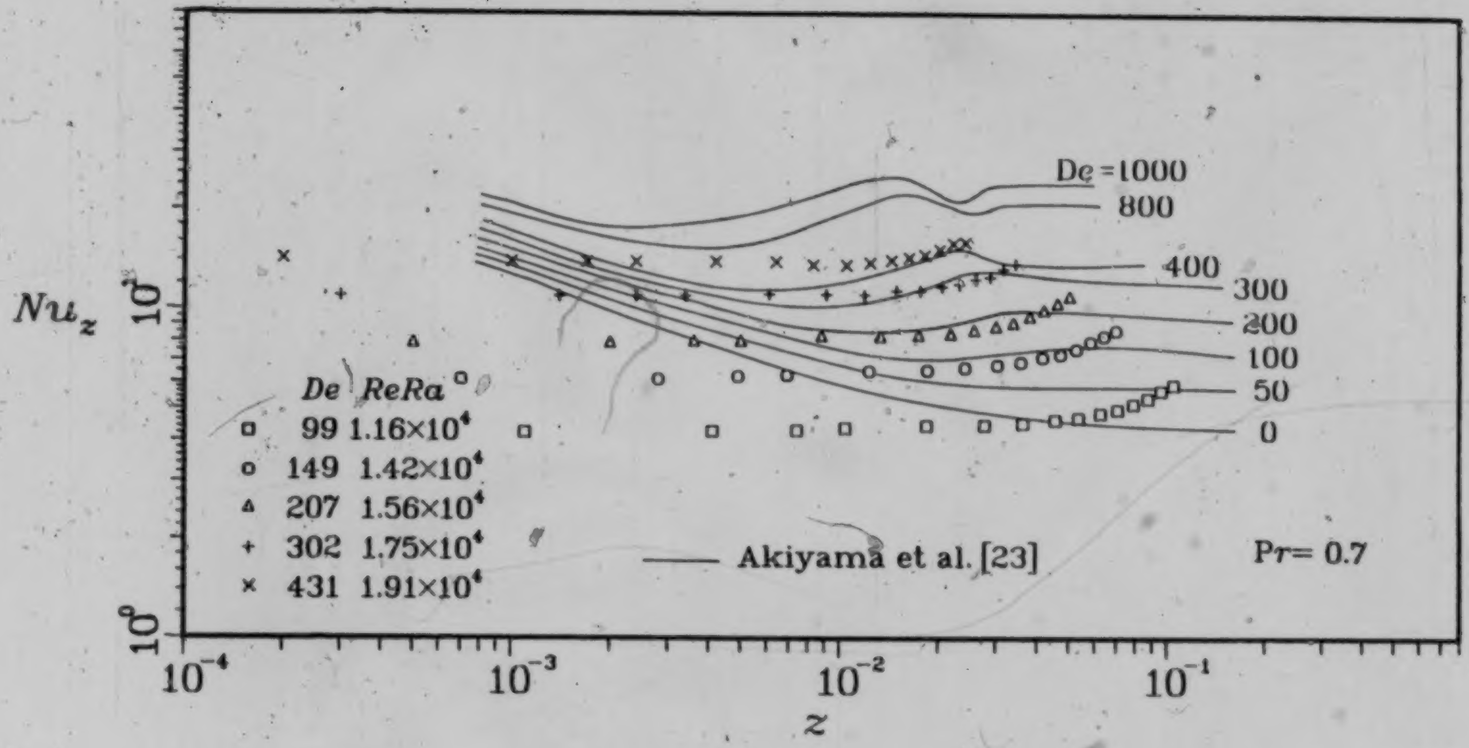

Fig. 2.25 Local Nusselt Number Variation for Horizontal Curved Pipe Flow in Insulation Vessel at 660 mmHg Vacuum

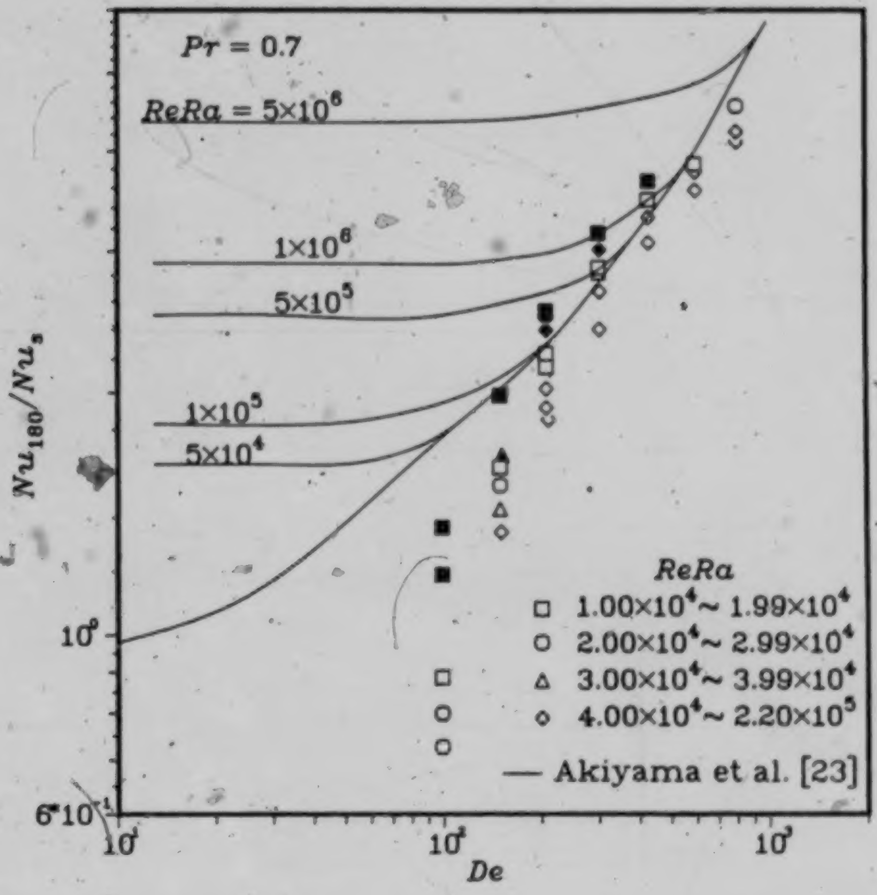

Fig. 2.26 Nu_{180}/Nu_s vs. De for Horizontal Curved Pipe Flow in Insulation Vessel at 660 mmHg Vacuum

3. Flow Visualization Study on Laminar Forced Convection Flow in Curved Pipes

3.1 Introduction

Curved pipes play an important role in many different fields in industry. Particularly the efficient performance of curved pipes in transferring heat is well reflected in their various applications such as coiled heat exchangers and heat engines. Most practical applications are involved with a large heat flux. Therefore the buoyancy effects may be significant in many cases and must be taken into account when establishing the design criteria.

The flow in curved pipes has been an interesting subject to many investigators for almost a century. Due to its practical importance in various fields, numerous theoretical and experimental works have been undertaken to this date. The related literature is so extensive and a detailed coverage will be a futile effort for the present work. Furthermore, most of the background works leading to the present experimental study were already introduced in the preceding chapter. Therefore, the literature survey will be confined to those recent works concerning the buoyancy effects in curved pipe flows.

The importance of buoyancy forces in curved pipe flows has been brought into attention by an analytical treatment on the subject by Yao and Berger [1]. Although their analysis was limited to small values of Dean number and buoyancy parameter, it showed the effect of buoyancy forces can be indeed as significant as that produced by centrifugal forces at low Reynolds numbers. Their work was subsequently followed by an numerical calculation by Prusa and Yao [2]. These initial theoretical considerations clarified that the combined effects of the buoyancy force and the centrifugal force result in a skew pair of vortices as illustrated in Fig. 3.1. The calculated streamline patterns are due to Prusa and Yao [2].

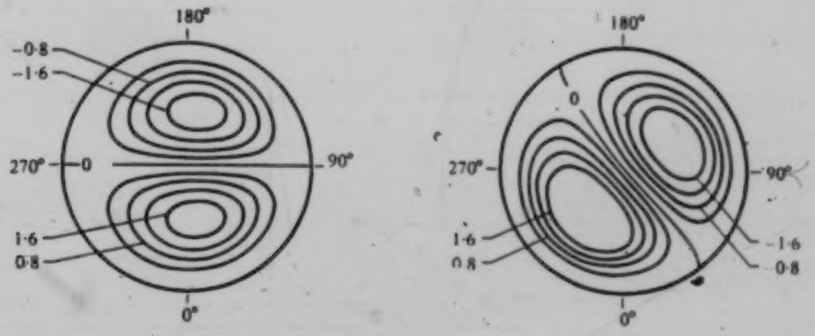

De = 660
ReRa = 0

De = 660
ReRa = 5000

Fig. 3.1 Streamline Patterns of Secondary Flow Motion with and without Buoyancy Effects [2]

Recently, more refined numerical calculations were made by Futagami et al. [3], Akiyama et al. [4], and Lee, Simon and Chow [5]. Their common finding is that the buoyancy forces act to increase the magnitude of secondary flow motions resulting in enhancement in the heat transfer rate for a given mass flow rate. In the preceding chapter, an attempt was made to confirm the results of numerical calculations by conducting a heat transfer experiment. As already discussed, a serious discrepancy was found in the trend of Nusselt numbers obtained by numerical calculations and experiments. Such discrepancy calls for more relible experimental data which may be compared with the calculated results. One of the problems in confirming a numerical result is the lack of experimental data for field information, i.e. velocity and temperature profiles. It is noted that the measurements for such information in a secondary flow field are extremely difficult. For this reason, many investigators resort to a flow visualization study in order to confirm their numerical predictions. A flow visualization study using a hydrogen bubble technique in [4] is a good example.

More recently, a series of flow visualization studies regarding the flow in curved pipes by Cheng and Yuen [6,7] received some attention. In particular the flow visualization results for the case of isothermally heated curved pipe [7] revealed some interesting flow phenomena. There were many other cases where the flow visualization studies motivated and guided theoretical studies in the past. In this connection, it is believed that the present flow visualization study will be valuable in studying the flow phenomena in curved pipes concerning the buoyancy effects and hopefully help substantiate the existing numerical results.

The purpose of the present flow visualization study is to provide some physical understanding of buoyancy force effects in curved pipe flows and to present photographs of secondary flow motions which are comparable to the existing numerical calculations. A series of flow visualization studies were carried out at the exit of a 200° pipe bend which is subject to the uniform heat flux boundary condition with parabolic entrance velocity profile.

Attention is given to the combined effects of the buoyancy force and the centrifugal force with respect to the inclination angle of the curvature plane of bend. Three different cases were considered as the inclination angle α was varied from upward vertical (α=90°), horizontal (α=0°), and to downward vertical (α=-90°) flow cases. An example of comparison between the streamline patterns obtained by a numerical solution and the flow patterns shown by the present study for the case of horizontal flow will be presented. A typical result for the transient case is also presented. The present flow visualization results are also useful in explaining the trends of Nusselt numbers observed in the preceding heat transfer experiments in Chapter 2.

3.2 Experimental Parameters

The experimental parameters in the present flow visualization study are the curvature ratio a/R_c, Reynolds number Re, Dean number De, Rayleigh number Ra, and inclination angle of the plane of curvature from the horizontal direction α. The range of experimental parameters are listed in Table 3.1.

Table 3.1 Range of Experimental Parameters

a/R_c	0.045
Re	260 ~ 3,800
De	55 ~ 800
ReRa	0 ~ 2.20×10^5
α	-90° ~ 90°
Air Flow Rate	62 ~ 916 [cm^3/s]
Mean Velocity	0.2 ~ 2.9 [m/s]

3.3 Experimental Apparatus and Procedure

The test setup used in the present flow visualization study is essentially the same as that used in the preceding heat transfer experiments. The mixing box was removed in order to permit visual observations at the bend exit. The method of flow visualization was a smoke tracer technique. Smoke was created by burning paper sticks in the smoke generator shown in Fig. 2.1 of Chapter 2. The smoke generator was on a by-pass line of the main flow circuit so that it may be easily disconnected from the flow circuit while the flow rate into the test section is kept constant.

No bulk temperature measurements were available with the absence of mixing box. The heat input levels and the range of Dean numbers were basically identical to those used in the preceding heat transfer experiments except for the case of De=55 in the present flow visualization study. Therefore, the ReRa values obtained in the heat transfer experiments were directly used in showing the buoyancy effects in the present flow visualization results. For De=55, the values of ReRa were calculated by using the axial bulk temperature gradients extrapolated against the Dean numbers.

The major steps in the experimental procedure are also similar to those of heat transfer experiments. The flow rate and heat input to the main heater are first set to desired values. The heat input to the compensation heater is controlled as the axial wall temperature distribution is periodically monitored by the data acquisition control system. Due to the presence of an open end and the resulting heat loss, the axial wall temperature was observed to decrease toward the bend exit. The heat input to the compensation heater was varied anywhere between 1.5 W and 8.7 W for each experimental run. After the wall temperature distribution reached a steady-state condition, the smoke generated from burning paper sticks in the smoke generator was fed into the main flow circuit. The density of smoke was adjusted to produce clear secondary flow patterns by controlling the amount of by-pass air through the smoke generator.

The cross-sectional secondary flow patterns were visualized by passing a sheet of light from a 500 W slide projector perpendicular to the direction of main flow at the bend exit. Since the hot air was directly ejected into the atmosphere at an open end, the buoyant air leaving the test section formed into a rising plume creating flow separations near the bottom of the bend exit particularly at low Reynolds numbers. To prevent the plume effect at the pipe exit, a short piece of acrylic resin tube was temporarily attached at the bent exit while photographing the flow patterns. A Nikon single lens reflex camera with a 50mm standard lens was used. Kodak Tri-X black and white film (400 ASA) was used throughout the experiments. The shutter speed was varied from 1/2 to 1/8 of a second at a fixed aperture of f 2.0.

3.4 Results and Discussion

3.4.1 Upward Vertical Flow

The results of flow visualization study for the case of upward vertical flow configuration are shown in Figs. 3.2 to 3.4. Photographs are arranged to show the increasing buoyancy effects on the secondary flow patterns with fixed Dean numbers. The top photograph of each column shows the flow pattern obtained without wall heating for isothermal flow at a given Dean number. It serves as a reference to see the effect of ReRa on the secondary flow pattern with increasing buoyancy parameter. The Rayleigh number is based on the axial bulk temperature gradient. Γ defined as $(Ra/Pr)/De^2$ is also given for reference. This correlation parameter for the buoyancy effects is due to [8]. The dimensionless axial distance z at the bend exit is defined by Eq.(2.11) in Chapter 2. In each photograph, the outer bend is at the top and the inner bend, at the bottom for this flow configuration.

Fig. 3.2 shows the effect of ReRa on the secondary flow patterns at De=55 and 100. For upward vertical flow, the buoyancy forces are in phase with the centrifugal forces in the region $0° < \phi < 90°$. After passing the cross sectional plane at $\phi = 90°$, the two body forces are out of phase in $90° < \phi < 180°$. Therefore the flow pattern observed at the bend exit is the outcome of the rather complicated interaction between two body forces in the simultaneous hydrodynamic and thermal entrance region.

The centrifugal forces caused by the curvature of the bend act to push the fluid in the core region toward the outer bend. Then, by continuity, the fluid near the outer bend returns back to the inner bend along the wall surfaces being driven by the pressure gradient directed toward the inner bend. If the pipe wall is heated, density variations in the fluid occur near the wall surfaces. Since the warm fluid near the wall surface is consequently lighter than the cold fluid in the core region, the resulting buoyancy forces will cause the fluid near the pipe wall to be in upward flow motions. This is where the two body forces interact each other. It should be noted that such opposing interaction between the buoyancy force and the centrifugal force was predicted by Yao and Berger [1]. As the buoyancy forces increase, the secondary flow field due to centrifugal forces alone will be further distorted. This point is well illustrated by the photographs shown in column-(a). One prominent trend is that the eyes of vortices are gradually moved to the outer bend with increasing value of ReRa.

In Fig. 3.3, the effect of ReRa on secondary flow pattern is shown for Dean numbers 150 and 200. By comparing Fig. 3.2 and 3.3, one finds that the buoyancy effects observed as the lift-up of the cores of vortex pair are not as prominent although the buoyancy parameters are still quite high. This is apparently due to the increased momentum of the main flow which consequently surpasses the effect of buoyancy forces. Apart from the trend of lift-up of the vortex cores, the increasing black region near the inner bend and the open-up of the demarcation line of vortices are other trends observed with increasing buoyancy effects.

Fig. 3.4 shows the secondary flow patterns at Dean numbers 300, 430, 600, and 800. In view of the decaying buoyancy effects with increasing Dean number, only a typical case with a fairly large ReRa is shown for comparison at each Dean number.

For De=300, the eyes of vortex pair are still observed to be slightly lifted up as a result of buoyancy effects. At De=430 and ReRa=0, an additional pair of vortices (presumably Dean vortices) begin to appear near the outer bend and the streamline patterns tend to become distorted. On the other hand, in the picture obtained at De=430 and ReRa=1.22×10^5, the additional pair of vortices seems to disappear and the flow field becomes far more stable than that of the unheated case. At De=600, a similar flow situation exists, but highly distorted streamline patterns can be observed. It is noted that the Reynolds number for this case is 2,860, exceeding the critical Reynolds number 2,300 in a straight pipe. The present flow visualization study clearly shows the stabilizing effect of curved flow passage which gives rise to a relaminarization phenomenon. The photograph for unheated case at De=800 shows the complex nature of flow patterns at high Dean numbers, but a pair of vortices is still barely identified. Although not shown here, the flow was intermittently turbulent. A comparison of the photographs at De=800 with and without heating suggests the stabilizing effect of wall heating. It should be mentioned that the intermittently observed transition didn't occur as the wall heating condition was imposed. It is interesting to notice that the appearance of black region near the inner bend and the trend of open-up of the demarcation line are still clearly observed at high Dean numbers.

3.4.2 Horizontal Flow

The same arrangements of photographs as those of the previous section are given in Figures 3.5 through 3.7. In this case, the inner bend of the curved pipe is shown on the left hand side of each photograph and the outer bend, on the right hand side. The centrifugal forces created by the curvature of the bend act from the left to the right forming a pair of vortices with symmetry in the central horizontal plane. The buoyancy forces caused by wall heating act in the vertical direction. The results of numerical calculations show that the combined effects of these two perpendicular forces result in a pair of vortices skewed from the horizontal direction. Such prediction is clearly confirmed by the present flow visualization study.

The secondary flow patterns obtained for De=55 and 100 at different buoyancy parameters are shown in Fig. 3.5. An inspection of the flow patterns shows the increasing degree of skewness with increasing buoyancy parameter. It is also noted that the resulting pair of vortices is not neccessarily symmetric as indicated by a curved demarcation line and the increased area for bottom vortex. In Fig. 3.6, similar arrangements of secondary flow patterns for De=150 and 200 are given. One may notice that both the skewness and nonsymmetricity of vortex pair is seen to be substantially weakened in comparison with those of the previous cases at lower Dean numbers.

Fig. 3.7 shows the results of flow visualization study for higher Dean numbers. At De=300, the skewness almost disappears, but again the black region near the inner bend and the larger demarcation region near the center are clearly observed. In general, similar effects of wall heating are observed for De=430 and also some stabilizing effects caused by wall heating may be mentioned. At De=600, there's no significant difference in the flow patterns obtained with and without wall heating. For De=800, a similar intermittent transition to turbulence to the case of upward vertical flow was again observed.

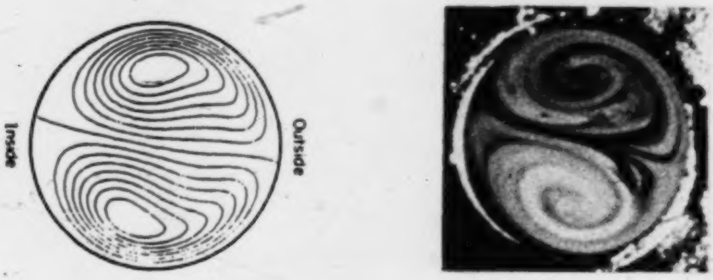

Re= 749.71
De= 149.94
ReRa = 40,000
Pr= 1.0

Re= 702
De= 149
ReRa = 43,400
Pr= 0.71

Fig. 3.8 Comparison between the Streamline Patterns Obtained by Numerical Calculation [5] and Present Flow Visualization Result for Horizontal Flow Case

A typical streamline pattern obtained from a numerical solution [5] is compared with the flow pattern obtained by the present study in Fig. 3.8.

3.4.3 Downward Vertical Flow

In this flow configuration, the effect of buoyancy forces is directly opposite to that of upward vertical flow. Up to the angular position 90° from the start of bend, the buoyancy forces are out of phase acting against the centrifugal forces. Passing 90°, the two forces act in phase.

In Fig. 3.9, the secondary flow patterns obtained for De=55 and 100 are shown in the order of increasing buoyancy parameter. Photographs in column (a) clearly show the dominating effets of buoyancy forces as the secondary flow patterns are observed to significantly differ from those of unheated case. In particular the secondary flow patterns obtained at ReRa= 1.54×10^4 and 1.69×10^4 are very close to those obtained for isothermally heated straight pipe in [6]. The black crescent observed at ReRa= 1.69×10^4 is noteworthy in distinction from the preceding flow patterns. This is apparently a consequence of wall heating.

Photographs for De=100 do not show any significant change in the secondary flow patterns. However, in view of the significant buoyancy force effects at low Dean numbers demonstrated by the previous sections, it is believed that the intensity of the secondary flow motion is substantially assisted by the buoyancy forces.

Fig. 3.10 shows the secondary flow patterns for Dean numbers 150 and 200. In general one finds that there is no significant buoyancy force effect observed on the secondary flow pattern for both cases. However as already pointed out in the previous sections, the trends of increasing black region near the inner bend and the enlarged demarcation zone in the center are clearly seen as the consequence of increasing wall heating.

Photographs of secondary flow pattern for De=300, 430, 600, and 800 without heating are shown with those with fairly large buoyancy parameter in Fig. 3.11. The trend observed is quite similar to that noted in the previous sections. One cannot detect any buoyancy force effect from the comparison of the photographs obtained with and without wall heating. The stabilizing effect of wall heating is again observed for De=430, 600, and 800.

3.4.4 Transient Secondary Flow Field at De=55 for Horizontal Flow

Fig. 3.12 shows the developing transient secondary flow patterns for De=55. The heat input used for this case was 30 W. At steady-state condition, such heat input yields a value of ReRa= 1.70×10^4. Photographs were arranged in the order of increasing time from the start of heating to show the transient effect. The Fourier modulus

Fo is defined as

$$Fo = \kappa t/a^2 \qquad (3.1)$$

where κ is the thermal diffusivity of air.

The effect of wall heating begins to appear at t=60 sec as the fluid near the inner bend is gradually being lifted up by the effect of buoyancy forces. The skewness of vortices also begins to appear in the clockwise direction. The direction of skewness is obviously due to the low velocity region near the inner bend which is easily affected by the buoyancy forces. The change of skewness is observed to stop at t=180 sec and no further significant change can be detected.

3.5 Concluding Remarks

A series of flow visualization studies were carried out at the exit of 200° bend to illustrate the combined effect of centrifugal forces and buoyancy forces in curved pipe flows using a smoke tracer technique.

The test pipe was subjected to the uniform wall heat flux boundary condition with a parabolic entrance velocity profile. The cross-sectional views of the resulting secondary flow patterns were obtained for the following three cases with respect to the three different inclination angles of the curvature plane: upward vertical (α=90°), horizontal (α=0°), and downward vertical (α=-90°) flows. The flow patterns for upward vertical and downward vertical cases, respectively, show the opposing and assisting effects of the centrifugal force and the buoyancy force at the bend exit. Such observations are in good agreement with the trends of Nusselt numbers observed in the preceding heat transfer experiments.

The present flow visualization results for the case of horizontal flow show the trend of increasing degree of skewness of vortices with increasing buoyancy effects and qualitatively confirm the secondary flow patterns from published numerical solutions. A typical comparison between calculated streamlines and a present flow visualization result reveals a good agreement in the shape of skewed streamline patterns. Comparing with the flow visualization results shown in [7], the flow in the present experiments under the uniform wall heat flux boundary condition appears to be less susceptible to the occurrence of Dean vortices. The stabilizing effect of wall heating was also revealed.

The present flow visualization study provides physical insights into the transport phenomena in a heated curved pipe under the uniform wall heat flux boundary condition. It is believed that the present photographic results will be useful to future investigations in the related area.

3.6 References

1. Yao, Lun-Shin and Berger, Stanley A., "Flow in Heated Curved Pipes," J. Fluid Mech. Vol. 88, Part 2, 1978, pp. 339 - 354.

2. Prusa, J. and Yao, L.S., "Numerical Solution For Fully Developed Flow in Heated Curved Tubes," J. Fluid Mech. Vol. 123, 1982, pp. 503 - 522.

3. Futagami, K., Aoyama, Y. and Abe, F., "Forced and Free Combined Convective Laminar Heat Transfer in a Helically-Coiled Tube," Trans. Jap. Soc. ~~of~~ Mech. Engrs, Vol. 47B, 1981, pp. 1995 - 2003.

4. Akiyama, M., Suzuki, M., Cheng, K.C., Suzuki, Mi. and Nishiwaki, I., "Mixed Convection in the Laminar Entry Flow of Curved Circular Pipes," Int. Symposium on Heat Transfer, Tsinghua University, Beijing, P.R.C., 1983.

5. Lee, Jy-ber, Simon, H.A. and Chow, J.C.F., "Buoyancy in Developed Laminar Curved Tube Flows," Int. J. Heat Mass Transfer, Vol. 28, No. 3, 1985, pp. 631 - 640.

6. Cheng, K.C. and Yuen, F.P., "Flow Visualization Studies on Secondary Flow Patterns in Curved Tubes and Isothermally Heated Horizontal Tubes," ASME Paper 84-HT-62, 22nd ASME/AICHE National Heat Transfer Conf., Niagara Falls, New York, Aug. 5 - 8, 1984.

7. Cheng, K.C. and Yuen, F.P., "Flow Visualization Experiments of Secondary Flow Patterns in an Isothermally Heated Curved Pipe," Eds. B.F. Armaly and L.S. Yao, Mixed Convection Heat Transfer, HTD-Vol. 53, ASME, 1985, pp. 17-24

8. Akiyama, M., Kikuchi, K., Cheng, K.C., Suzuki, Mi. and Nishiwaki, I., "Mixed Laminar Convection of the Thermal Entry Region in Curved Rectangular Channels," ASME-JSME Thermal Engineering Joint Conference, Vol. 3, 1983, pp. 27 - 33.

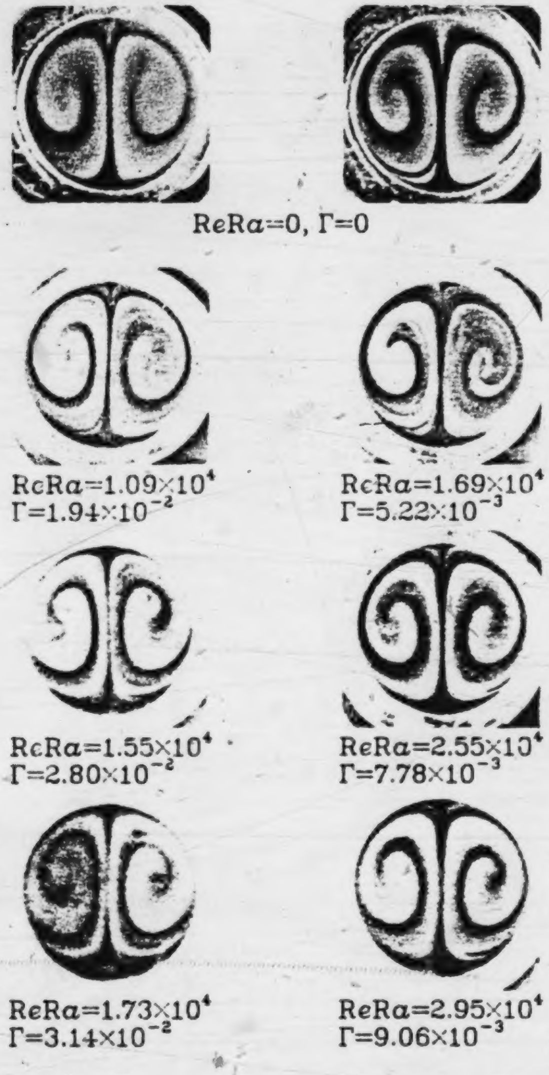

$ReRa=0$, $\Gamma=0$

$ReRa=1.09\times10^4$
$\Gamma=1.94\times10^{-2}$

$ReRa=1.69\times10^4$
$\Gamma=5.22\times10^{-3}$

$ReRa=1.55\times10^4$
$\Gamma=2.80\times10^{-2}$

$ReRa=2.55\times10^4$
$\Gamma=7.78\times10^{-3}$

$ReRa=1.73\times10^4$
$\Gamma=3.14\times10^{-2}$

$ReRa=2.95\times10^4$
$\Gamma=9.06\times10^{-3}$

(a) $De=55$
$z=0.211$

(b) $De=100$
$z=0.116$

Fig. 3.2 Secondary Flow Patterns for Upward Vertical Flow at De=55 and 100 with ReRa and Γ as Parameters

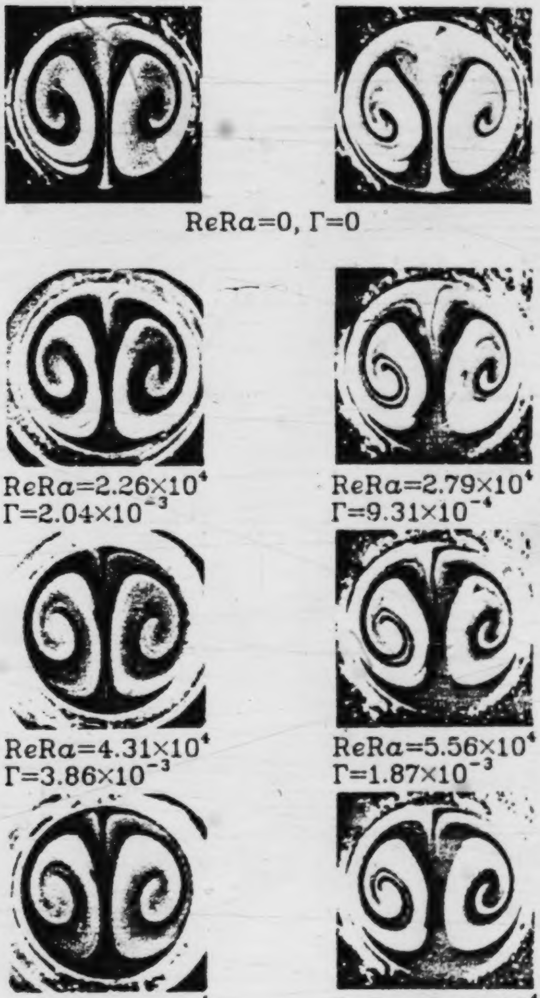

ReRa=0, Γ=0

$ReRa=2.26\times10^{4}$
$\Gamma=2.04\times10^{-3}$

$ReRa=2.79\times10^{4}$
$\Gamma=9.31\times10^{-4}$

$ReRa=4.31\times10^{4}$
$\Gamma=3.86\times10^{-3}$

$ReRa=5.56\times10^{4}$
$\Gamma=1.87\times10^{-3}$

$ReRa=4.77\times10^{4}$
$\Gamma=4.25\times10^{-3}$

$ReRa=6.48\times10^{4}$
$\Gamma=2.11\times10^{-3}$

(a) De=150
$z=0.077$

(b) De=200
$z=0.056$

Fig. 3.3 Secondary Flow Patterns for Upward Vertical Flow at De=150 and 200 with ReRa and Γ as Parameters

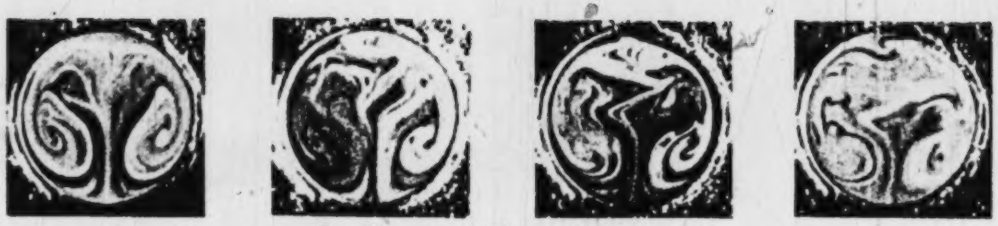

Isothermal Flow, ReRa=0

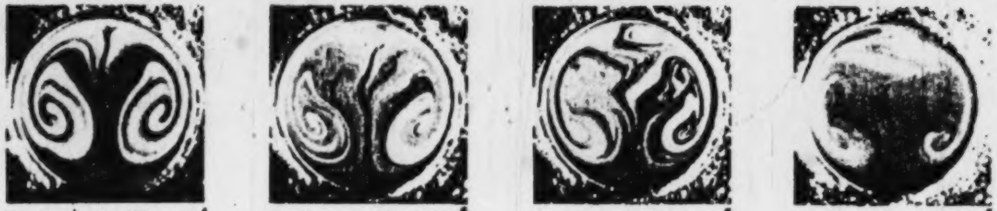

$ReRa=9.08\times10^{4}$
$\Gamma=9.77\times10^{-4}$

$ReRa=1.22\times10^{5}$
$\Gamma=4.49\times10^{-4}$

$ReRa=1.62\times10^{5}$
$\Gamma=2.27\times10^{-4}$

$ReRa=2.16\times10^{5}$
$\Gamma=1.25\times10^{-4}$

(a) De=300
$z=0.038$

(b) De=430
$z=0.027$

(c) De=600
$z=0.019$

(d) De=800
$z=0.014$

Fig. 3.4 Secondary Flow Patterns for Upward Vertical Flow at De=300, 430, 600 and 800 with ReRa and Γ as Parameters

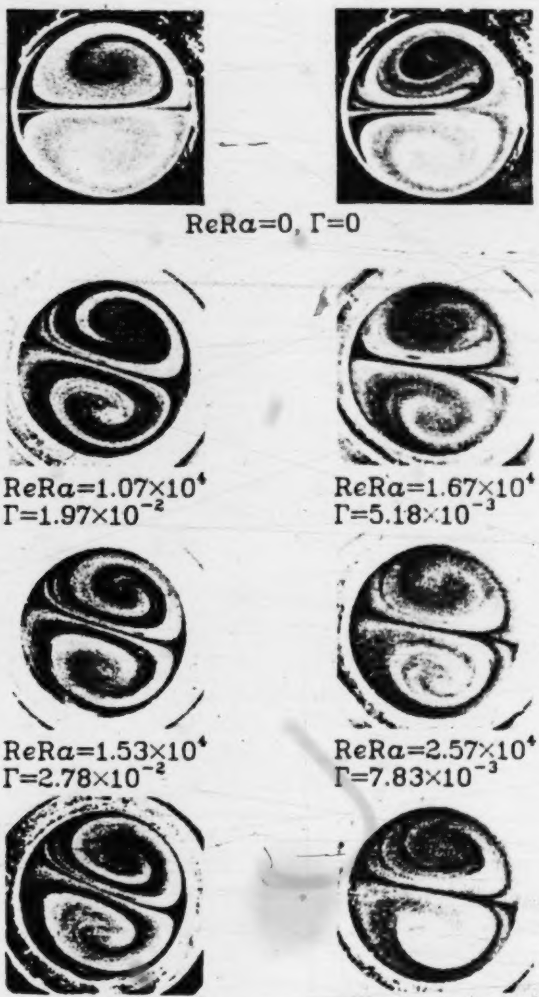

ReRa=0, Γ=0

ReRa=1.07×10^{4}
Γ=1.97×10^{-2}

ReRa=1.67×10^{4}
Γ=5.18×10^{-3}

ReRa=1.53×10^{4}
Γ=2.78×10^{-2}

ReRa=2.57×10^{4}
Γ=7.83×10^{-3}

ReRa=1.70×10^{4}
Γ=3.16×10^{-2}

ReRa=2.94×10^{4}
Γ=9.08×10^{-3}

(a) De=55
z=0.211

(b) De=100
z=0.116

Fig. 3.5 Secondary Flow Patterns for Horizontal Flow at De=55 and 100 with ReRa and Γ as Parameters

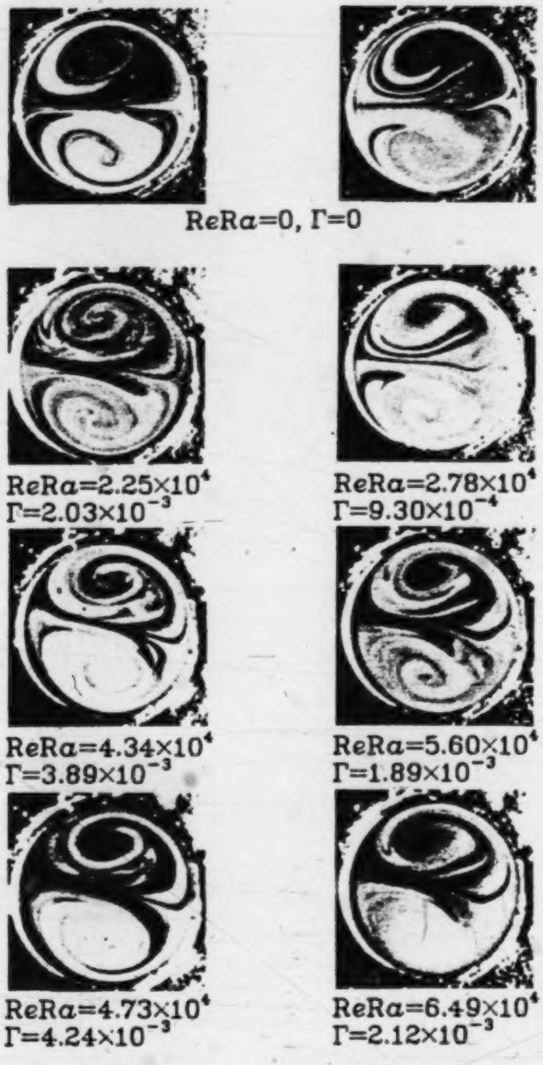

$ReRa=0$, $\Gamma=0$

$ReRa=2.25\times10^4$
$\Gamma=2.03\times10^{-3}$

$ReRa=2.78\times10^4$
$\Gamma=9.30\times10^{-4}$

$ReRa=4.34\times10^4$
$\Gamma=3.89\times10^{-3}$

$ReRa=5.60\times10^4$
$\Gamma=1.89\times10^{-3}$

$ReRa=4.73\times10^4$
$\Gamma=4.24\times10^{-3}$

$ReRa=6.49\times10^4$
$\Gamma=2.12\times10^{-3}$

(a) $De=150$
$z=0.077$

(b) $De=200$
$z=0.056$

Fig. 3.6 Secondary Flow Patterns for Horizontal Flow at De=150 and 200 with ReRa and Γ as Parameters

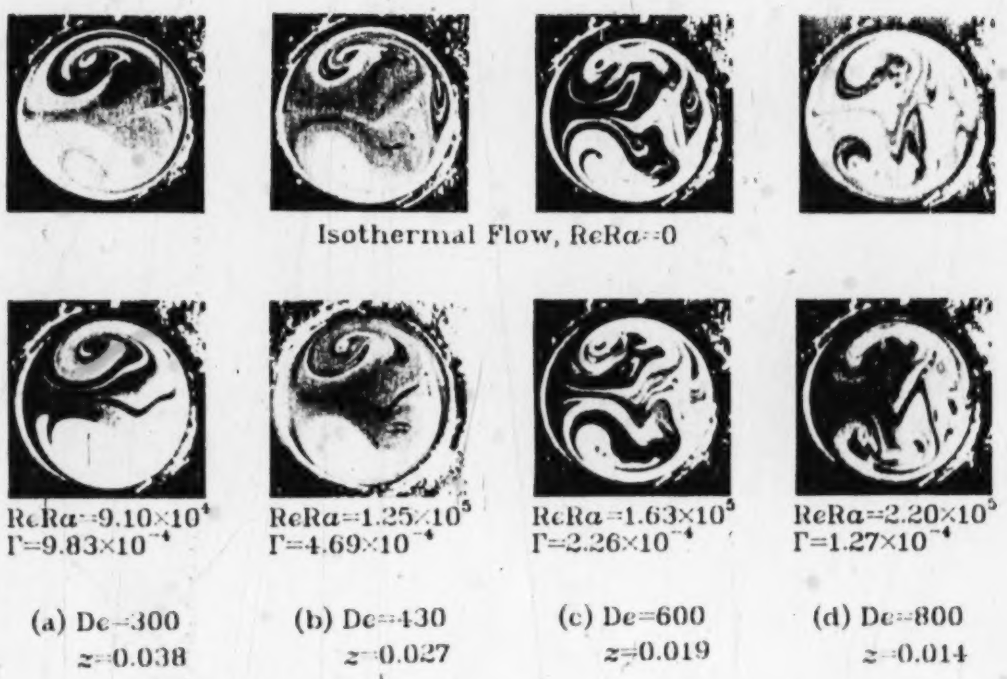
Isothermal Flow, $ReRa=0$
$ReRa=9.10\times10^4$
$\Gamma=9.83\times10^{-4}$
$ReRa=1.25\times10^5$
$\Gamma=4.69\times10^{-4}$
$ReRa=1.63\times10^5$
$\Gamma=2.26\times10^{-4}$
$ReRa=2.20\times10^5$
$\Gamma=1.27\times10^{-4}$
(a) $De=300$
$z=0.038$
(b) $De=430$
$z=0.027$
(c) $De=600$
$z=0.019$
(d) $De=800$
$z=0.014$

Fig. 3.7 Secondary Flow Patterns for Horizontal Flow at De=300, 430, 600 and 800 with ReRa and Γ as Parameters

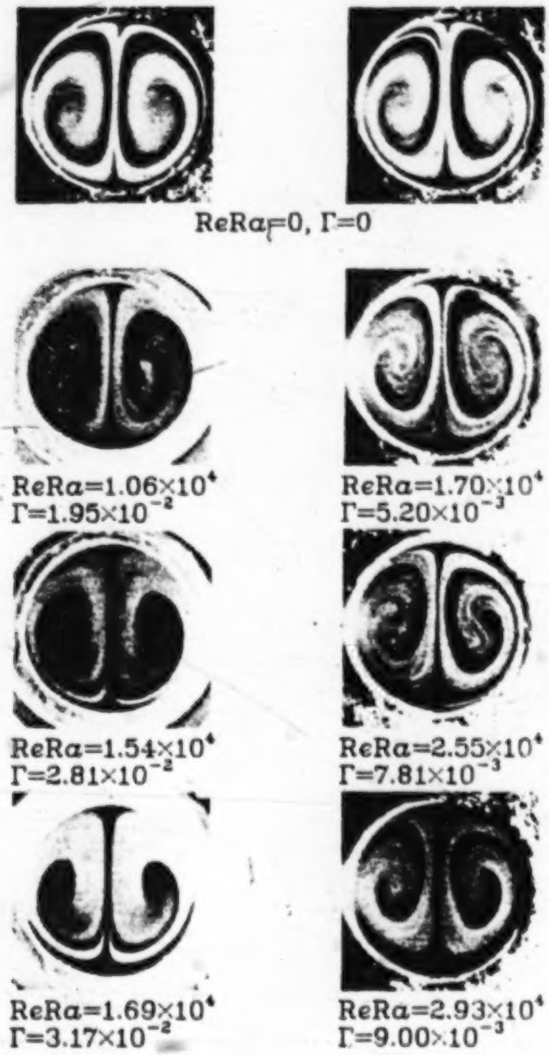

$ReRa=0,\ \Gamma=0$

$ReRa=1.06\times10^{4}$
$\Gamma=1.95\times10^{-2}$

$ReRa=1.70\times10^{4}$
$\Gamma=5.20\times10^{-3}$

$ReRa=1.54\times10^{4}$
$\Gamma=2.81\times10^{-2}$

$ReRa=2.55\times10^{4}$
$\Gamma=7.81\times10^{-3}$

$ReRa=1.69\times10^{4}$
$\Gamma=3.17\times10^{-2}$

$ReRa=2.93\times10^{4}$
$\Gamma=9.00\times10^{-3}$

(a) $De=55$
$z=0.211$

(b) $De=100$
$z=0.116$

Fig. 3.9 Secondary Flow Patterns for Downward Vertical Flow at De=55 and 100 with ReRa and Γ as Parameters

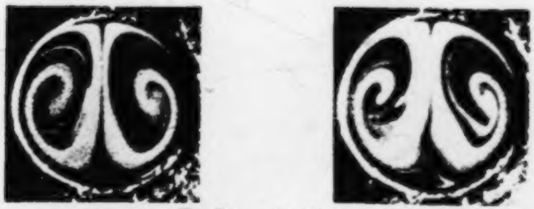

$ReRa=0$, $\Gamma=0$

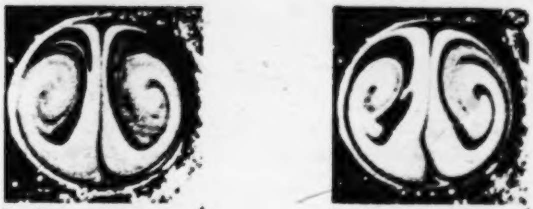

$ReRa=2.23\times10^{4}$
$\Gamma=2.01\times10^{-3}$

$ReRa=2.70\times10^{4}$
$\Gamma=9.15\times10^{-4}$

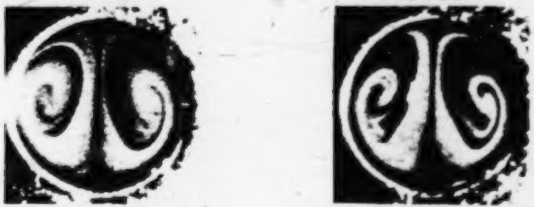

$ReRa=4.26\times10^{4}$
$\Gamma=3.86\times10^{-3}$

$ReRa=5.48\times10^{4}$
$\Gamma=1.86\times10^{-3}$

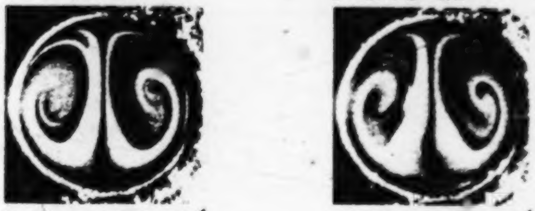

$ReRa=4.73\times10^{4}$
$\Gamma=4.29\times10^{-3}$

$ReRa=6.18\times10^{4}$
$\Gamma=2.10\times10^{-3}$

(a) $De=150$
$z=0.077$

(b) $De=200$
$z=0.056$

Fig. 3.10 Secondary Flow Patterns for Downward Vertical Flow at De=150 and 200 with ReRa and Γ as Parameters

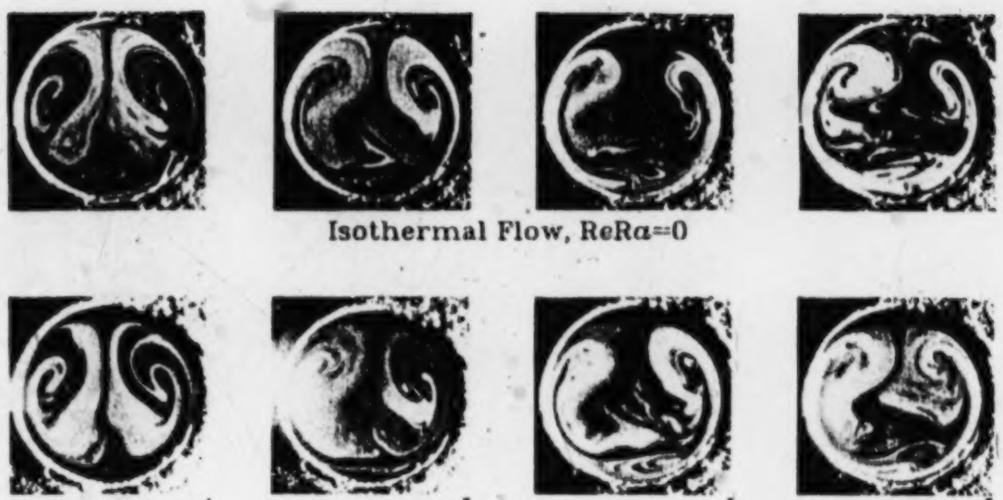

Isothermal Flow, $ReRa=0$

$ReRa=9.03\times10^{4}$
$\Gamma=9.77\times10^{-4}$

$ReRa=1.25\times10^{5}$
$\Gamma=4.68\times10^{-4}$

$ReRa=1.64\times10^{5}$
$\Gamma=2.27\times10^{-4}$

$ReRa=2.17\times10^{5}$
$\Gamma=1.25\times10^{-4}$

(a) $De=300$
$z=0.038$

(b) $De=430$
$z=0.027$

(c) $De=600$
$z=0.019$

(d) $De=800$
$z=0.014$

Fig. 3.11 Secondary Flow Patterns for Downward Vertical Flow at De=300, 430, 600 and 800 with ReRa and Γ as Parameters

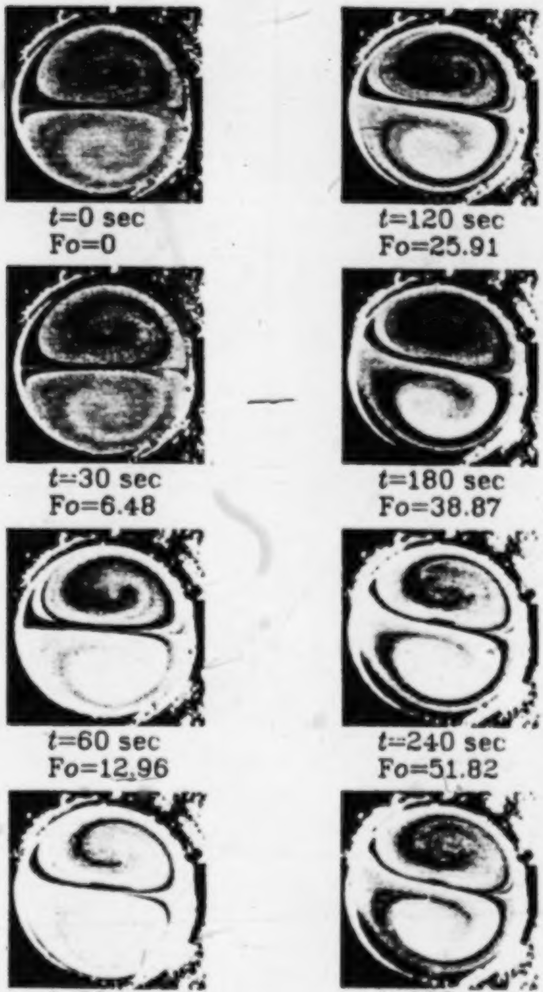

t=0 sec
Fo=0

t=30 sec
Fo=6.48

t=60 sec
Fo=12.96

t=90 sec
Fo=19.43

t=120 sec
Fo=25.91

t=180 sec
Fo=38.87

t=240 sec
Fo=51.82

t=300 sec
Fo=64.78

Fig. 3.12 Transient Case for Horizontal Flow at De=55 with t and Fo as Parameters

4. Flow Visualization Studies on Vortex Instability of Natural Convection Flow over Horizontal and Slightly Inclined Constant Temperature Plates*

4.1 Introduction

The problem of natural convection flows along inclined plates with vertical and horizontal directions as limiting cases under the thermal boundary condition of constant wall temperature or uniform wall heat flux has been studied both theoretically and experimentally by many investigators in the past because of its importance in various technical applications. When a natural convection flow is induced by heating from below over a horizontal or slightly inclined plate with constant wall temperature, for example, the flow is potentially unstable because of top heavy situation. The convective instability problem occurs if the destabilization caused by buoyancy is large enough to overcome the stabilizing effects of viscous and thermal diffusion.

The occurrence of longitudinal vortices or rolls in natural convection boundary-layer flows along inclined isothermal surfaces was clearly established by Sparrow and Husar [1] using a flow visualization technique revealing the flow pattern made visible by local changes of colour of the fluid due to a change in pH. Subsequently, the instability data of natural convection flow on inclined isothermal plates were also obtained by Lloyd and Sparrow [2] and Lloyd [3]. Apparently, these experimental investigations have motivated a series of linear stability studies on the onset of longitudinal vortices in natural convection flow along inclined surfaces. In this connection, one may mention the linear stability analyses by Haaland and Sparrow [4], Hwang and Cheng [5] and Kahawita and Meroney [6]. The wave instability analysis results were also presented by Lee and Lock [7], Haaland and Sparrow [8] and Pera and Gebhart [9]. Iyer and Kelly [10] studied both wave and vortex modes of instability for a heated inclined plate. Recently both vortex and wave instability analysis results were presented by Chen and co-workers [11,12] for natural convection flow on inclined isothermal surfaces. It is of interest to note that Hsu and Cheng [13] carried out vortex instability analysis for buoyancy-induced flow over inclined heated surfaces in porous media.

---

* A version of this chapter has been accepted for publication. Cheng, K.C. and Kim, Yong W., 1986 ASME Winter Annual Meeting, Anaheim, CA, Nov. 30, 1986.

It is now well established that in the range of inclination angles from the horizontal direction $\theta = 0 - 73°$ the vortex instability has priority over the wave instability and the opposite is true near the vertical plate. It is noted that the experimental instability data for the onset of longitudinal vortices are rather limited for the range of inclination angles $\theta = 0$ to $25°$.

The purpose of this chapter is to present flow visualization photographs for the onset and subsequent development of longitudinal vortex rolls for natural convection flow along inclined constant temperature plates at inclination angles θ = 0, 5, 10, 15 and 20°. The flow visualization was realized by a smoke injection method. The experiments were conducted in a suction low speed wind tunnel specifically designed for convective heat transfer and flow visualization studies. The instability data for critical Grashof number and wavelength are obtained and compared with experimental and theoretical results in literature.

The heat transfer results for free convection over inclined plates have been reported by many investigators and the pertinent literature can be found in the recent works by Rotem and Claassen [14], Fujii and Imura [15], Pera and Gebhart [16], Ackroyd [17] and Chen and Tzuoo [11] and others. The longitudinal vortices in free convection flow over inclined surfaces near the horizontal direction represent the first stage of the laminar-turbulent transition process. This is in contrast to Tollmien-Schlichting wave as the first stage of transition for natural convection on a vertical plate. After the onset of longitudinal vortices, the flow field becomes three-dimensional and the two-dimensional free convection boundary-layer theory is not strictly applicable.

In spite of the importance in applications, the natural convection heat transfer on horizontal or nearly horizontal surfaces has not been studied as extensively as the problem relating to vertical surfaces. In this connection, the Schlieren pictures of temperature fields near various heated objects obtained by Schmidt [18] provide considerable physical insight into the physical phenomena for natural convection. The interference photographs were used by Eckert and Soehngen [19] to study the laminar and turbulent free-convection on a vertical plate. It is thus seen that flow visualization photographs reveal the whole flow field and provide considerable physical insight in understanding the free convection phenomena. It is of particular interest to observe that flow visualization was used extensively by Prandtl [20] in his investigations of fluid motion.

The occurrence of longitudinal vortices in the boundary layer along a concave wall was first shown by Gortler [21] and the related centrifugal instability problems have subsequently been studied by many investigators. The analogy between centrifugal and thermal instability problems is well-known and it is interesting to compare the flow visualization results from this study with those of Gortler vortices. Chandra [22] conducted flow visualization studies on thermal instability of horizontal air layer heated from below using cigarette smoke and for the case with shear the longitudinal rolls were observed. The vortex instability problem also arises when a horizontal Blasius flow is heated from below. This problem was studied by Wu and Cheng [23], Gilpin et al. [24], Takimoto et al. [25] and Moutsoglou et al. [26].

4.2 Apparatus and Experimental Procedure

4.2.1 Wind Tunnel and Isothermal Heating Plate Assembly

The flow visualization experiments were performed in a wind tunnel which can be tilted at any inclination angle from the horizontal direction about the center of the tunnel body. The schematic diagrams for the wind tunnel, the constant temperature plate with auxiliary equipment and a smoke generator with injection device are shown in Fig. 4.1. The dimensions of the tunnel test section are 30.6×30.6×247.6cm, width by height by length. The test surface used in the experiments was fabricated from copper plate with dimensions 6.35mm×152.4cm×24.1cm, thickness by length by width. The test plate was installed as a bottom surface of the test section and the leading edge of the plate was placed flush with the end of the contraction section. The test section except the bottom part was made of acrylic resin plates in order to permit a visual investigation of the flow.

The constant wall temperature condition was provided by circulating water from a hot water tank at high speed through the heating water channel attached below the bottom surface of the test plate. At lower temperature levels, the wall temperature remained practically constant during a complete run due to the large capacity of the hot water tank. At wall temperature levels higher than 50°C, a maximum temperature drop of 1°C was observed during the course of a complete run.

4.2.2 Wall Temperature Measurement

The wall temperature measurements were made by four 0.3mm diameter copper-constantan thermocouples installed at four locations along the side edges of the test plate. The thermocouple was embedded in a 1mm deep depression and covered with aluminum epoxy. The four readings essentially agreed within the calibration error of the thermocouple after steady-state conditions were reached. The inlet and outlet temperatures of the circulating hot water to the test section were also monitored by two 0.8mm iron-constantan sheathed thermocouples(see Fig. 4.1). The difference between the two reading was less than 0.2°C for all temperature levels. The wall temperature was always lower than the heating water temperature up to a maximum of 1°C and the difference decreased at lower temperature levels.

The ambient air temperature was measured using a 25μm copper-constantan thermocouple. The thermocouple junction was made by butt-welding to produce an effective junction diameter of around 50μm. The probe was positioned using a traversing mechanism with an accuracy of 1/50mm. All thermocouples were calibrated in a constant temperature bath against a laboratory grade digital thermometer.

4.2.3 The Flow Visualization Technique and Photographic Arrangement

The smoke was generated by burning paper sticks in a 55mm o.d. copper tube which was connected to the room compressed air. The smoke was then injected through a small slot type smoke injector along the leading edge of the heated test plate. The temperature of the smoke flow at the exit of the smoke injector was checked to be close to the room temperature. The setup is shown in detail in Fig. 4.1.

The transverse cross-sectional views of the developing secondary flow in the form of longitudinal vortices were recorded by a camera using a mirror placed at the end of the test plate with an angle of 45° to the direction of the main flow. The secondary flow was made visible by a sheet of light produced from a 1.5 KW halogen slit light source. The mushroom-like counter-rotating vortices were recorded by the fixed camera projected downwards toward the mirror.

4.2.4 Measurements for the Onset of Instability

The determination of the onset point of the vortex rolls was made by carefully observing the changes in the cross-sectional flow pattern as the slit light source was moved in the downstream direction. The region of two-dimensional laminar flow along the plate was first confirmed. By proceeding further downstream, the critical distance from the leading edge of the heated plate was recorded after detecting the onset of cellular motion. The above procedure was repeated several times to obtain a single data point. The experimental data can be reproduced within a distance of 1cm.

4.3 The Experimental Parameters

The experimental parameters for this investigation are an inclination angle measured from the horizontal direction θ, the constant wall temperature T_w, the wall to ambient temperature difference ΔT and the local Grashof number Gr_x. The ranges of these parameters are given in Table 4.1.

Table 4.1 Range of Experimental Parameters

$\theta = 0, 5, 10, 15, 20°$

$T_w = 34.0 \sim 57.6°C$

$\Delta T = T_w - T_\infty = 15.5 \sim 37.5°C$

$Gr_x = 1.02\times10^6 \sim 2.13\times10^8$

4.4 Result and Discussion

4.4.1 Horizontal Plate

The experiments were conducted in the wind tunnel and the results should be interpreted under this light. The present study is mainly concerned with the vortex instability phenomena in the region with distance from the leading edge x = 0 ~ 50cm and the adjoining surfaces near both ends of the test plate (24.1cm×152.4cm) can be regarded to be adiabatic. The limiting case of natural convection heat transfer from horizontal isothermal surface is of considerable practical and theoretical interest and the related literature is given, for example, by Yousef et al. [27].

The photos depicting the side and top views of the developing longitudinal vortices in natural convection flow along the horizontal isothermal plate with T_w = 51.8°C and T_∞ = 21.0°C are shown in Fig. 4.2. It is noted that at the distances from the leading edge x = 10, 20, 30, 40 and 50cm, the corresponding values for local Grashof number are $Gr_x = 3.54\times10^6$, 2.83×10^7, 9.55×10^7, 2.26×10^8 and 4.42×10^8, respectively. It is seen that after the onset of vortex instability at x = 7cm ($Gr_x = 1.21\times10^6$), the longitudinal vortices develop rather quickly and then the flow becomes turbulent in the range x ≥ 40cm. The corresponding top view shows the smoke tracer lines (7 lines) which represent the up-wash flow in each pair of counter-rotating vortex rolls. These lines also show the approximate locations of the start of the formation of longitudinal vortices and the eventual breakage.

The cross-sectional views of the secondary flow at different axial positions are shown in Fig. 4.3 for $\theta = 0°$ and $\Delta T = 30.8°K$. At x = 9cm the cellular motion already appears and one sees clearly the embryo of the growing longitudinal vortices. The two mushroom-type vortices at both ends might be caused by disturbances due to smoke injection. At x = 15cm the six pairs of vortices are quite stable. At x = 20cm, each vortex pair is seen to be of about the same size. Although not shown here, at different instant, three pairs of vortices are seen to be much larger than the neighboring other three pairs. At x = 25 and 30cm, the different height for each vortex pair is of interest. At x = 35cm, the secondary flow is seen to be not stable and the vortex pair oscillate sidewise. Fig. 4.3 shows the developing region of longitudinal vortices. From Figs. 4.2 and 4.3, one may distinguish three flow regimes consisting of two-dimensional laminar flow, three-dimensional developing flow for longitudinal vortices in the post-critical regime and turbulent flow. One is impressed with the complex flow patterns for natural convection flow along a horizontal isothermal plate. Within the scope of this investigation, the flow separation phenomenon was not studied.

The effect of the temperature difference $\Delta T = T_w - T_\infty$ on developing secondary flow pattern of vortex rolls is of interest and the photos are shown in Fig. 4.4 (a), (b), (c) and (d) for ΔT = 19.4, 25.0, 30.8 and 37.5°C, respectively. The effect of ΔT is clearly seen. The onset of vortex instability occurs at a smaller value of x or Gr_x and the average wavelength tends to decrease significantly as the value of ΔT increases. In Fig. 4.4, the developing secondary flow pattern is of special interest for each ΔT. The temperature dependence of wavelength observed in this study for $\theta = 0°$ was not as prominent as that observed by Sparrow and Husar [1] for inclined plates using water. However, the Prandtl number effect may exist.

4.4.2 Inclined Plate ($0° < \theta \le 20°$)

The overall top and side views of developing longitudinal vortices in a natural convection flow are shown in Fig. 4.5 for θ = 15° and ΔT = 15.5°C. The side view shows a general flow field and one may again distinguish three flow regimes, a two-dimensional laminar flow for x = 0 ~ 10cm, a transition regime with developing longitudinal vortices for x = 10 ~ 35cm and turbulent regime with the eventual breakdown of the longitudinal vortices x ≥ 35cm, characterizing the flow field. For x ≥ 40cm, the smoke rises as plume. For the side view photo, it is of interest to note that at x = 10, 20, 30, 40 and

50cm, the values for Gr_x are 1.99×10^6, 1.59×10^7, 5.36×10^7, 1.27×10^8 and 2.48×10^8, respectively. Thus, the effect of Gr_x on flow pattern can be seen. The top view reveals seven smoke tracer lines showing the approximate locations for the beginning and the breakdown of the developing longitudinal vortices. The lines indicate meandering motion with the amplification of the longitudinal vortices in the main flow direction.

The cross-sectional views of the developing longitudinal vortices in the post-critical regime for θ = 15° and ΔT = 15.5°K are shown in Fig. 4.6. A beginning stage of the formation of longitudinal vortices is characterized by cellular motion. The more or less periodic disturbances in the transverse cross-section provide a fairly good indication of the onset point of the vortex instability in contrast to some uncertainty from the observation of side view alone. The vortex rolls are fairly steady up to x = 20cm and become unsteady with sidewise meandering motion for x > 25cm. It is of interest to observe the varying pitch (wavelength) between two neighboring counter-rotating vortex rolls with the increase of the distance from the leading edge x. The photographic results for θ = 20°, ΔT = 23.1°K are also shown in Fig. 4.7. The unsteady motion can be seen for x > 35cm.

The developing secondary flow patterns at five different inclination angles are shown in Figs. 4.8 (a) to (e) for θ = 0, 5, 10, 15 and 20°, respectively, with ΔT = 18.3 - 19.4°K and x = 10, 15, 20 and 25cm. The arrangement of the photos with identical downstream locations facilitates a direct comparison of the developing secondary flow patterns at different inclination angles. By observing the flow patterns at x = 10cm, one can see clearly the onset point of vortex instability is gradually being delayed as the inclination angle increases from the horizontal direction θ = 0°. This is due to the decreasing buoyancy force component normal to the plate as the inclination angle increases and can be seen from the factor $g \cos\theta$. The wavelength of the vortex rolls does not seem to vary significantly with the increase of inclination angle. The photos presented provide considerable physical insight into the developing longitudinal vortices in natural convection flows along inclined isothermal plates. Within the scope of present investigation, the effect of the inclination angle on the wavelength appears to be rather weak. This observation agrees with that of Sparrow and Husar [1] using water.

4.4.3 Instability Results and Wavelength Correlation

Measurements for the critical distance marking the onset of vortex instability were also made in the course of the flow visualization study. At each inclination angle, eight or nine independent determinations for the onset point were made with wall to ambient temperature difference ΔT ranging from 15 to 45°K. The mean and standard deviation of the critical Grashof number for each inclination angle were computed and the results are shown in Table 4.2. In order to facilitate comparison with other instability data, the critical Grashof number Gr_x^* was defined.

Table 4.2 Critical Grashof Numbers and Standard Deviations

θ	Gr_x^*	σ
0°	8.86×10^5	2.51×10^5
5°	1.03×10^6	6.45×10^5
10°	1.53×10^6	7.08×10^5
15°	1.95×10^6	1.13×10^6
20°	2.13×10^6	1.02×10^6

The instability data are presented in the form of mean critical Grashof number as a function of inclination angle in Fig. 4.9 where the theoretical and experimental results from literature are also plotted for comparison. The error bar indicates the maximum and minimum values of the instability data at each inclination angle. It is seen that theory predicts over three orders of magnitude lower values of critical Grashof number for air (Pr = 0.7) than the present experiment. The same remark also applies to the instability data of Lloyd and Sparrow [2] for the case of water (Pr = 7). The large discrepancy may be attributed to the fact that the linear stability theory is based on infinitesimal disturbances and the experimental determination of the onset point requires a certain amplification of the formation process. However, the exact reasons for the large discrepancy between theory and experiment remain to be clarified. It is noted that the general trend as revealed by the slope of the present instability data is in good agreement with that predicted by theory. The trend of the present data also appears to be in agreement with the air data by Lock et al. [28] for inclination angles $\theta > 35°$.

For the case of horizontal plate, it is possible to compare the present instability data with those of Rotem and Claassen [29] and the results are shown in Fig. 4.10. The agreement is seen to be satisfactory.

The mean wavelength of the vortex rolls is also of particular interest. The measurements of the wavelength were made directly from the photographs of the cross-sectional views using the distance between two lines in the photos representing the inner walls of the test section as reference. The wavelengths of vortex rolls at a particular cross-section were then averaged to obtain a single data point for the mean wavelength. The results are plotted in Fig. 4.11 together with theoretical predictions from Chen and Tzuoo [11]. The following correlation equation for wavelength is also obtained.

$$x_c/\lambda = C\ Gr_x^{*1/4} \tag{4.1}$$

where C = 0.088 and 0.068 for upper and lower bounds, respectively. It is noted that $Gr_x^{1/2}$ may be regarded to be a Reynolds number Re_x.

4.5 Concluding Remarks

The problem of vortex instability of natural convection flow over horizontal or slightly inclined isothermally heated flat plate was studied by a flow visualization technique using smoke for inclination angles from horizontal direction θ = 0, 5, 10, 15 and 20°. The photographs showing the developing longitudinal vortices and the instability data are presented. The three flow regimes characterizing the natural convection flow are shown to be two-dimensional laminar flow regime, transition regime for developing longitudinal vortices and turbulent regime. The experimental results are compared with theoretical predictions.

The present vortex instability problem for natural convection flow along an inclined isothermal plate is somewhat analogous to centrifugal instability problem for Gortler vortices in the boundary layer along a concave wall. The secondary flow pattern in a cross-section normal to the main flow for Gortler vortices shown in Fig. 4.4 by Aihara and Koyama [30], for example, is strikingly similar to the flow patterns shown in this investigation dealing with vortex instability due to buoyancy forces. The flow visualization study provides considerable insight into the structure and nature of the developing longitudinal vortices in the transition regime for natural convection flow heated from below. The problem of transition from laminar to turbulent flow through developing longitudinal vortices apparently needs further investigations.

4.6 References

1. Sparrow, E.M., and Husar, R.B., "Longitudinal Vortices in Natural Convection Flow on Inclined Plates," J. Fluid Mech., Vol. 37, 1969, pp. 251 - 255.

2. Lloyd, J.R., and Sparrow, E.M., "On the Instability of Natural Convection Flow on Inclined Plates," J. Fluid Mech., Vol. 42, 1970, pp. 465 - 470.

3. Lloyd, J.R., "Vortex Wavelength in the Transition Flow Adjacent to Upward Facing Inclined Isothermal Surfaces," Procs. 5th Int. Heat Transfer Conference, Vol. 3, 1974, pp. 34 - 37.

4. Haaland, S.E., and Sparrow, E.M., "Vortex Instability of Natural Convection Flow on Inclined Surfaces," Int. J. Heat and Mass Transfer, Vol. 16, 1973, pp. 2355 - 2367.

5. Hwang, G.J., and Cheng, K.C., "Thermal Instability of Laminar Natural Convection Flow on Inclined Isothermal Plates," Canadian J. of Chemical Engineering, Vol. 51, 1973, pp. 659 - 666.

6. Kahawita, R.A., and Meroney, R.N., "The Vortex Mode of Instability in Natural Convection Flow Along Inclined Plates," Int. J. Heat Mass Transfer, Vol. 17, 1974, pp. 541 - 548.

7. Lee, J.B., and Lock, G.S.H., "Instability in Boundary-Layer Free Convection along an Inclined Plate," Trans. Canadian Soc. for Mechanical

Engineering, Vol. 1, 1972, pp. 197 - 203.

8. Haaland, S.E., and Sparrow, E.M., "Wave Instability of Natural Convection on Inclined Surfaces Accounting for Nonparallelism of the Basic Flow, " ASME Journal of Heat Transfer, 1973, pp. 405 - 407.

9. Pera, L., and Gebhart, B., "On the Stability of Natural Convection Boundary Layer Flow Over Horizontal and Slightly Inclined Surfaces," Int. J. Heat Mass Transfer, Vol. 16, 1973, pp. 1147 - 1163.

10. Iyer, P.A., and Kelly, R.E., "The Stability of the Laminar Free Convection Flow Induced by a Heated Inclined Plate," Int. J. Heat Mass Transfer, Vol. 17, 1974, pp. 517 - 525.

11. Chen, T.S., and Tzuoo, K.L., "Vortex Instability of Free Convection Flow over Horizontal and Inclined Surfaces," ASME Journal of Heat Transfer, Vol. 107, 1982, pp. 637 - 643.

12. Tzuoo, K.L., Chen, T.S. and Armaly, B.F., " Wave Instability of Natural Convection Flow on Inclined Surfaces," ASME Journal of Heat Transfer, Vol. 107, 1985, pp. 107 - 111.

13. Hsu, C.T., and Cheng, P., "Vortex Instability in Buoyancy-Induced Flow Over Inclined Heated Surfaces in Porous Media," ASME Journal of Heat Transfer, Vol. 101, 1979, pp. 660 - 665.

14. Rotem, Z., and Claassen, L., "Free Convection Boundary-Layer Flow Over Horizontal Plates and Discs," Canadian J. Chemical Engineering, Vol. 47, 1969, pp. 461 - 468.

15. Fujii, J., and Imura, H., "Natural-Convection Heat Transfer from a Plate with Arbitrary Inclination," Int. J. Heat Mass Transfer, Vol. 15, 1972, pp. 755 - 767.

16. Pera, L., and Gebhart, B., "On the Stability of Natural Convection Boundary Layer Flow Over Horizontal and Slightly Inclined Surfaces," Int. J. Heat Mass Transfer, Vol. 16, 1973, pp. 1147 - 1163.

17. Ackroyd, J.A.D., "Laminar Natural Convection Boundary Layers on Near-Horizontal Plates," Proc. R. Soc. Lond., Vol. 352A, 1976, pp. 249 - 274.

18. Schmidt, E., "Schlierenaufnahmen des Temperaturfeldes in Der Nahe Warmeabgebender Korper," Forsch. Geb. Ingwes., Vol. 3, 1932, pp. 181 - 189.

19. Eckert, E.R.G., and Soehnghen, E., "Interferometric Studies on the Stability and Transition to Turbulence of A Free Convection Boundary Layer," General Discussion on Heat Transfer, Institution of Mechanical Engineers, 1951, pp. 321 - 323.

20. Prandtl, L., "The Generation of Vortices in Fluids of Small Viscosity," Royal Aeronautical Soc., Vol. 31, 1927, 720 - 743.

21. Gortler, H., "Uber eine dreidimensionale Instabilitat laminarer Grenzschichten an konkaven Wander," Nachr. Ges. Wiss. Gottingen, Math.-phys., 1940, kl. 2(1).

22. Chandra, K., "Instability of Fluids Heated from Below," Proc. Roy. Soc., Vol. 164A, 1938, pp. 231 - 242.

23. Wu, R.S., and Cheng, K.C., "Thermal Instability of Blasius Flow along Horizontal Plates," Int. J. Heat Mass Transfer, Vol. 19, 1976, pp. 907 - 913.

24. Gilpin, R.R., Imura, H., and Cheng, K.C., "Experiments on the Onset of Longitudinal Vortices in Horizontal Blasius Flow Heated from Below," ASME Journal of Heat Transfer, Vol. 100, 1978, pp. 71 - 77.

25. Takimoto, A., Hayashi, Y., and Matsuda, O., "Thermal Stability of Blasius Flow Over a Horizontal Flat Plate," Heat Transfer-Japanese Research, Vol. 12, 1983, pp. 19 - 33.

26. Moutsoglou, A., Chen, T.S., and Cheng, K.C., "Vortex Instability of Mixed Convection Flow Over a Horizontal Flat Plate," ASME Journal of Heat Transfer, Vol. 103, 1981, pp. 257 - 261.

27. Yousef, W.W., Tarasuk, J.D., and Mckeen, "Free Convection Heat Transfer from Upward-Facing Isothermal Surfaces," ASME Journal of Heat Transfer, Vol. 104, 1982, pp. 493 - 500.

28. Lock, G.S.H., Gort, C., and Pond, G.R., "A Study of Instability in Free Convection from an Inclined Plate," Applied Scientific Research, Vol. 18, 1967, pp. 171 - 182.

29. Rotem, Z., and Claassen, L., "Natural Convection above Unconfined Horizontal Surfaces," J. Fluid Mech., Vol. 38, 1969, pp. 173 - 192.

30. Aihara, Y., and Koyama, H., "Secondary Instability of Gortler Vortices: Formation of Periodic

Three-Dimensional Coherent Structure," Trans. Japan Soc. Aeronautical and Space Sciences, Vol. 24, 1981, pp. 78 - 94.

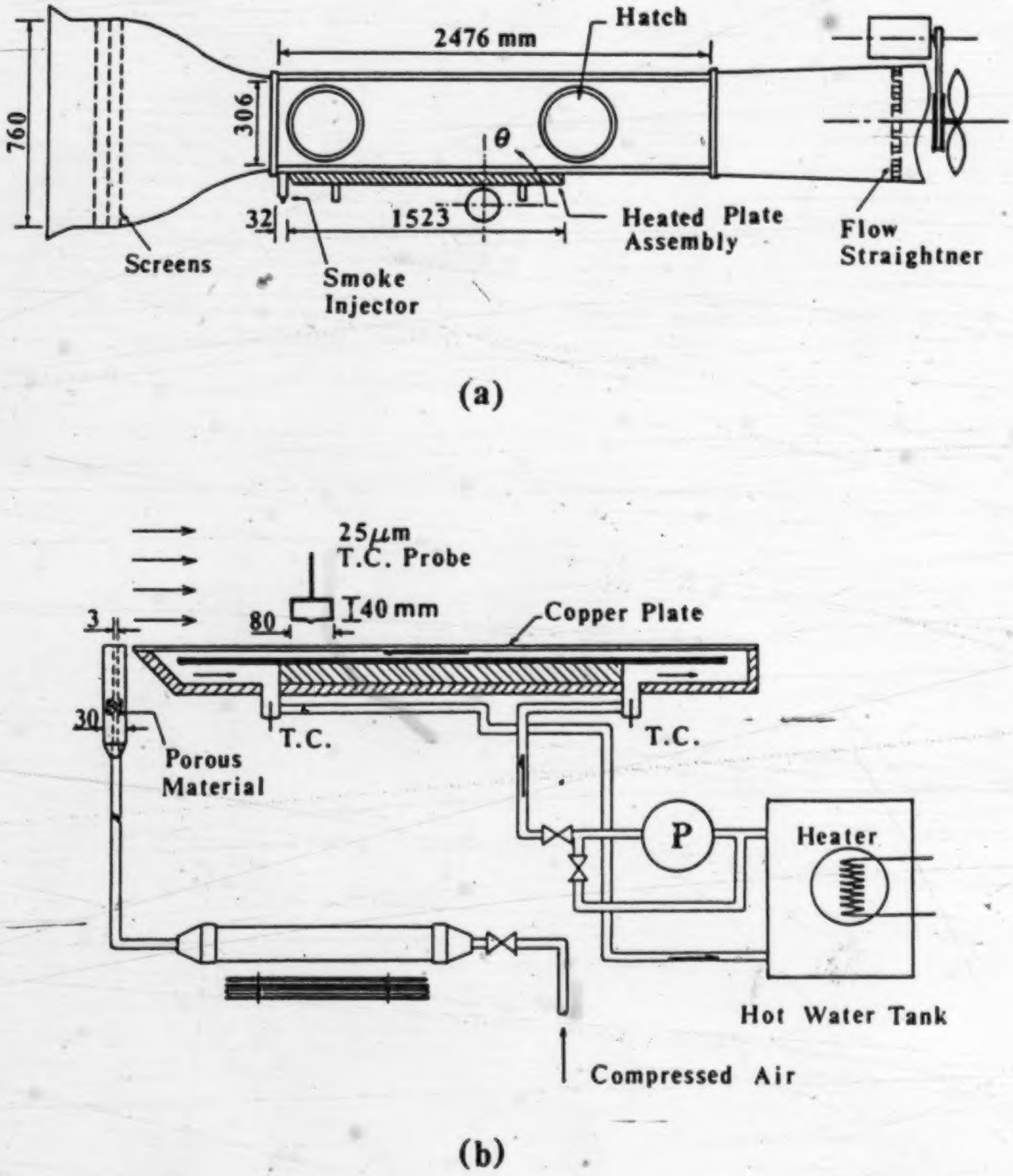
Hatch
2476 mm
760
306
θ
32
1523
Heated Plate Assembly
Flow Straightner
Screens
Smoke Injector
(a)
25μm T.C. Probe
40 mm
3
80
Copper Plate
30
T.C.
T.C.
Porous Material
P
Heater
Hot Water Tank
Compressed Air
(b)

Fig. 4.1 Schematic Diagrams for (a) Wind Tunnel Test Facility and (b) Constant Temperature Plate and Auxiliary Equipment

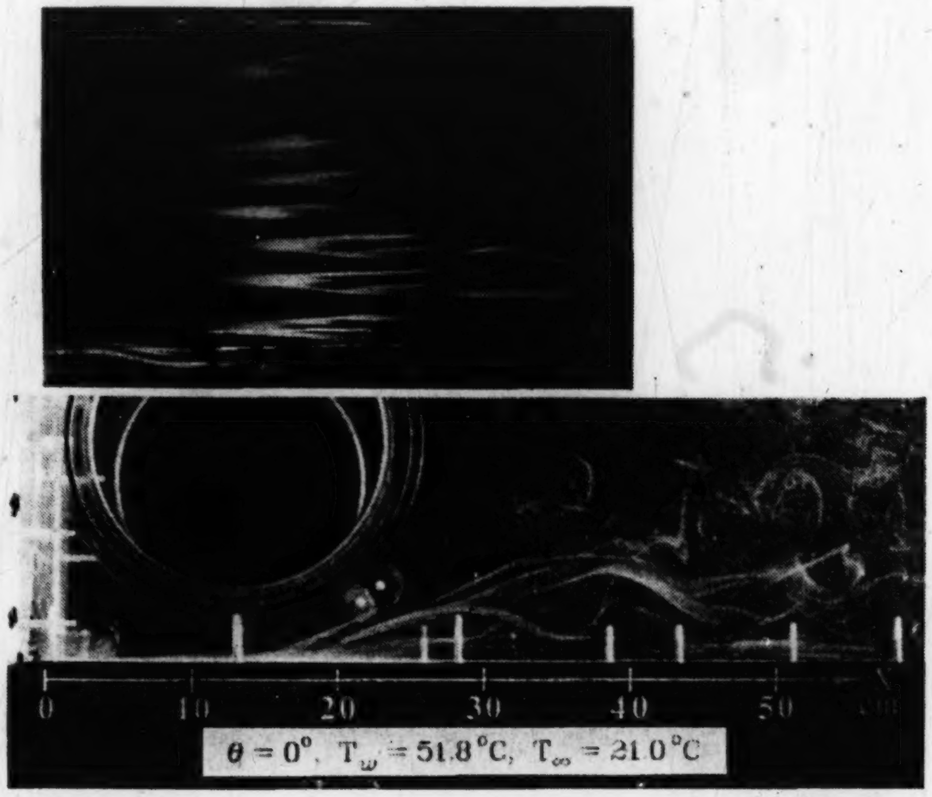
0
10
20
30
40
50
cm
$\theta = 0^\circ$, $T_w = 51.8^\circ C$, $T_\infty = 21.0^\circ C$

Fig. 4.2 Top and Side Views of Developing Longitudinal Vortices for $\theta=0^\circ$, $T_w=51.8^\circ C$ and $T_\infty=21.0^\circ C$

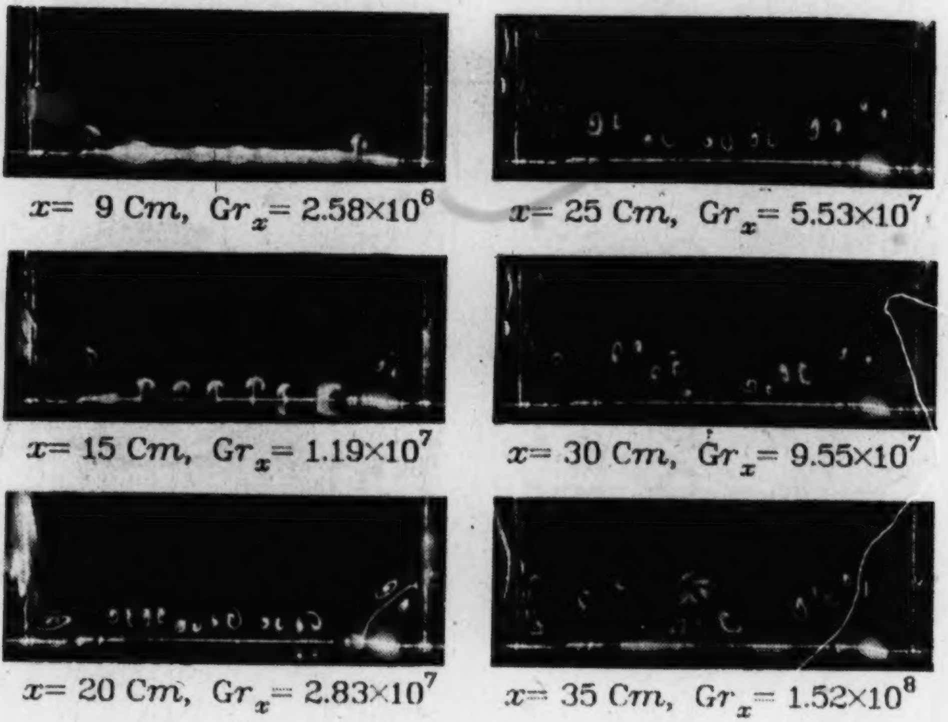

$x = 9$ Cm, $Gr_x = 2.58\times10^6$

$x = 25$ Cm, $Gr_x = 5.53\times10^7$

$x = 15$ Cm, $Gr_x = 1.19\times10^7$

$x = 30$ Cm, $Gr_x = 9.55\times10^7$

$x = 20$ Cm, $Gr_x = 2.83\times10^7$

$x = 35$ Cm, $Gr_x = 1.52\times10^8$

Fig. 4.3 Cross-sectional Views of Secondary Flow Patterns for $\theta=0°$ and $\Delta T=30.8°K$

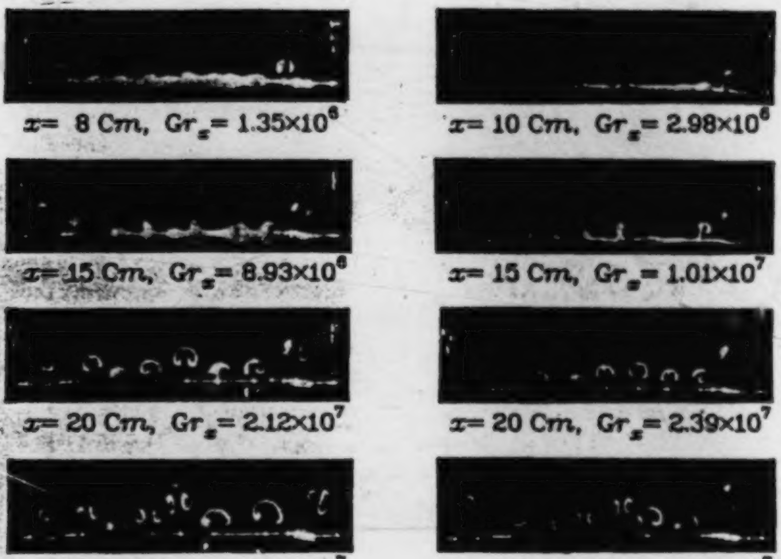

x= 8 Cm, Gr_x= 1.35×10^6

x= 15 Cm, Gr_x= 8.93×10^6

x= 20 Cm, Gr_x= 2.12×10^7

x= 25 Cm, Gr_x= 4.13×10^7

(a) ΔT= 21.7 °K

x= 10 Cm, Gr_x= 2.98×10^6

x= 15 Cm, Gr_x= 1.01×10^7

x= 20 Cm, Gr_x= 2.39×10^7

x= 25 Cm, Gr_x= 4.66×10^7

(b) ΔT= 25.0 °K

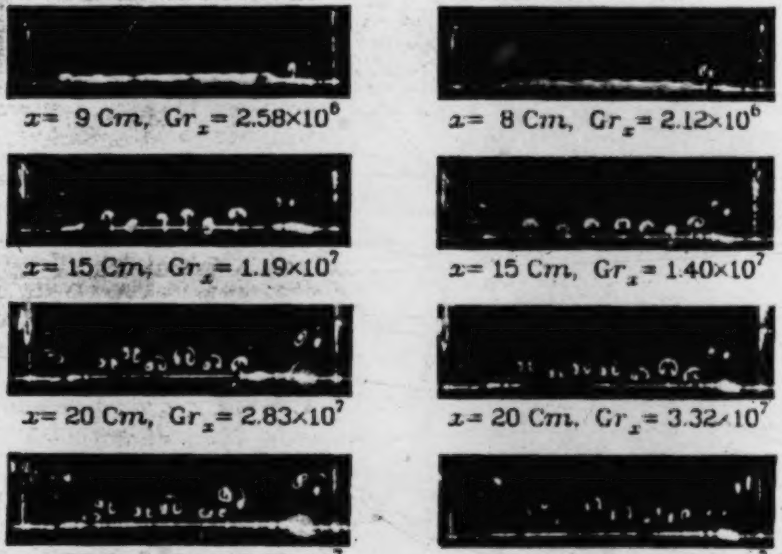

x= 9 Cm, Gr_x= 2.58×10^6

x= 15 Cm, Gr_x= 1.19×10^7

x= 20 Cm, Gr_x= 2.83×10^7

x= 25 Cm, Gr_x= 5.53×10^7

(c) ΔT= 30.8 °K

x= 8 Cm, Gr_x= 2.12×10^6

x= 15 Cm, Gr_x= 1.40×10^7

x= 20 Cm, Gr_x= 3.32×10^7

x= 25 Cm, Gr_x= 6.48×10^7

(d) ΔT= 37.5 °K

Fig. 4.4 Effect of ΔT on Developing Secondary Flow Patterns for θ= 0°

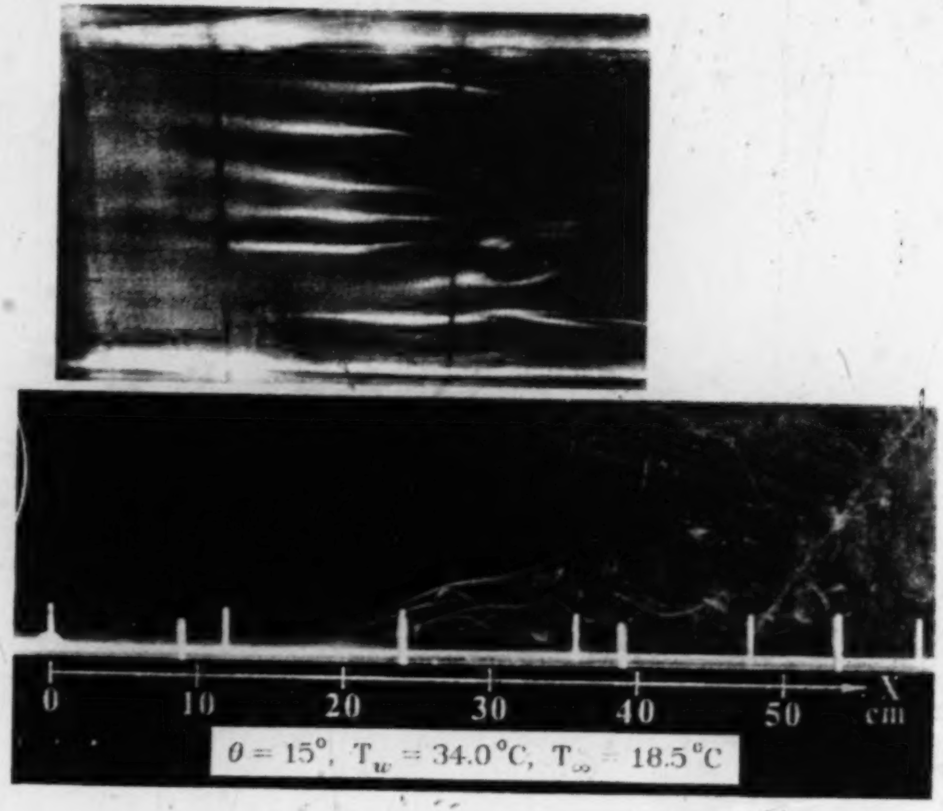
0
10
20
30
40
50
X
cm
$\theta = 15^\circ$, $T_w = 34.0^\circ C$, $T_\infty = 18.5^\circ C$

Fig. 4.5 Top and Side Views of Developing Longitudinal Vortices for θ=15°, T_W=34.0°C and T_∞=18.5°C

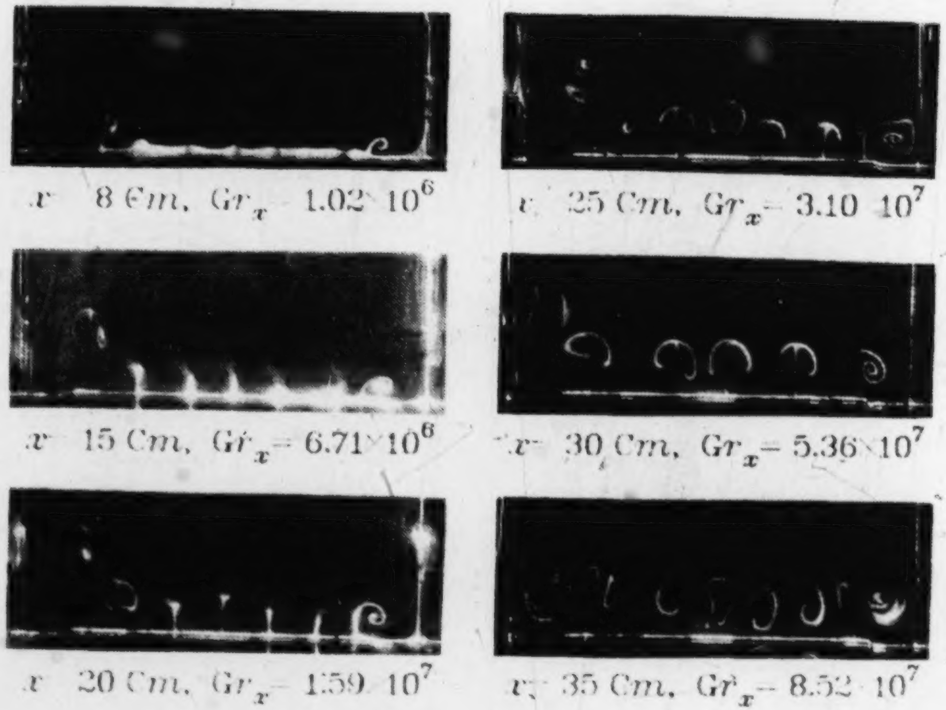

$x = 8$ Cm, $Gr_x = 1.02 \times 10^6$

$x = 15$ Cm, $Gr_x = 6.71 \times 10^6$

$x = 20$ Cm, $Gr_x = 1.59 \times 10^7$

$x = 25$ Cm, $Gr_x = 3.10 \times 10^7$

$x = 30$ Cm, $Gr_x = 5.36 \times 10^7$

$x = 35$ Cm, $Gr_x = 8.52 \times 10^7$

Fig. 4.6 Cross-sectional Views of Secondary Flow Patterns for $\theta=15°$ and $\Delta T=15.5°K$

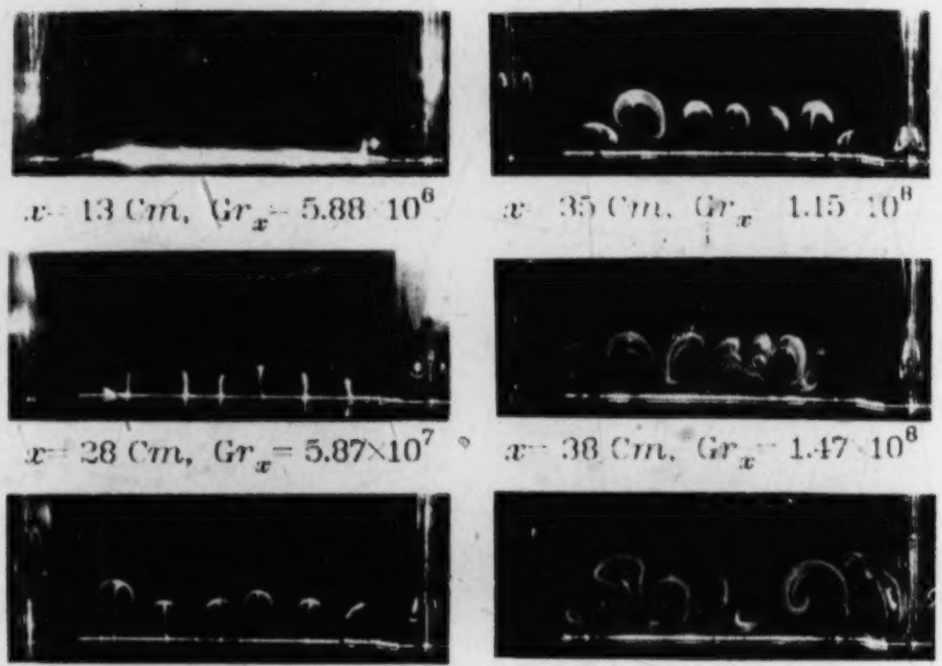

$x = 13$ Cm, $Gr_x = 5.88 \times 10^6$

$x = 35$ Cm, $Gr_x = 1.15 \times 10^8$

$x = 28$ Cm, $Gr_x = 5.87 \times 10^7$

$x = 38$ Cm, $Gr_x = 1.47 \times 10^8$

$x = 33$ Cm, $Gr_x = 9.61 \times 10^7$

$x = 43$ Cm, $Gr_x = 2.13 \times 10^8$

Fig. 4.7 Cross-sectional Views of Secondary Flow Patterns for $\theta=20°$ and $\Delta T=23.1°K$

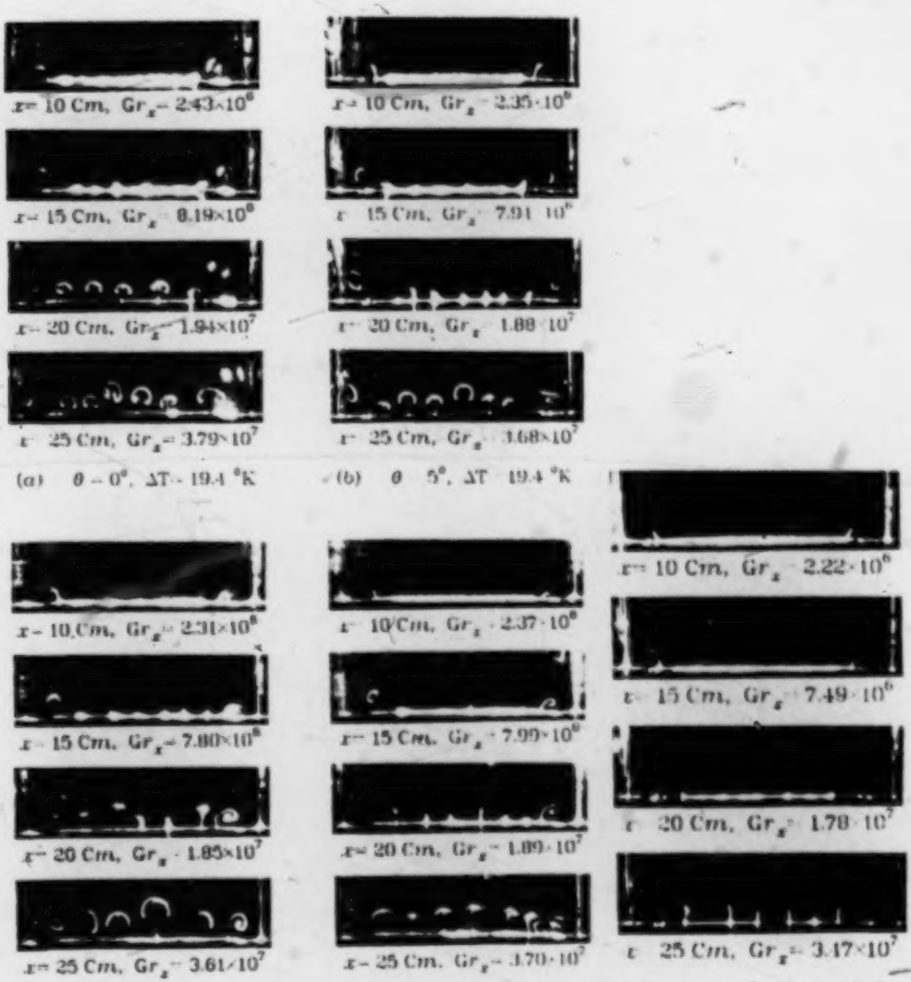
$x = 10$ Cm, $Gr_x = 2.43\times10^6$
$x = 15$ Cm, $Gr_x = 8.19\times10^6$
$x = 20$ Cm, $Gr_x = 1.94\times10^7$
$x = 25$ Cm, $Gr_x = 3.79\times10^7$
$x = 10$ Cm, $Gr_x = 2.35\times10^6$
$x = 15$ Cm, $Gr_x = 7.91\times10^6$
$x = 20$ Cm, $Gr_x = 1.88\times10^7$
$x = 25$ Cm, $Gr_x = 3.68\times10^7$
$x = 10$ Cm, $Gr_x = 2.31\times10^6$
$x = 15$ Cm, $Gr_x = 7.80\times10^6$
$x = 20$ Cm, $Gr_x = 1.85\times10^7$
$x = 25$ Cm, $Gr_x = 3.61\times10^7$
$x = 10$ Cm, $Gr_x = 2.37\times10^6$
$x = 15$ Cm, $Gr_x = 7.99\times10^6$
$x = 20$ Cm, $Gr_x = 1.89\times10^7$
$x = 25$ Cm, $Gr_x = 3.70\times10^7$
$x = 10$ Cm, $Gr_x = 2.22\times10^6$
$x = 15$ Cm, $Gr_x = 7.49\times10^6$
$x = 20$ Cm, $Gr_x = 1.78\times10^7$
$x = 25$ Cm, $Gr_x = 3.47\times10^7$

(a) $\theta = 0^\circ$, $\Delta T = 19.4$ °K

(b) $\theta = 5^\circ$, $\Delta T = 19.4$ °K

(c) $\theta = 10^\circ$, $\Delta T = 18.3$ °K

(d) $\theta = 15^\circ$, $\Delta T = 19.2$ °K

(e) $\theta = 20^\circ$, $\Delta T = 19.4$ °K

Fig. 4.8 Effect of Inclination Angle on Developing Secondary Flow Patterns for $\phi=0^\circ$

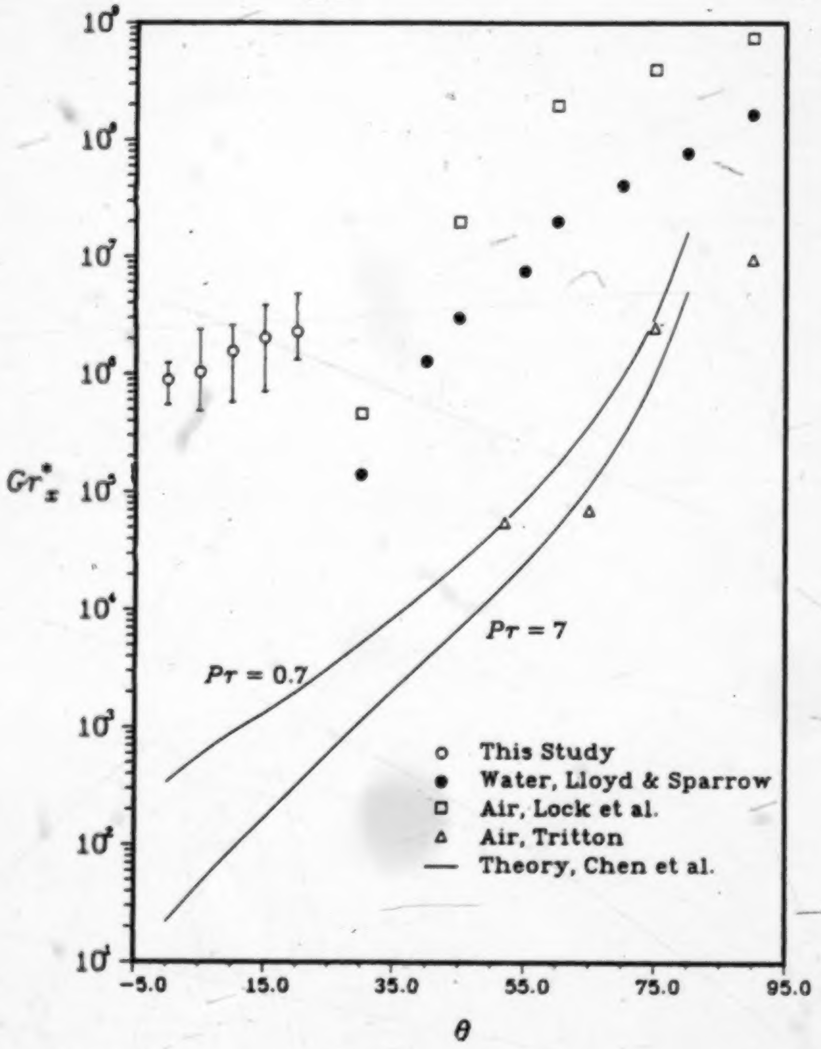

Fig. 4.9 Variation of Critical Grashof Number with Inclination Angle

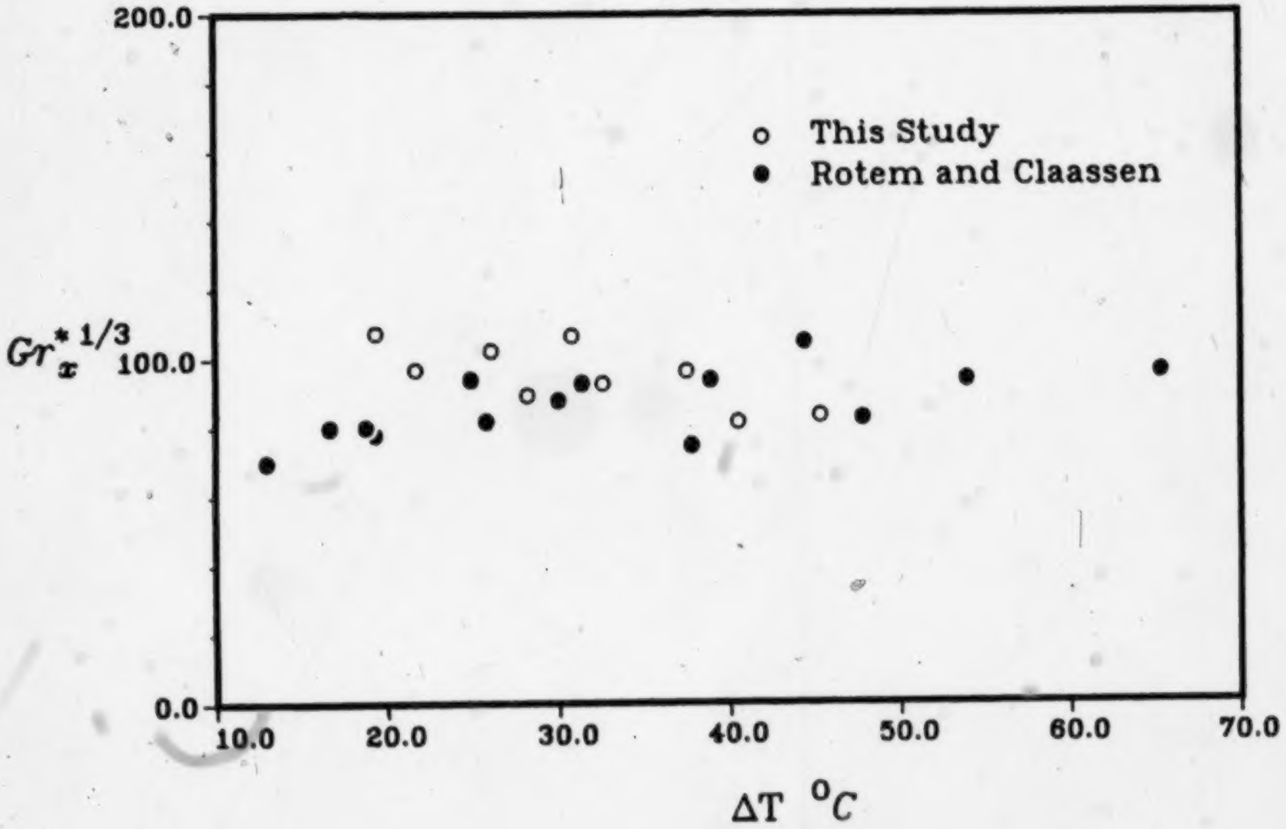

Fig. 4.10 Critical Grashof Number for Horizontal Plate

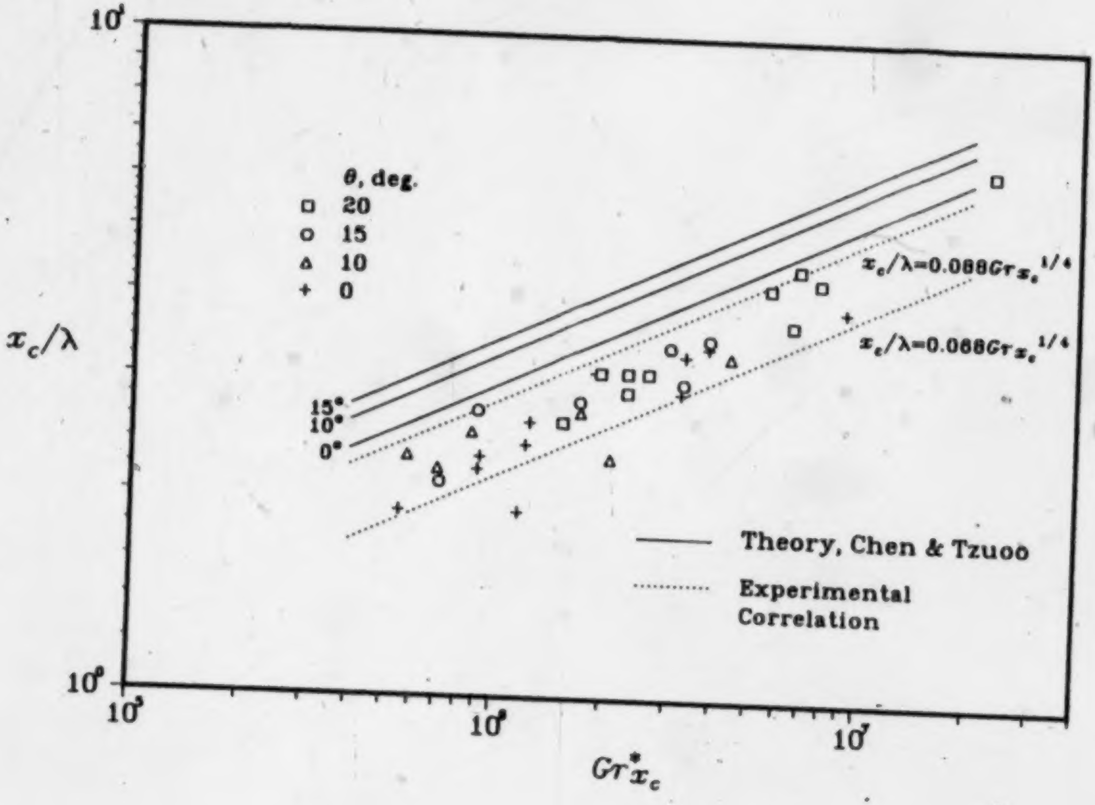

Fig. 4.11 Correlation for the Wavelength of Vortex Rolls

5. Flow Visualization Study on the Vortex Instability in a Horizontal Blasius Flow Heated From Below

5.1 Introduction

If a laminar boundary layer over a horizontal flat plate is heated from below, a top-heavy situation may arise due to the density variations near the heated surface. The potentially unstable flow situation eventually breaks down as the buoyancy forces increase and the flow is characterized by secondary flow motion in the form of the longitudinal vortex rolls which are more or less periodic in the spanwise direction. The vortex rolls grow to a finite amplitude forming a post-critical flow regime and finally break up into turbulent motions. Once the vortex instability is set up, the flow field takes a three-dimensional characteristic and the conventional two-dimensional theory can no longer be applied in that flow regime.

The linear instability theory regarding the onset of the longitudinal vortex rolls in a horizontal Blasius flow was first applied by Wu and Cheng [1]. Subsequently, experimental instability results were obtained by Gilpin, Imura and Cheng [2] in a flow visualization study in water employing an electro-chemical technique. Their flow visualization results clearly revealed the existence of longitudinal vortex rolls in a horizontal Blasius flow over an isothermally heated flat plate. Measurements for temperature profiles and heat transfer coefficients in the post-critical regime were made by Imura, Gilpin and Cheng [3] using water as the flow medium. Takimoto and Hayashi [4] conducted a similar experiment in a wind tunnel and also presented an analytical instability result. Recently, more refined theoretical instability results were suggested by Moutsoglou, Chen and Cheng [5].

The purpose of this chapter is to present the flow visualization photographs showing the onset and the subsequent growth of the longitudinal vortex rolls observed in a horizontal Blasius flow over an isothermally heated flat plate. Attention was given to the effect of an unheated length on the secondary flow motion and the instability characteristics. It is noted that no theoretical or experimental studies regarding the effect of an unheated length on the instability characteristics are yet available in the literature.

The side and top views and the cross-sectional views of the longitudinal vortex rolls are presented for three different unheated lengths: x_o= 0 , 33.5 and 60.5 cm. For the case of x_o= 0 cm, photographs showing the effects of the wall to free stream temperature difference and the free stream velocity on the cross-sectional secondary flow patterns of the vortex rolls are presented. Instability data for the critical Grashof number were also obtained for three different cases of unheated length and compared with the theoretical results available in the literature.

5.2 Apparatus and Experimental Procedure

5.2.1 Wind Tunnel and Isothermal Heating Plate

The schematic diagrams for the wind tunnel, the constant temperature plate assembly and the smoke generation facilities are shown in Fig. 4.1 in Chapter 4. The wind tunnel was a suction low speed wind tunnel driven by a variable speed DC moter. The test section dimensions were 30.6×30.6×247.6 cm, width by height by length. The top and side walls of the test section were made of acrylic resin to facilitate flow visualization studies. The inlet contraction ratio of the wind tunnel was 0.40 and a steady air flow between 0.1 ~ 0.86 m/s was provided by a fan installed at the tunnel outlet. The free stream air velocity was measured by a TSI hot film anemometer with an accuracy of 0.01 m/s

The test plate was a copper plate of 6.35mm×152.4cm×24.1cm, thickness by length by width. The test plate was assembled as the top part of a heating water channel fabricated from acrylic resin. The isothermal heating conditon was provided by circulating hot water through the heating water channel in counterflow direction from a constant temperature hot water tank. The constant temperature plate assembly was installed as a bottom surface of the wind tunnel test section and was freely relocated in the direction of main flow as an unheated length was added.

5.2.2 Wall and Air Temperature Measurements

The wall temperature measurements were taken by four 0.3mm copper-constantan thermocouples installed along the side edges of the test plate. The four readings agreed within the calibration error of the thermocouple after a steady-state condition was reached. The temperature of the circulating hot water was measured at the inlet and outlet of the heating water channel and less than 0.2°C difference was observed between the two readings. The wall temperature was usually 1°C lower than the average of the inlet and outlet water temperature. The steady-state condition was assumed to be reached if the wall temperature remained constant over a 10 minute interval while the wind tunnel and the water circulation unit were in continuous operation.

The air temperature profiles were measured by a 25μm copper-constantan thermocouple. The probe was fabricated from a stainless steel tube and formed into the shape of a rectangular loop to prevent the thermocouple wires near the junction from being subject to a temperature gradient in the vertical direction (see Fig. 4.1 (b) in Chapter 4). It was positioned using a traversing mechanism with an accuracy of 1/50mm.

5.2.3 The Flow Visualization Technique and Photographic Arrangement

The flow visualization technique used in the present study is a smoke injection method. The smoke was generated by burning paper sticks in a copper tube connected to the room compressed air. It was injected through a slot type smoke injector along the leading edge of the test plate.

The cross-sectional views of the developing longitudinal vortices were photographed by a camera fixed downward using a mirror placed at the end of the test plate with an angle of 45° from the horizontal direction. The cross-sectional secondary flow patterns of the vortex rolls were made visible by passing a sheet of light produced from a 1.5kw halogen slit light source perpendicular to the direction of the main flow.

5.2.4 Measurements for the Onset of Instability

The determination of the onset point of the vortex rolls was made by locating the point of the first occurrence of the cellular motions using a sheet of light produced from the halogen slit light source. Unlike the case of natural convection flow in the previous chapter, the range of the occurrence of vortex rolls was observed to be rather lengthy (usually 5 ~ 15 cm depending on the free stream velocity). The cellular motions at a given cross-section near the onset point also fluctuated in time. Therefore, the critical distance marking the onset of vortex rolls was not a precise quantity. For these reasons, the determination of the onset of instability was made over a region of uncertainty bounded by the cross-section where the occurrence of the cellular motions was occasionally detected and the cross-section where the onset of vortex rolls was continuously observed.

5.2.5 Range of Experimental Parameters

The experimental parameters for the present study are the free stream velocity U_∞, the wall to free stream air temperature difference ΔT, the unheated lenght x_o, the local Reynolds number Re_x, and the local Grashof number $Gr_{x'}$ where $x'=x-x_o$. The property values for Re_x and $Gr_{x'}$ were all evaluated at the film temperature which is the average of freestream temperature and wall temperature. The range of these parameters are given in Table 5.1.

Table 5.1 Range of Experimental Parameters

$U_\infty = 0.01 \sim 0.72$ m/s

$\Delta T = T_w - T_\infty = 6.9 \sim 33.6$°K

$x_o = 0 \sim 60.5$ cm

$Re_x = 192 \sim 36{,}250$

$Gr_{x'} = 4.95\times10^4 \sim 5.23\times10^8$

5.3 Results and Discussion

5.3.1 Air Temperature Profiles

In order to confirm the existence of a Blasius flow in the present wind tunnel, measurements for air temperature profiles were made for the case of stable flow (without vortices). Fig. 5.1 shows the results of four different temperature profile measurements taken in the mid-region of the test plate. The local air temperature T_∞ was nondimensionalized using the wall and free stream temperature and the vertical distance y was nondimensionalized by the thermal boundary layer thickness δ_t obtained experimentally. The solid curve represents the Von Karman's approximate solution for laminar boundary layer temperature profile. The agreement between the theory and experiments is considered to be reasonable for the present study.

5.3.2 Results of Flow Visualization Study

The photographs of the side and top views of the buoyancy induced longitudinal vortex rolls in a horizontal Blasius flow over an isothermal plate with T_W=57.4°C and T_∞=29.5°C for the case of U_∞= 0.05 m/s and x_o=0 cm are shown in Fig. 5.2.

An inspection of side view suggests the existence of three different flow regimes, i.e. the two-dimensional boundary layer flow regime, the post-critical regime following the onset of vortex rolls and the turbulent regime. In general, the present observation for the overall side view is very similar to that of [2]. The top view clearly shows the existence of longitudinal vortex rolls. Six pairs of vortex rolls which are more or less periodic across the width of the test plate can be identified.

The cross-sectional views of the onset and growth of longitudinal vortex rolls are shown in Fig. 5.3. The complex but well organized secondary flow motions are clearly revealed. For this flow condition, the onset of vortex rolls was first detected at x'=0.07 m. As shown by the photograph for $Re_x=204$ and $Gr_{x'}=1.01\times10^6$, the onset is observed as the occurrence of small cellular motions across the width of the test plate. The following photographs show that each of the cellular motions is the origin of a pair of longitudinal vortex rolls. At $Re_x=729$ and 4.59×10^7, the vortex rolls are nearly fully developed. Comparing with the next photograph i.e. at $Re_x=874$ and $Gr_{x'}=7.93\times10^7$, one notices some discrepancy in the number of vortex pairs. Up to $Re_x=729$ and $Gr_{x'}=4.59\times10^7$, eight pairs of vortex rolls are clearly observed in the mid-regin across the test plate. At $Re_x=874$ and $Gr_{x'}=7.93\times10^7$, 7 pairs can be identified. This is obviously due to the pairing of the vortex rolls occurring in the downstream direction. The photograph at $Re_x=1,020$

and $Gr_{x'}=1.26\times10^8$ shows the oscillating vortex rolls near the transition to turbulence regime. Although not shown here, the six vortex rolls in the photograph were observed to form into three or four pairs at this location.

The side and top views of the developing longitudinal vortex rolls for the case of $x_o=33.5$cm are shown in Fig. 5.4. The free stream velocity was 0.04 m/s, and the wall and free stream temperature were 56.0°C and 27.8°C, respectively. No significant difference can be observed in the overall side view as compared with the case of $x_o=0$ cm. However, the top view shows less number of vortex rolls than the case of $x_o=0$ cm. Fig. 5.5 shows the corresponding cross-sectional views of the developing vortex rolls. The vortex rolls near the side walls(indicated as a white vertical line on each side of the photograph) were observed to be disturbed by the side walls. It is believed that this is due to the early development of a hydrodynamic boundary layer along the side wall resulting from the presence of an unheated length. However, the three pairs of vortex rolls in the mid-region are observed to be quite stable and persist well up to $Re_x=1,597$ and $Gr_{x'}=1.28\times10^8$. At $Re_x=1,714$ and $Gr_{x'}=1.91\times10^8$, only three pairs can be barely identified.

Fig. 5.6 shows the side and top views of the longitudinal vortex rolls for the case of $x_o=60.5$cm with $U_\infty=0.04$ m/s, $T_w=58.5$°C and 26.4°C. In general, the overall shape of the developing flow field revealed by the side and top views do not significantly differ from the preceding two cases of different unheated length. The corresponding cross-sectional views given in Fig. 5.7 show quite stable vortex rolls. The number of vortex rolls are slightly larger than the case of x_o=33.5 cm. However, the increased side wall effects can be still observed. The photograph at Re_x=2,208 and $Gr_{x'}=1.43\times10^8$ again suggests the pairing phenomenon of vortex rolls.

From the comparison of the photographs showing the overall side and top views and cross-sectional views for different unheated length, x_o, one may notice that the vortex rolls are in general less stable with the presence of an unheated length. One may also find that no distinct trend can be observed in regard to the average wavelength of the vortex rolls with increasing unheated length.

The effect of the wall to free stream temperature difference ΔT on the developing secondary flow patterns of the vortex rolls were studied and the results for the case of x_o= 0 cm are shown in Fig. 5.8 (a), (b), (c) and (d), for ΔT=13.6, 16.3, 19.7 and 27.9°C, respectively. The effect of the increasing wall to free stream temperature difference is clearly observed as the increasing number of vortex pairs. Then, the average wavelength consequently decreases with increasing ΔT. Another distinct trend is that the onset of vortex rolls occurs at a smaller value of Re_x and $Gr_{x'}$, which indicates the flow becomes more susceptible to the vortex instability with increasing wall to free stream temperature difference. The present observation for the effect of the wall to free stream temperature difference is similar to that of the natural convection case in Chapter 4.

The effect of the free stream velocity was also studied and the photographs are shown in Fig. 5.9 for U_∞=0.08, 0.1, 0.17 and 0.3 m/s with ΔT fixed within the range 28.6 - 29.6°K. The free stream velocity does not seem to affect the average wavelength significantly up to U_∞=0.17 m/s. For U_∞=0.3 m/s, the average wavelength of the vortex rolls is clearly observed to be decreased. However, one must also consider the increasing side wall effects with increasing free stream velocity. Ideally, a horizontal Blasius flow is not confined in the spanwise direction and the vortex instability must be studied in the pertinent flow condition. Therefore, the above result for the effect of the free stream velocity must be interpreted with the consideration of the specific geometry of the present wind tunnel.

On the other hand, the effect of increasing free stream velocity on the instability characteristics is clear. The onset of vortex rolls occurs at a larger value of Re_x and Gr_x, indicating that the flow becomes less susceptible to the vortex instability with increasing free stream velicity. This is in contrast to the study of wall to free stream temperature effects.

5.3.3 Instability Results

The experimental instability data for the case of $x_o=0$ cm are presented in Fig. 5.10. It has been found by Wu and Cheng [1] that the vortex instability results in a horizontal Blasius flow can be correlated by the following correlation equation:

$$Gr_{x'} = C\ Re_x^{1.5} \qquad (5.1)$$

As shown in Fig. 5.10, the correlation seems satisfactory for the present instability results. The data can be bounded by

$$Gr_{x'}/Re_x^{1.5} = 90 < C < 230 \qquad (5.2)$$

and the correlation results are shown as dotted lines. Shown together are the analytical results by Takimoto et al. [4] and the numerical results obtained by Moutsoglou, Chen and Cheng [5].

Nearly two to three orders of magnitude discrepancy between the theory and the experiment can be observed. It is noted that a similar discrepancy was also observed for the case of natural convection flow on inclined surfaces in Chapter 5. Such result is again attributed to the fact that the linear stability theory is based on infinitesimal disturbances which need a further amplification process in order to be detected experimentally.

The effect of an unheated length on the instability characteristics was the primary concern for the present vortex instability study. Measurements for the onset of the vortex instability were also made for two different unheated lengths, i.e. x_o=33.5 and 60.5 cm. The free stream velocity and the wall to free stream temperature ranged within 0.01 ~ 0.72 m/s and 6.9 - 33.6°K, respectively.

In general, the flow was observed to be more affected by the side walls with the presence of an unheated length and the determination of the vortex instability was consequently subject to a larger human error. As a result, the instability data showed a large scattering for the case of x_o=33.5 and 60.5 cm. For this reason, only the data obtained for occasional vortices (representing the lower bound of instability data) were plotted for both cases and compared with the case of x_o=0 cm in Fig. 5.11.

It is clearly seen that increasing unheated length results in a lower value of Gr_x, at a given free stream Reynolds number Re_x. This means the flow becomes more susceptible to the vortex instability with increasing unheated length. Although the data tend to scatter at low values of Re_x, the correlation equation [5.1] seems to be still applicable as indicated by the agreement between the slopes of the solid curves representing the lower bound of the instability data for each case.

5.4 Concluding Remarks

The problem of the vortex instability in a horizontal Blasius flow heated from below was approached by a flow visualization study.

Flow visualization experiments were carried out in a suction low speed wind tunnel to provide photographs showing the onset and subsequent growth of the longitudinal vortex rolls. The photographs of overall side and top views and the cross-sectional views of developing longitudinal vortex rolls were obtained for three different unheated lengths: x_o=0, 33.5 and 60.5 cm. For the case of x_o=0 cm, the effects of the wall to free stream temperature difference and the free stream velocity on the developing secondary flow patterns of longitudinal vortex rolls were investigated. It was found that the flow becomes more susceptible to the vortex instability with increasing wall to free stream temperature difference and an opposite trend was observed with increasing free stream velocity.

Experimental instability data were also obtained and compared with the published results. It was found that theory predicts two to three orders of magnitude lower values of critical Grashof number than the present experiment. The effect of an unheated length on the instability characteristic were also investigated for x_o=33.5 and 60.5 cm. The results showed that the flow becomes more susceptible to the vortex instability with increasing unheated length.

The present experimental study clearly reveals the complex secondary flow motion after the onset of the vortex instability in a horizontal Blasius flow heated from below. It is believed that the present photographs of longitudinal vortex rolls provide considerable physical insight into the vortex instability phenomenon in forced convection boundary layer flow.

5.5 References

1. Wu, R.S. and Cheng, K.C., "Thermal Instability of Blasius Flow along Horizontal Plates," Int. J. Heat Mass Transfer, Vol. 19, 1976, pp. 907 - 913.

2. Gilpin, R.R., Imura, H. and Cheng, K.C. "Experiments on the Onset of Longitudinal Vortices in Horizontal Blasius Flow Heated from Below," ASME Journal of Heat Transfer, Vol. 100, 1978, pp. 71 - 77.

3. Imura, H., Gilpin, R.R. and Cheng, K.C., "An Experimental Investigation of Heat Transfer and Buoyancy Induced Transition from Laminar Forced Convection to Turbulent Free Convection over a Horizontal Isothermally Heated Plate," ASME Journal of Heat Transfer, Vol. 100, 1978, pp. 429 - 434.

4. Takimoto, A., Hayashi, Y. and Matsuda, O., "Thermal Stability of Blasius Flow Over a Horizontal Flat Plate, "Heat Transfer-Japanese Research, Vol. 12, 1983, pp. 19 - 33.

5. Moutsoglou, A., Chen, T.S. and Cheng, K.C., "Vortex Instability of Mixed Convection Flow Over a Horizontal Flat Plate," ASME Journal of Heat Transfer, Vol. 103, 1981, pp. 257 - 261.

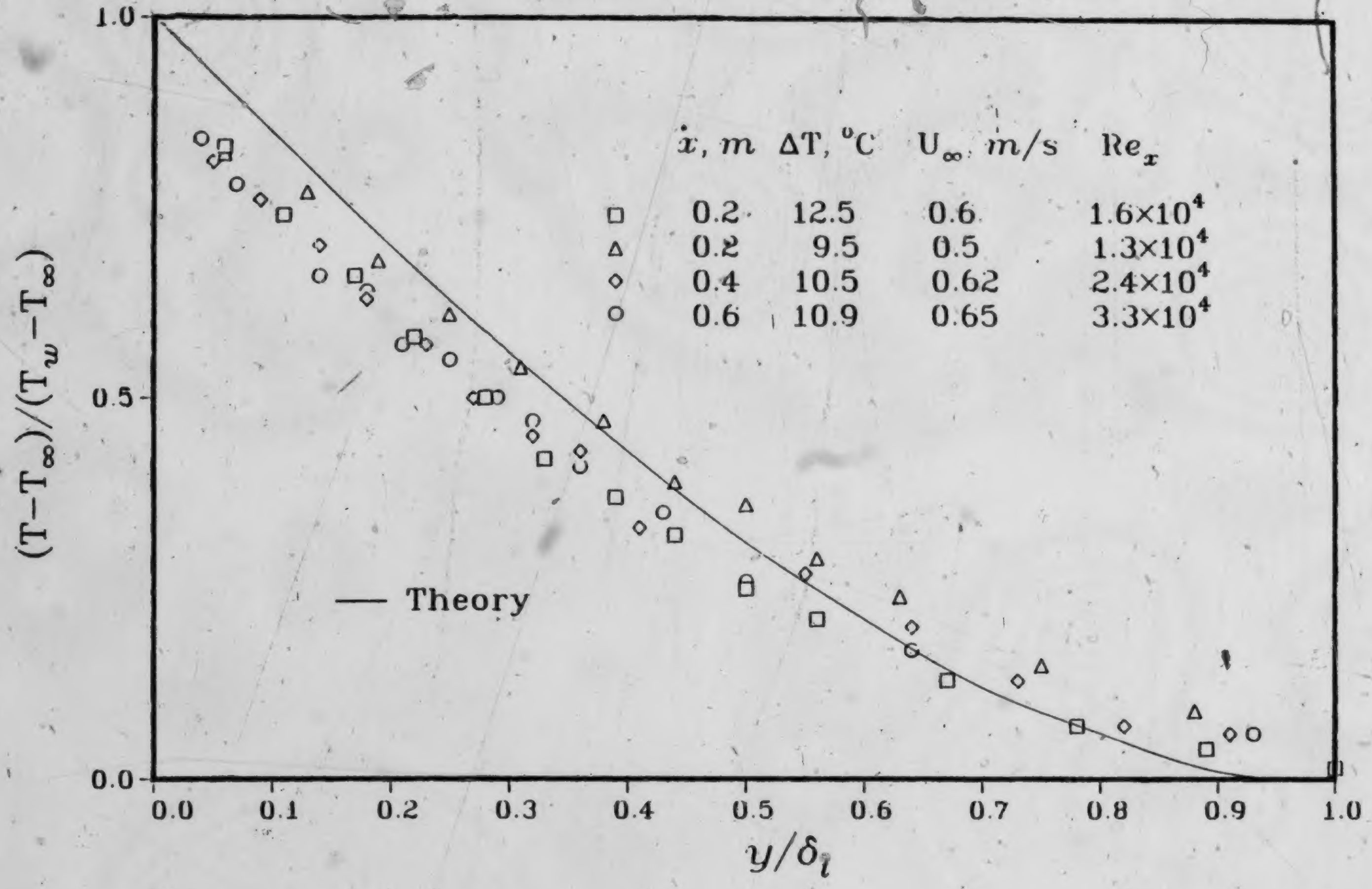

Fig. 5.1 Temperature Profiles for the Case of Stable Flow

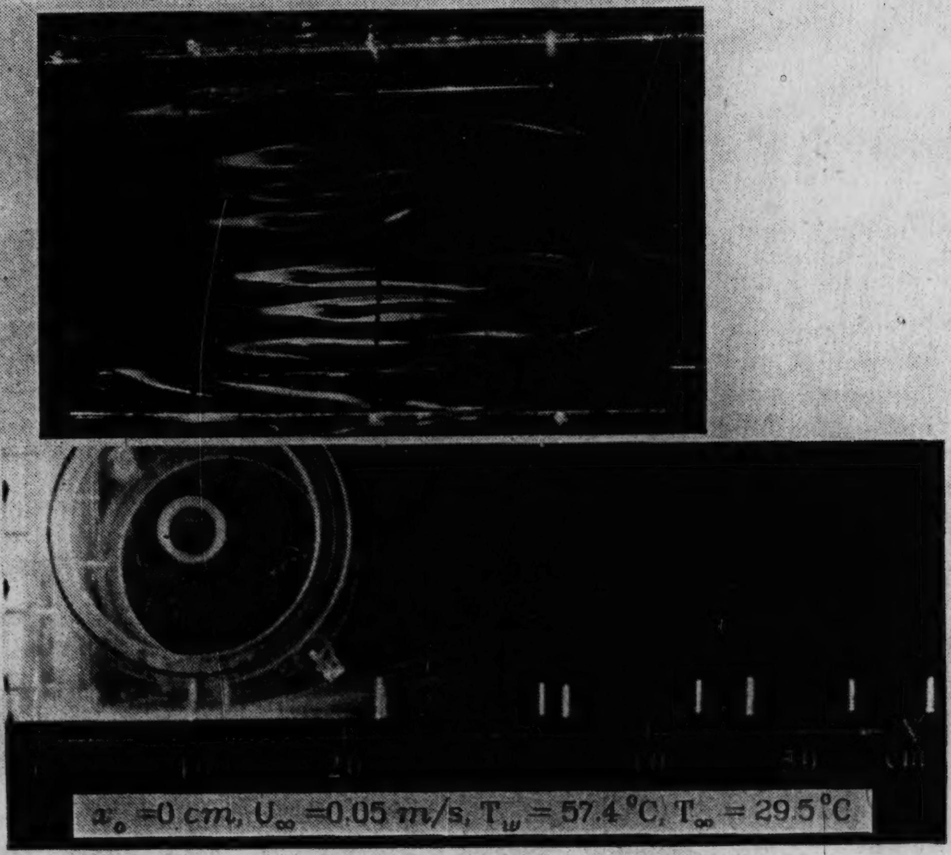
10
20
40
50
cm
x_o =0 cm, U∞ =0.05 m/s, T_w = 57.4°C, T∞ = 29.5°C

Fig. 5.2 Top and Side Views of Developing Longitudinal Vortices for x_o=0 cm, U_∞=0.05 m/s, T_W=57.4°C and T_∞=29.5°C

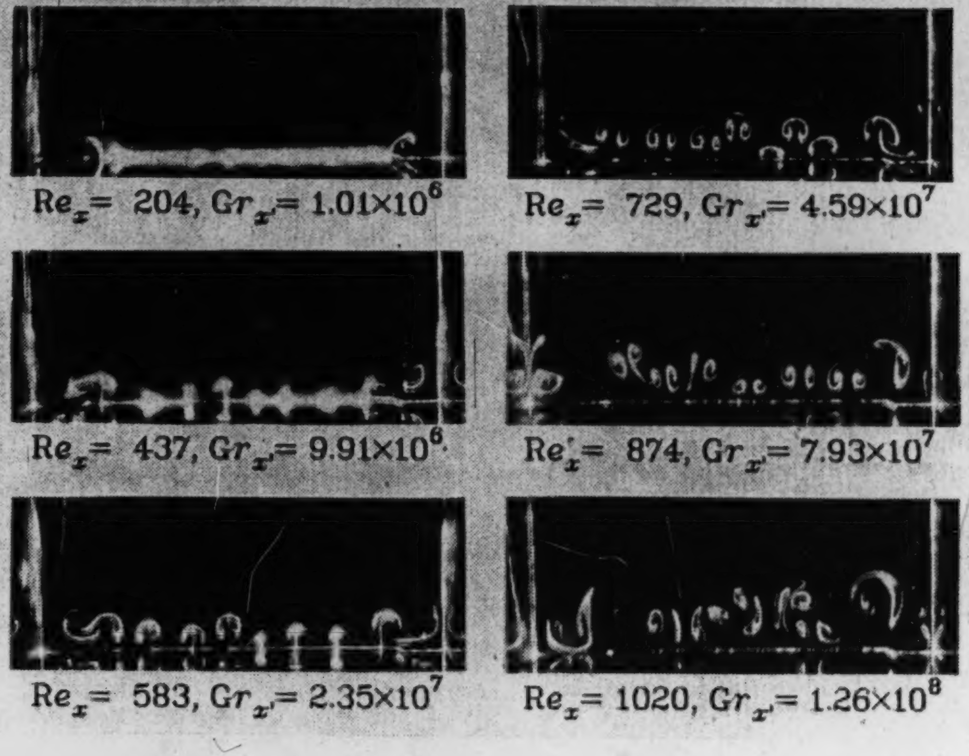

$Re_x = 204, Gr_{x'} = 1.01\times10^6$

$Re_x = 729, Gr_{x'} = 4.59\times10^7$

$Re_x = 437, Gr_{x'} = 9.91\times10^6$

$Re_x = 874, Gr_{x'} = 7.93\times10^7$

$Re_x = 583, Gr_{x'} = 2.35\times10^7$

$Re_x = 1020, Gr_{x'} = 1.26\times10^8$

Fig. 5.3 Cross-sectional Views of Secondary Flow Patterns for x_o=0 cm, U_∞=0.05 m/s and ΔT=27.9°K

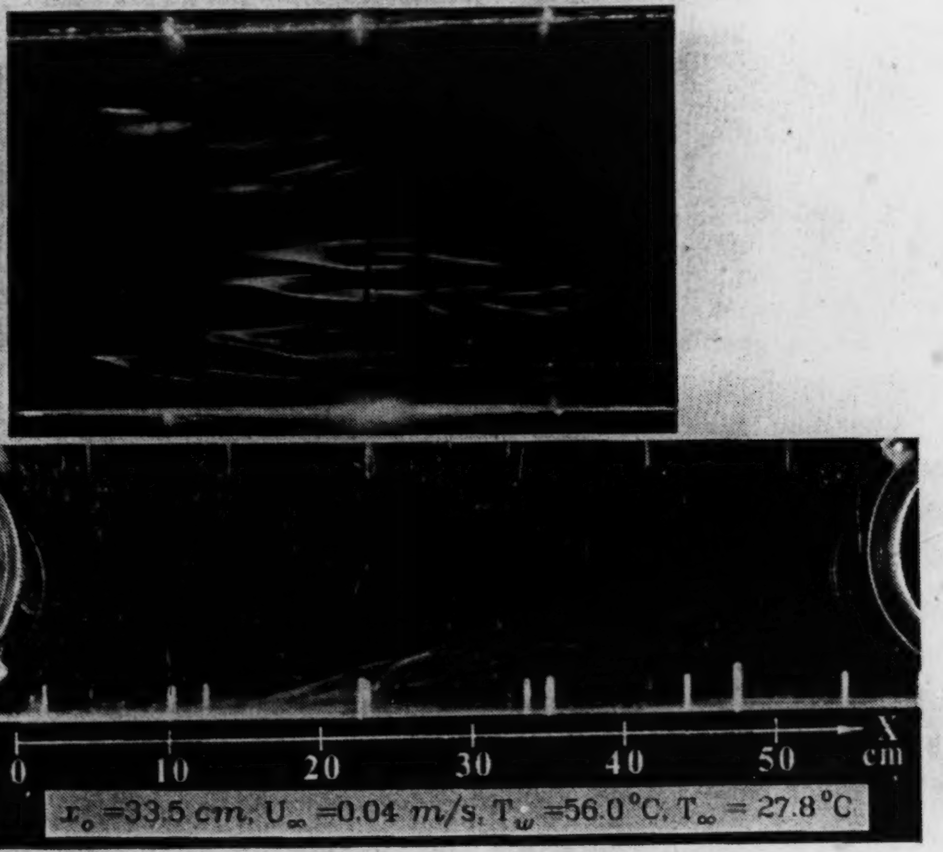
X
cm
0
10
20
30
40
50
x_o =33.5 cm, U_∞ =0.04 m/s, T_w =56.0 °C, T_∞ = 27.8 °C

Fig. 5.4 Top and Side Views of Developing Longitudinal Vortices for x_o=33.5 cm, U_∞=0.04 m/s, T_w=56.0°C and T_∞=27.8°C

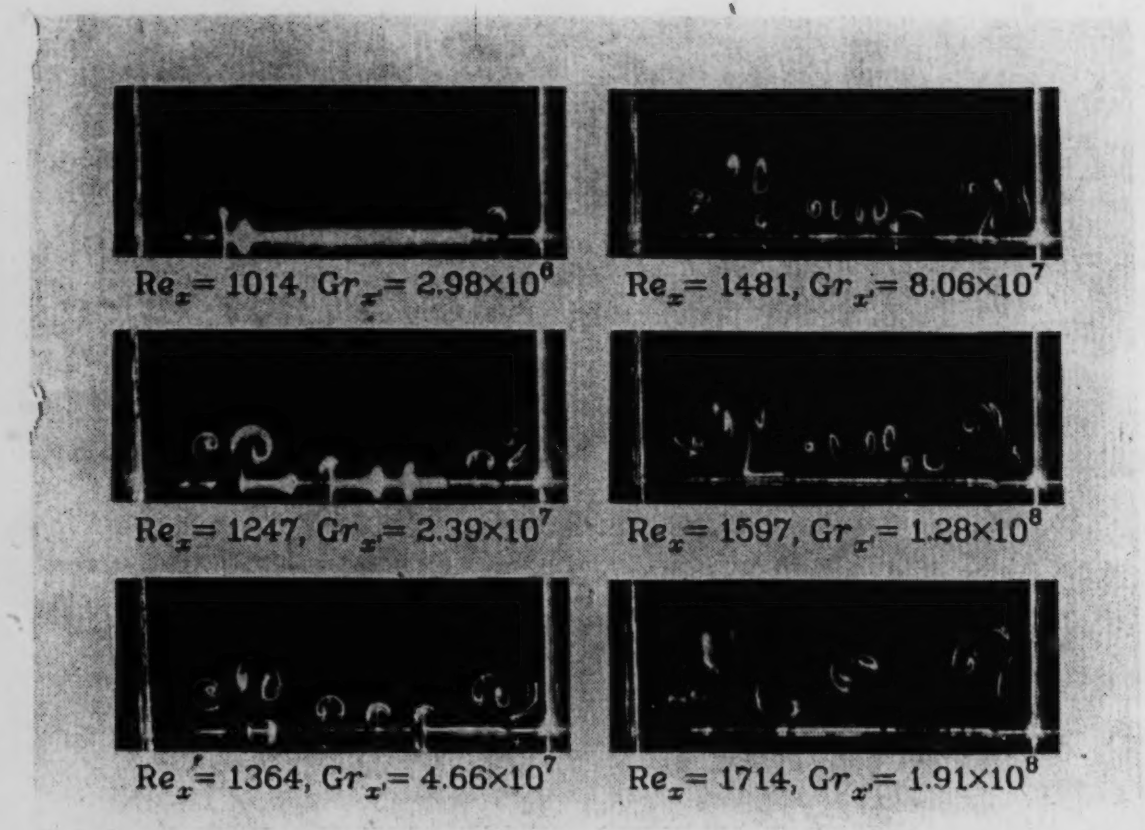

$Re_x = 1014$, $Gr_{x'} = 2.98\times10^6$

$Re_x = 1481$, $Gr_{x'} = 8.06\times10^7$

$Re_x = 1247$, $Gr_{x'} = 2.39\times10^7$

$Re_x = 1597$, $Gr_{x'} = 1.28\times10^8$

$Re_x = 1364$, $Gr_{x'} = 4.66\times10^7$

$Re_x = 1714$, $Gr_{x'} = 1.91\times10^8$

Fig. 5.5 Cross-sectional Views of Secondary Flow Patterns for x_o=33.5 cm, U_∞=0.04 m/s and ΔT=28.2°K

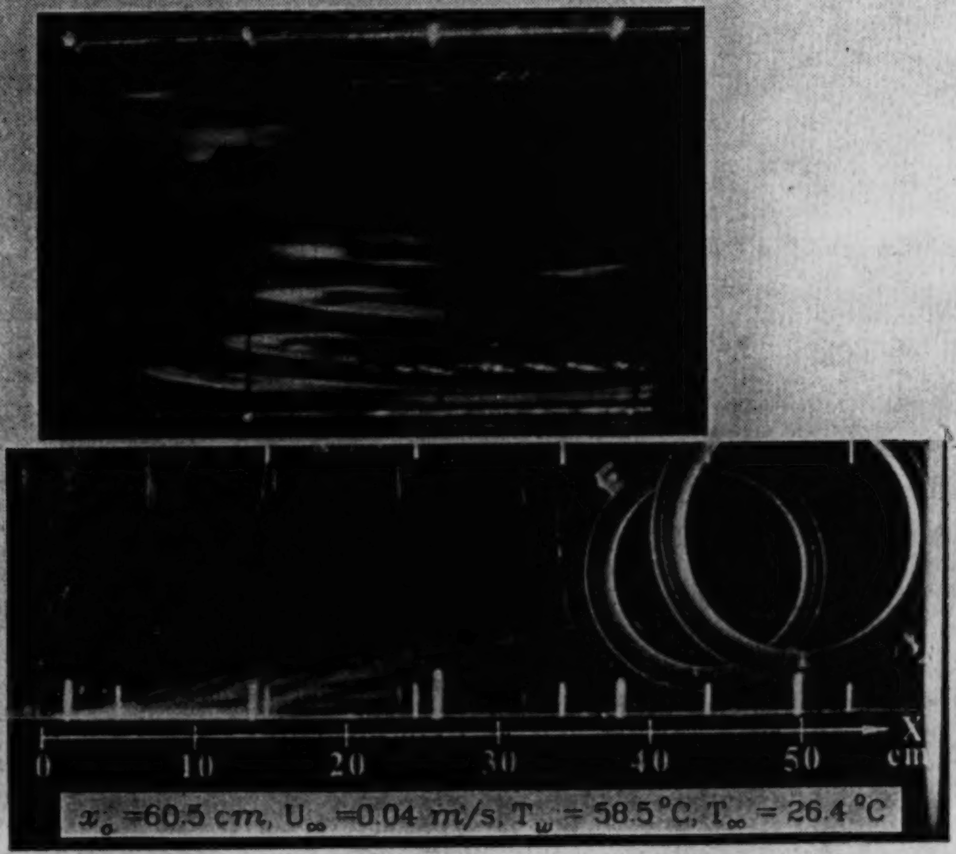
0
10
20
30
40
50
X
cm
x_o =60.5 cm, U_∞ =0.04 m/s, T_w = 58.5 °C, T_∞ = 26.4 °C

Fig. 5.6 Top and Side Views of Developing Longitudinal Vortices for x_o=60.5 cm, U_∞=0.04 m/s, T_W=58.5°C and T_∞=26.4°C

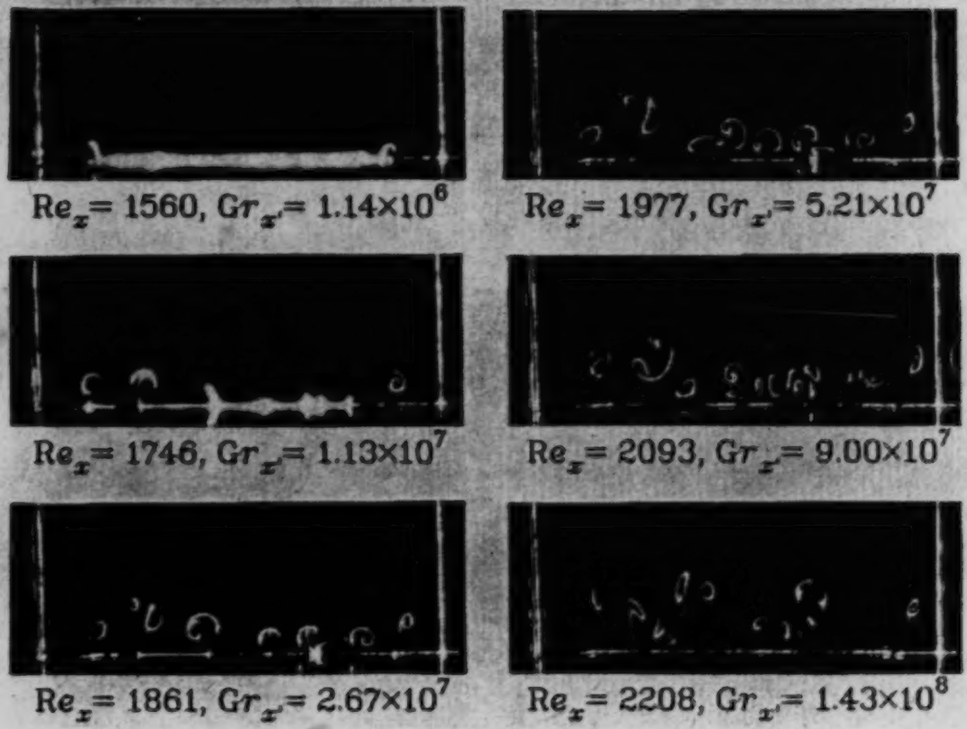

$Re_x = 1560$, $Gr_{x'} = 1.14\times10^6$

$Re_x = 1977$, $Gr_{x'} = 5.21\times10^7$

$Re_x = 1746$, $Gr_{x'} = 1.13\times10^7$

$Re_x = 2093$, $Gr_{x'} = 9.00\times10^7$

$Re_x = 1861$, $Gr_{x'} = 2.67\times10^7$

$Re_x = 2208$, $Gr_{x'} = 1.43\times10^8$

Fig. 5.7 Cross-sectional Views of Secondary Flow Patterns for x_o=60.5 cm, U_∞=0.04 m/s and ΔT=32.1°K

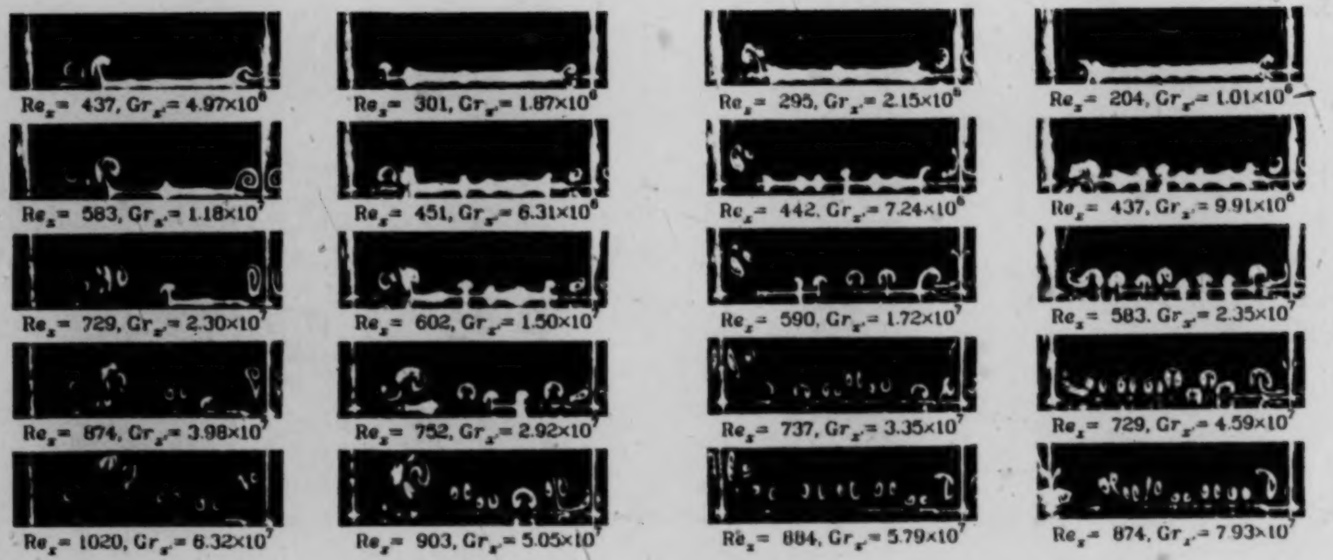
Re_x= 437, Gr_x= 4.97×10^6
Re_x= 583, Gr_x= 1.18×10^7
Re_x= 729, Gr_x= 2.30×10^7
Re_x= 874, Gr_x= 3.98×10^7
Re_x= 1020, Gr_x= 6.32×10^7
Re_x= 301, Gr_x= 1.87×10^6
Re_x= 451, Gr_x= 6.31×10^6
Re_x= 602, Gr_x= 1.50×10^7
Re_x= 752, Gr_x= 2.92×10^7
Re_x= 903, Gr_x= 5.05×10^7
Re_x= 295, Gr_x= 2.15×10^6
Re_x= 442, Gr_x= 7.24×10^6
Re_x= 590, Gr_x= 1.72×10^7
Re_x= 737, Gr_x= 3.35×10^7
Re_x= 884, Gr_x= 5.79×10^7
Re_x= 204, Gr_x= 1.01×10^6
Re_x= 437, Gr_x= 9.91×10^6
Re_x= 583, Gr_x= 2.35×10^7
Re_x= 729, Gr_x= 4.59×10^7
Re_x= 874, Gr_x= 7.93×10^7

(*a*) U_∞ =0.05 *m*/s, ΔT= 13.6 °K (*b*) U_∞ =0.05 *m*/s, ΔT= 16.3 °K (*c*) U_∞ =0.05 *m*/s, ΔT= 19.7 °K (*d*) U_∞ =0.05 *m*/s, ΔT= 27.9 °K

Fig. 5.8 Effect of ΔT on Developing Secondary Flow Patterns of Vortices for x_o=0 cm

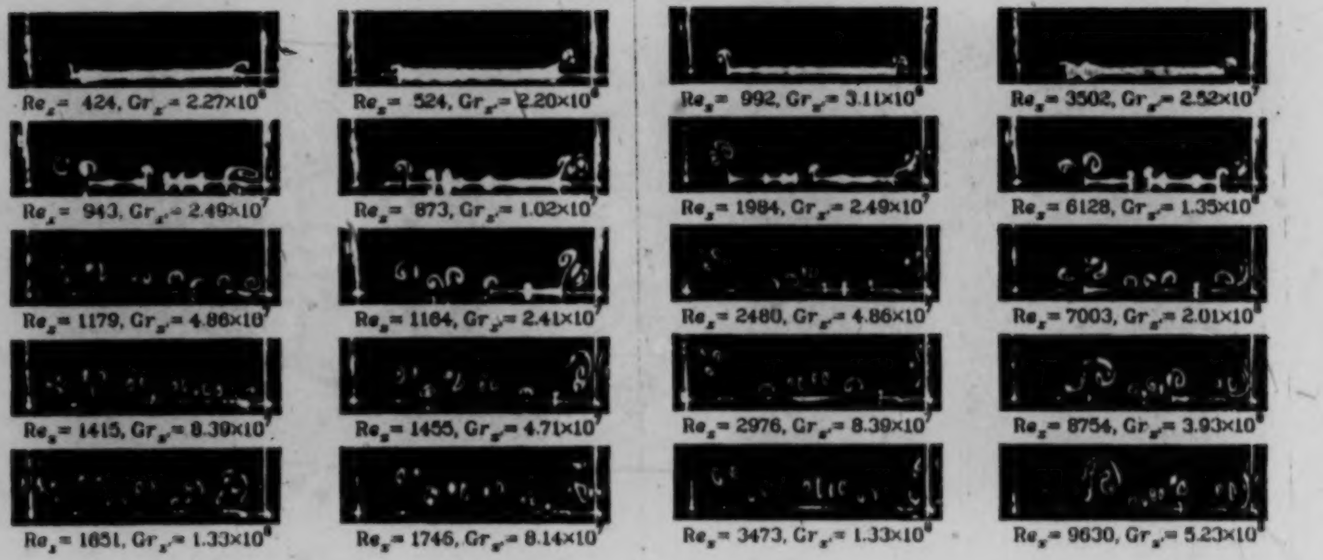
$Re_x = 424$, $Gr_x = 2.27\times10^6$
$Re_x = 943$, $Gr_x = 2.49\times10^7$
$Re_x = 1179$, $Gr_x = 4.86\times10^7$
$Re_x = 1415$, $Gr_x = 8.39\times10^7$
$Re_x = 1651$, $Gr_x = 1.33\times10^8$
$Re_x = 524$, $Gr_x = 2.20\times10^6$
$Re_x = 873$, $Gr_x = 1.02\times10^7$
$Re_x = 1164$, $Gr_x = 2.41\times10^7$
$Re_x = 1455$, $Gr_x = 4.71\times10^7$
$Re_x = 1746$, $Gr_x = 8.14\times10^7$
$Re_x = 992$, $Gr_x = 3.11\times10^6$
$Re_x = 1984$, $Gr_x = 2.49\times10^7$
$Re_x = 2480$, $Gr_x = 4.86\times10^7$
$Re_x = 2976$, $Gr_x = 8.39\times10^7$
$Re_x = 3473$, $Gr_x = 1.33\times10^8$
$Re_x = 3502$, $Gr_x = 2.52\times10^7$
$Re_x = 6128$, $Gr_x = 1.35\times10^8$
$Re_x = 7003$, $Gr_x = 2.01\times10^8$
$Re_x = 8754$, $Gr_x = 3.93\times10^8$
$Re_x = 9630$, $Gr_x = 5.23\times10^8$

(*a*) $U_\infty = 0.08$ *m/s*, $\Delta T = 28.8$ °K (*b*) $U_\infty = 0.1$ *m/s*, $\Delta T = 28.6$ °K (*c*) $U_\infty = 0.17$ *m/s*, $\Delta T = 29.3$ °K (*d*) $U_\infty = 0.3$ *m/s*, $\Delta T = 29.6$ °K

Fig. 5.9 Effect of U_∞ on Developing Secondary Flow Patterns of Vortices for $x_o = 0$ cm

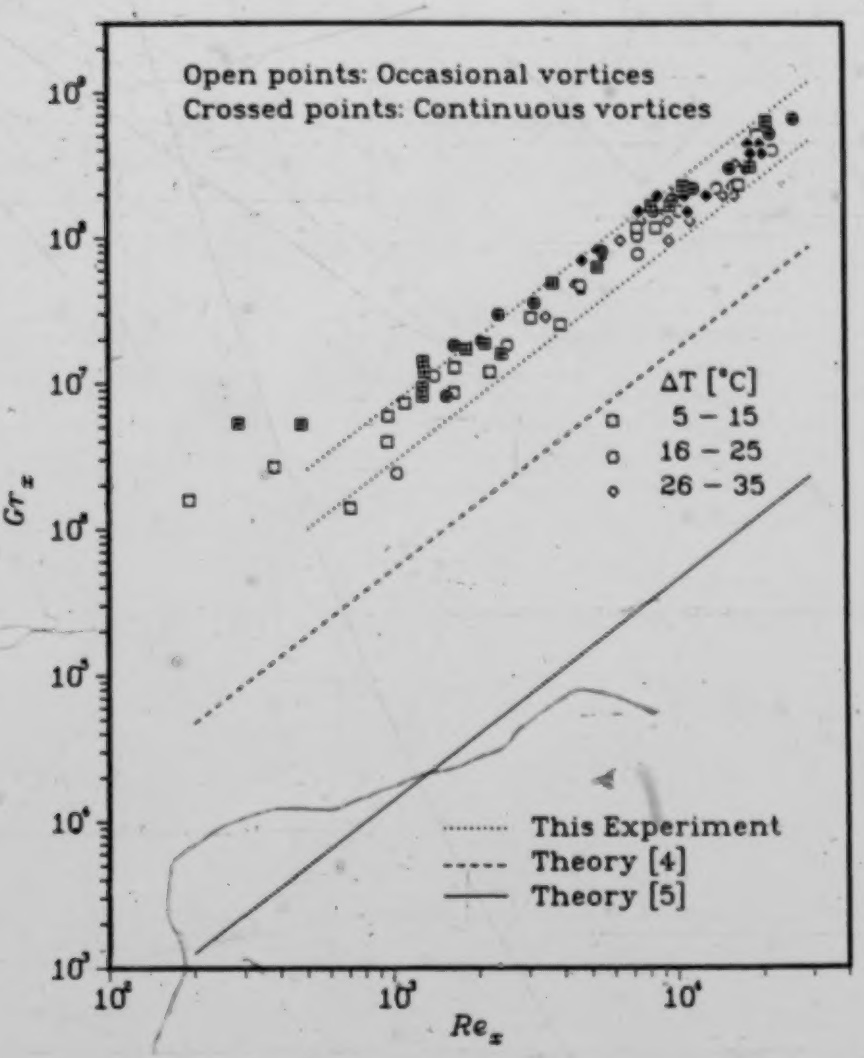

Fig. 5.10 Experimental Instability Results for $x_0=0$ cm

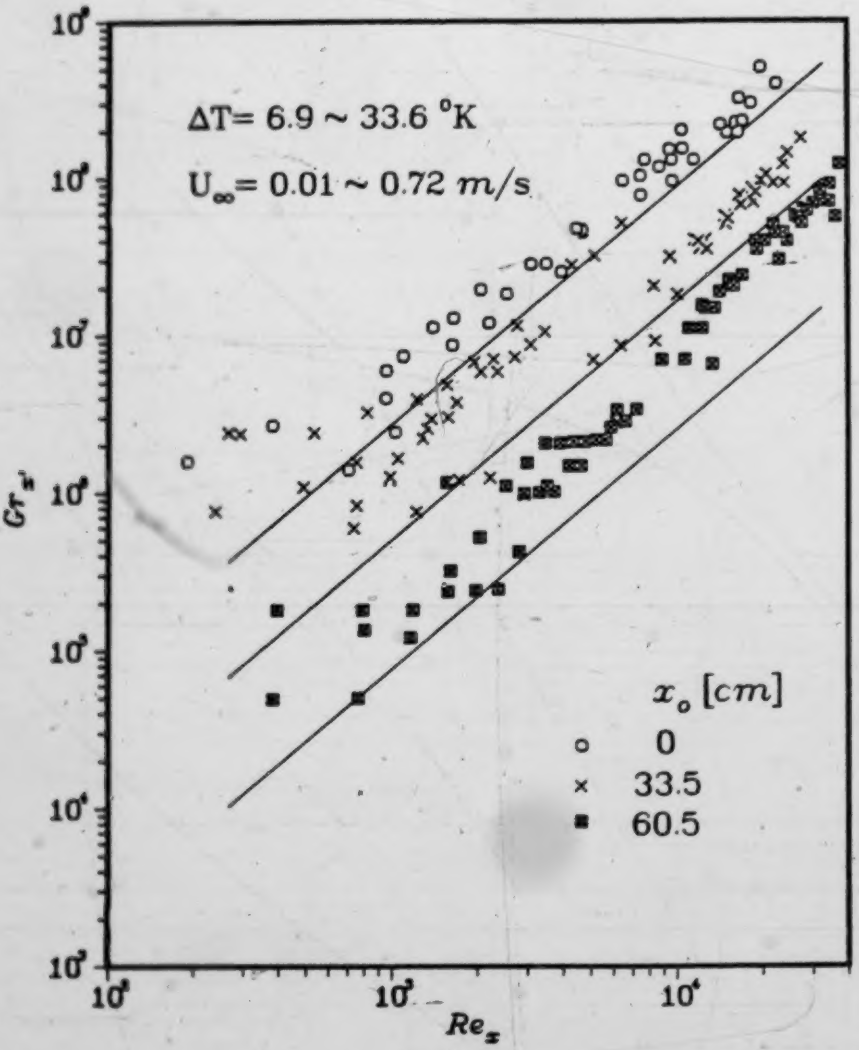

Fig. 5.11 Effect of x_o on Vortex Instability

6. Conclusions

6.1 Buoyancy force effects on Laminar Forced Convection Flow in Curved Pipes

Experiments were conducted to study the buoyancy force effects on laminar forced convection air flow in a 200° pipe bend under the uniform wall heat flux boundary condition with parabolic entrance velocity profile.

Measurements for the wall temperature distributions and Nusselt numbers were made at De=150, 200, 300, 430, 600 and 800 for three different inclination angles of the curvature plane of the pipe bend: upward vertical, horizontal and downward vertical cases. The present results for the buoyancy force effects on heat transfer characteristics for the horizontal flow case turned out to be in direct contradiction to the existing theoretical results for fully developed flow. It is felt that further work should be conducted to check the accuracy of measurements for volume flow rate and bulk temperature particularly for low Dean number regime.

The buoyancy force effects arising from varying the inclination angle of the curvature plane do not appear to be extensively studied in the literature regardless of the practical importance of the problem. The present results for the effect of inclination angle clearly revealed the significance of the interaction between the buoyancy force and the centrifugal force in the entrance region. This point also suggests the need for further experimental and theoretical studies.

6.2 Flow Visualization Studies on Laminar Forced Convection Flow in Curved pipes

The present flow visualization study is basically an extension of the preceding heat transfer experiments reported in Chapter 2. Emphasis was given to the physical understanding of the buoyancy force effects reflected in the observed secondary flow patterns.

A series of flow visualization studies were carried out at the exit of 200° pipe bend for three different inclination angles of the curvature plane. The wall boundary condition and the entry flow condition are identical to those of the preceding heat transfer experiments.

For the case of horizontal flow, the interaction between the buoyancy force and the centrifugal force is clearly revealed. The skewed pair of vortices at low Reynolds numbers shown by the present flow visualization study are in general good agreement with the streamline patterns obtained by recent numerical solutions. The flow visualization photographs for the upward flow and the downward flow case also provide considerable physical insight into the flow phenomena resulting from a complex interaction between the buoyancy force and the centrifugal force in the simultaneous hydrodynamic and thermal entrance region.

It is believed that the present flow visualization results will be valuable to the future investigations in the related field.

6.3 Flow Visualization Studies on Vortex Instability of Natural Convection Flow over Horizontal and Slightly Inclined Constant Temperature Plates

Flow visualization experiments were conducted to study the problem of the vortex instability in a natural convection flow over horizontal or slightly inclined isothermally heated flat plate employing a smoke injection technique.

Photographs of the side and top views and the cross-section views of the longitudinal vortex rolls were presented. The effects of the wall to ambient temperature difference and the inclination angle on the developing secondary flow patterns of vortex rolls were also illustrated by flow visualization photographs. Of special interest was the effect of the two parameters on the average wavelength of the vortex rolls. The average wavelength of the vortex rolls was found to be more sensitive to changes in the wall to ambient temperature difference.

Experimental instability data were also obtained for five different inclination angles: θ=0, 5, 10, 15 and 20°. The present instability data fill in some existing gaps in the experimental instability results at small inclination angles from the horizontal direction. The data seemed to show a similar trend to the known experimental and theoretical results. However, over three orders of magnitude difference between the experimental and theoretical instability results was observed. Such discrepancy apparently demands further investigations.

A correlation for the average wavelength was also made. The results showed that the data can be well correlated using the parameter suggested by theory.

Future investigations may include a correlation for the critical Grashof number as a function of the inclination angle. The study on the transition to fully turbulent regime will also be of practical interest.

6.4 Flow Visualization Studies on Vortex Instability in Horizontal Blasius Flow

The problem of the vortex instability in a horizontal Blasius flow heated from below was investigated by a flow visualization technique.

Flow visualization experiments employing a smoke injection method were conducted in a suction low speed wind tunnel to show the onset and subsequent development of the longitudinal vortex rolls over an isothermally heated horizontal plate. Of particular interest was the effect of an unheated length on the formation of the vortex rolls and on the instability characteristics.

Photographs of the side and the top views and the cross-sectional views of developing secondary flow patterns of the longitudinal vortex rolls were presented for three cases of different unheated lengths: x_o=0, 33.5 and 60.5 cm. The effects of the wall to free stream temperature difference and the free stream velocity on the developing vortex rolls were also investigated for the case of x_o=0 cm. It was found that the average wavelength of the vortex rolls strongly depends on the wall to free stream temperature difference. No distinct correlation between the average wavelengh and the free stream velocity was found.

Instability data for the critical Grashof number were also obtained for different unheated lengths. The results showed the flow becomes more susceptible to the onset of vortex instability with increasing unheated length.

The effect of an unheated length on the vortex instability has practical importance in many applications. Neverthless, no theoretical or experimental works are yet available in the literature. The present result can be considered as a preliminary step to the problem. Future studies may include the effect of free stream turbulence. Correlation for the average wavelength of the vortex rolls is also worth an exploration.

Appendix I

Uncertainty Analysis for Chapter 2

i) Error in Heat Transfer Coefficient

The heat transfer coefficient is defined as

$$h = q_w/(T_w-T_b) = f(q_w, T_w, T_b) \qquad \text{(A-1)}$$

Taking derivatives

$$dh = (\partial f/\partial q_w)dq_w + (\partial f/\partial T_w)dT_w + (\partial f/\partial T_b)dT_b \qquad \text{(A-2)}$$

where $\partial f/\partial q_w = 1/(T_w-T_b)$

$\partial f/\partial T_w = -q_w/(T_w-T_b)^2$

$\partial f/\partial T_b = q_w/(T_w-T_b)^2$

Dividing both sides of Eq.(A-2) by Eq.(A-1) yields

$$dh/h = dq_w/q_w-(dT_w/T_w)/(1-T_b/T_w)+(dT_b/T_b)/(T_w/T_b-1) \qquad \text{(A-3)}$$

where the terms dh/h, dq_w/q_w, dT_w/T_w and dT_b/T_b are the fractional errors denoted by ϵ_h, ϵ_{qw}, ϵ_{Tw} and ϵ_{Tb}, respectively.

Then, the mean square error for h can be written as

$$\epsilon_h = [\epsilon_{qw}^2 + \epsilon_{Tw}^2/(1-T_b/T_w)^2 + \epsilon_{Tb}^2/(T_w/T_b-1)^2]^{1/2} \qquad \text{(A-4)}$$

ii) Error in Wall Heat Flux

From the energy balance

$$q_w = m\ C_p\ (T_{be} - T_{bi})/(2\pi aL) \qquad \text{(A-5)}$$

Assuming C_p is constant

$$q_w = \text{Const. } m\ (T_{be}-T_{bi})/(aL) = f(m,\ T_{be},\ T_{bi},\ a,\ L) \qquad \text{(A-6)}$$

Then, it can be shown that

$$\epsilon_{qw} = \epsilon_m + \epsilon_{Tbe}/(1-T_{bi}/T_{be}) - \epsilon_{Tbi}/(T_{be}/T_{bi}-1) - \epsilon_a - \epsilon_L \qquad \text{(A-7)}$$

The mean square error for q_w is then

$$\epsilon_{qw} = [\epsilon_m^2 + \epsilon_{Tbe}^2/(1-T_{bi}/T_{be})^2 + \epsilon_{Tbi}^2/(T_{be}/T_{bi}-1)^2 + \epsilon_a^2 + \epsilon_b^2]^{1/2} \qquad \text{(A-8)}$$

iii) Error in the Inlet and Exit Bulk Temperature

The fractional error for inlet bulk temperature is estimated from the measurements for one-dimensional temperature profiles at the bend inlet.

By curve-fitting the data for temperature profile and assuming a parabolic velocity profile at the bend inlet, a crude approximation for the inlet bulk temperature can be made using the following equation, i.e.

$$T_b = \frac{\int_0^a u\, T_{air}\, dr}{\int_0^a u\, dr} \qquad \text{(A-9)}$$

where r is the coordinate in the radial direction.

Since the center air temperature was used as the inlet bulk temperature for the present experiments, ϵ_{Tbi} is obtained by

$$\epsilon_{Tbi} = (T_b - T_{center})/T_{center} \qquad \text{(A-10)}$$

The fractional error for the exit bulk temperature measurements ϵ_{Tbe} is estimated based on the temperature variation observed while traversing the thermocouple probe across the center hole in the fourth partition of the mixing box (see Fig. 2.4 in Chapter 2).

iv) Error in Mass Flow Rate

ϵ_m is based on the read-off error of the calibration curve.

For typical cases the following estimates were made:

ϵ_{Tbi} = 3.2 %
ϵ_{Tbe} = 3.0 %
ϵ_m = 2.8 %
ϵ_a = 0.75 %
ϵ_L = 0.13 %
T_{bi}/T_{be} = 0.37, based on average T_{bi} and T_{be}.